Miniature Mobile Systems for Inspection of Ferromagnetic Structures

THÈSE N^{O} 5293 (2012)

PRÉSENTÉE LE 28 MARS 2012

À LA FACULTÉ DES SCIENCES ET TECHNIQUES DE L'INGÉNIEUR
LABORATOIRE DE SYSTÈMES ROBOTIQUES 1
PROGRAMME DOCTORAL EN SYSTÈMES DE PRODUCTION ET ROBOTIQUE

ÉCOLE POLYTECHNIQUE FÉDÉRALE DE LAUSANNE

POUR L'OBTENTION DU GRADE DE DOCTEUR ÈS SCIENCES

PAR

Patrick SCHOENEICH

acceptée sur proposition du jury:

Dr A. Karimi, président du jury
Dr F. Mondada, directeur de thèse
Dr G. Caprari, rapporteur
Dr R. Moser, rapporteur
Dr J.-C. Zufferey, rapporteur

ÉCOLE POLYTECHNIQUE
FÉDÉRALE DE LAUSANNE
Suisse
2012

Abstract

Power plants require periodical inspections to control their state. To ensure a safe operation, parts that could fail before the next inspection are repaired or replaced, since a forced outage due to a failure can cost up to millions of dollars per day. Non-Destructive Testing (NDT) methods are used to detect different defects that could occur, such as cracks, thinning, corrosion or pitting. Some parts are inspected directly in situ, but may be difficult to access; these can require opening access holes or building scaffoldings. Other parts are disassembled and inspected in workshops, when the required inspection tools cannot be moved.

In this thesis, we developed innovative miniature mobile systems able to move within these small and complex installations and inspect them. Bringing sensors to difficult-to-access places using climbing robots can reduce the inspection time and costs, because some dismantling or scaffolding can be eliminated. New miniature sensors can help to inspect complex parts without disassembling them, and reduce the inspection costs, as well.

To perform such inspections, miniature mobile systems require a high mobility and keen sensing capabilities. The following approach was used to develop these systems. First, different innovative climbing robots are developed. They use magnetic adhesion, as most structures are made of ferromagnetic steel. Then, vision is embedded in some of the robots. Performing visual inspections becomes thus possible, as well as controlling the robots remotely, without viewing them. Finally, non-visual NDT sensors are developed and embedded in some of the robots, allowing them to detect defects that simple vision cannot detect. Achieving the miniaturization of the developed systems requires strong system integration during these three steps. A set of examples for the different steps has been designed, implemented and tested to illustrate this approach.

The Tripillars robots, for instance, use caterpillars, and are able to climb on surfaces of any inclination and to pass inner angles. The Cy-mag^{3Ds} robots use an innovative magnetic wheel concept, and are able to climb on surfaces of any inclination and to pass inner angles, outer angles and surface flips. The Tubulos robots move in tubes of 25 mm diameter at any inclination. All robots embed the required electronics, actuators, sensors and energy to be controlled remotely by the user. Wireless transmission of the commands signals allows the systems to maintain their full mobility without disturbing cables. Integrating Hall sensors near the magnetic systems allows them to measure the adhesion force. This information improves the security of the robots, since when the adhesion force becomes low, the robots can be stopped before they fall. The Tubulo II uses Magnetic Switchable Devices (MSDs) for adhesion. An MSD is composed of a ferromagnetic stator and one or more moving magnets; it has the advantage of requiring only a low force to switch on or off a high adhesion force. MSDs have the advantage of being easy to clean of the magnetic dust that is present in most real environments and that sticks strongly to magnetic systems.

As an additional step toward inspection, a camera is embedded on the Cy-mag^{3D} II and the Tubulos. It allows these robots to inspect visually the structures the robots move in, and to control them remotely. The perspective of a climbing robot in an unknown environment is often not enough to give the user a sense of its scale, and to move efficiently in it. A distance sensor is designed and embedded on the Cy-mag^{3D} II, which increases the user's perception of the environment substantially;

Finally, an innovative miniature Magnetic Particle Inspection (MPI) system was developed to inspect turbine blades without disassembling them. An MSD is used to perform the required magnetization. The system can automatically inspect a flat surface, performing all the required steps of MPI: magnetize, spray magnetic particles, record images under UV light and demagnetize. Thanks to the strong integration and miniaturization, the system can potentially inspect complex parts such as steam turbines.

Keywords: Inspection robot, Climbing robot, Mobile robot, Magnetic adhesion, Vision, Non-Destructive Testing, Integration.

Résumé

Des inspections périodiques des centrales électriques sont nécessaires pour contrôler leur état. Les pièces qui pourraient casser avant la prochaine inspection sont réparées ou changées pour assurer un fonctionnement sûr de la centrale. En effet, un arrêt forcé peut coûter jusqu'à plusieurs millions de dollars par jours. Des méthodes de Contrôle Non Destructif (CND) sont utilisées pour détecter les différents défauts qui peuvent se produire, comme des fissures, amincissements ou corrosions. Certaines pièces sont inspectées directement in situ, mais peuvent être difficiles d'accès et nécessiter la création de trou d'accès ou la construction d'échafaudages. D'autres pièces sont désassemblées et inspectées dans des ateliers quand les outils nécessaires à l'inspection ne peuvent pas être déplacés.

Dans cette thèse, nous avons développé des systèmes mobiles miniatures innovants pouvant bouger dans ces espaces petits et complexes et les inspecter. Le temps d'inspection et les coûts peuvent être réduits en amenant des capteurs à l'aide de robots grimpants dans les endroits difficiles d'accès, car des démontages ou échafaudages peuvent être épargnés. Des nouveaux capteurs miniatures permettent d'inspecter des pièces complexes sans démontage, ce qui réduit également les coûts.

Les systèmes mobiles miniatures permettant d'effectuer de telles inspections ont besoin d'une grande mobilité et d'une grande perception. L'approche suivante a été suivie pour développer ces systèmes. Premièrement, plusieurs robots grimpants innovants sont développés. Ils utilisent une adhésion magnétique car la plupart des structures sont en acier ferromagnétique. Ensuite, un système de vision est embarqué sur certain des robots. Cela rend possible l'inspection visuelle ainsi que le contrôle à distance des robots. Finalement, des capteurs CND non visuels sont développés et embarqués sur certain des robots. Ils permettent de détecter des défauts que la simple vision ne peut pas détecter. Durant ces trois étapes, une intégration importante est nécessaire pour arriver à miniaturiser les systèmes. Plusieurs exemples ont été développés, implémentés et testés pour illustrer cette approche pour les différentes étapes.

Par exemple, les robots Tripillars utilisent des chenilles et sont capables de grimper sur des surfaces de n'importe quelle inclinaison et de passer des angles intérieurs. Les robots Cy-mag^{3Ds} utilisent un nouveau concept de roues magnétiques, et sont capables de grimper sur des surfaces de n'importe quelle inclinaison, de passer des angles intérieurs et des angles extérieurs. Les robots Tubulos se déplacent dans des tubes de 25 mm de diamètre de n'importe quelle inclinaison. Tous les robots embarquent l'électronique, les actionneurs, les capteurs et l'énergie nécessaire pour être contrôlés à distance par un utilisateur. La transmission sans fil des commandes permet de conserver la mobilité complète des robots sans câbles gênants. L'intégration de capteurs Hall proche des systèmes magnétiques permet de mesurer la force d'adhésion. Cette information augmente la sécurité des robots, puisqu'on peut les arrêter et les empêcher de tomber lorsque la force d'adhésion devient

trop basse. Le Tubulo II utilise des Systèmes Magnétiques à Commutation (SMC) pour l'adhésion. Un SMC est composé d'un stator ferromagnétique et d'un ou plusieurs aimants qui peuvent bouger, et a l'avantage de générer une grande force d'adhésion qui peut être enclenchée et déclenchée avec une faible force. Les SMCs ont l'avantage d'être faciles à nettoyer de la poussière magnétique présente dans la plupart des environnements réels, qui adhère fortement aux systèmes magnétiques standards.

L'étape suivante vers l'inspection est de rajouter une caméra et un système de transmission d'images au Cy-mag^{3D} II et aux Tubulos. Cela permet d'inspecter visuellement les structures dans lesquelles le robot se déplace, ainsi que de les contrôler à distance. Un capteur de distance est développé et rajouté sur le Cy-mag^{3D} II. Il permet d'augmenter la perception de l'environnement de l'utilisateur, et permet un contrôle plus efficace du robot. En effet, il est difficile d'avoir un sens précis de l'échelle des structures inconnues dans lesquelles le robot se déplace avec comme seule information l'image de la caméra.

Finalement, un système miniature d'inspection par magnétoscopie est développé pour inspecter des pales de turbines sans les démonter. Un SMC est utilisé pour effectuer la magnétisation nécessaire. Le système peut inspecter automatiquement une surface plane, en effectuant toutes les étapes nécessaires à la magnétoscopie : magnétisation, dispersion de particules magnétiques, enregistrement d'images sous lumière UV et démagnétisation. Grâce à l'intégration et la miniaturisation importante, le système peut potentiellement inspecter des pièces complexes telles que des turbines.

Mots clés : Robot d'inspection, Robot grimpant, Adhésion magnétique, Vision, Intégration, Contrôle Non Destructif.

Acknowledgments

First, I would like to thank my supervisor Francesco Mondada for giving me the opportunity to work in his group. His enthusiasm, knowledge and the positive atmosphere he created in the Mobots group encouraged me a lot during the 4 years of my thesis.

I would like to express my gratitude to the thesis committee members, Dr. Gilles Caprari, Dr. Roland Moser, Dr. Jean-Christophe Zufferey and Dr. Alireza Karimi for their careful reading of my work and their constructive suggestions.

I would like to thank my colleagues at the Mobots group: Michael Bonani, Daniel Burnier, Mariza Freire, Alexey Gribovskiy, Valentin Longchamps, Stéphane Magnenat, Anne Remillet-Schaller, Philippe Rétornaz, François Rey, Fanny Riedo, Frédéric Rochat and Florian Vaussard. It was a pleasure to work with such a friendly, stimulating and helping team. The tools developed by the group were very helpful to design the multiple prototypes in a fast and efficient way. I especially would like to thank Frédéric for the collaborative work, discussions and ideas during the years passed on this project. I also would like to thank Daniel for his help on many PCBs, and Philippe for his help on the programming of numerous microcontrollers.

I would like to thank Pierre Noirat, Tarek Baaboura and André Guignard for their advices on mechanics, and their manufacturing skills which allowed the realization of the different prototype parts. I also thank Marc Salle and his efficient workshop, and the ACI for the numerous PCBs realizations.

This thesis would not have been possible without the funding of Alstom power service and the Swiss CTI project 8439.1 “Highly Compact Robots for Power Plant Inspection”, and the people working in this project: Francesco Mondada and Frédéric Rochat at EPFL, Gilles Caprari, Fabien Tâche, Wolfgang Fischer, Andreas Breitenmoser, Christoph Hürzeler and Luca Bongulielmi at ETHZ and Roland Moser, Reinhard Fischer, Fernando Silverio and Andres Peralta at Alstom.

I would like to thank all the bachelor and master students who helped me on different projects: Alain Bock, Thierry Barras, Nicolas Yoakim, Xiaoling Wang, Olivier Truong-Dat Nguyen, Valerian Rucher, Nathanael Maegli, Barthélémy Lüthi, Adrian Ionut Prodan, Olivier Marti, Rolando Rodas, Ludovic Daler and Michael Rusterholz.

For all the corrections of my manuscripts, I thank Aline, Alexey, Fanny, Francesco, Frédéric, and Philippe.

I thank all my friends who helped me to “disconnect” from my thesis during exciting outdoor and indoor activities, including Aline, Quentin, Remy, Stephan, Benoit, Chloé, Marc, Géraud, Madeline and all the others.

Finally, I would like to thank my parents and family who always supported me through these long studies, and Aline for all the good moments passed together during the last years.

Contents

1 Introduction

1.1 Motivation

Power plants require periodic inspections to prevent failures and possible shutdowns, which are very costly. Indeed, each unplanned outage day can cause commercial losses above one million dollars per day. Plants are thus closed on a regular time basis for inspection. Non-Destructive Testing (NDT) sensors are used by inspectors to detect possible defects, and parts that may fail before the next inspection are repaired or replaced.

The industrial structures found in power plants are often difficult to access, and sometimes require the dismantling of some parts for the inspectors to access. Having miniature robots able to access difficult remote areas would be very useful in reducing the inspection time and the associated costs. Such robots need advanced mobility, including climbing abilities, to move within these structures and reach the area to be inspected. Once they are located near the parts to be inspected, they need to embed cameras and other sensors in order to perform inspections. Finally, they need to be small, as the available space is often limited. In addition to facilitating access, robots can improve inspection performance by performing more methodical measures than human operators.

1.2 Objectives

The objective of this thesis is to rethink inspection systems, creating new forms of inspection methods compatible with the use of miniature climbing robots. These robots should demonstrate their ability to inspect the different structures found in power plants or similar facilities.

To achieve these goals, a good mobility is required to climb on complex structures and pass obstacles. A vision system is required to control the robot and to perform visual inspections. Non-visual NDT sensors are required to detect non-visible defects. Finally, a high system integration is needed to design miniature robots embedding high mobility, vision and sensing able to inspect industrial structures. For example, on a ferromagnetic part, the use of magnetic adhesion can be combined with an inspection method requiring magnetization to reduce the size of the system.

1.3 Approach

To design a new generation of miniature inspection robots, we decided to follow three main steps.

The first one is to design the climbing part of the miniature system, embedding the required electronics, actuators, sensors and power to reach the inspection area in a safe way. The robots require high mobility, allowing them to move on surfaces of any inclination and to pass obstacles.

The second step is to embed the simplest and most versatile inspection sensor: the camera. A camera allows the robot to perform both visual inspection and to remote control the robots by using their point of view when we cannot see them.

The final step is to embed more sophisticated Non-Destructive Testing (NDT) methods on the robots, to be able to detect non-visible defects.

Most of this work has been done in collaboration with the industry, under a project of the Commission for Technology and Innovation (CTI), between ALSTOM Power Services, the École Polytechnique Fédérale de Lausanne (EPFL) and the Eidgenössische Technische Hochschule Zürich (ETHZ).

I worked on most of the robots with Frédéric Rochat from EPFL. He focused on adhesion systems and mobility concepts, and I focused on the system integration with a particular focus on the sensors, electronics, and software, and on the inspection methods.

1.4 Environments

We decided to design inspection systems for a specific type of environment that can be found in coal-fired power plants. This type of thermal power plants produced 45% of the electricity in the United States in 2010 (Figure 1.1). This work can be easily generalized to other industrial infrastructures.

The simplified working principle of a coal-fired power plant follows these steps (Figure 1.2): the coal is burned in the center of a boiler surrounded by tubes, the water contained in the tubes is heated and generates steam, the high pressure steam is then directed to the steam turbine, which drives the electrical generator.

The water wall is composed of tubes placed around the boiler (Figure 1.3). The tubes are aligned vertically next to each other and can measure more than 100 m in height. Usual diameters are between 2.5 to 5 cm, with bend radii down to 150 mm.

These tubes are exposed to very difficult conditions: fire and heat on one side, and high pressure water and steam on the inside. This leads to different failures that can occur after some time in operation: cracks (Figure 1.4(a)), tube thinning and wall loss (Figure 1.4(b)), corrosion, pitting (Figure 1.4(c)), and erosion. Tubes failures can cause power plant stoppage and shutdown. Thus, inspections are performed during outages to control the state of the tubes. They allow the detection and replacement of those tubes that are in a bad condition.

Another type of element to inspect is the turbines (Figure 1.5). They can have big diameters – over 3 m – with blades up to 1 m. They are exposed to high rotation speeds (up to 60 Hz) and high temperatures, which causes high mechanical constraints. Their good state is critical, as the failure of a blade can cause the destruction of the whole turbine. In addition to more regular visual inspections, a full and detailed inspection lasting around 1 month is thus performed every 3 years.

There are a number of less critical places in a power plant where inspection robots could be useful. For example, the housing of the generator is difficult to access, and contains a complex structure. Most of these structures are composed of ferromagnetic steel.

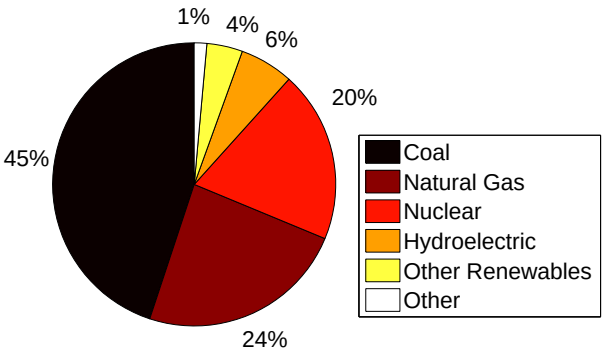

Figure 1.1: United States electricity production sources (source of data: U.S. Energy Information Administration (EIA)).

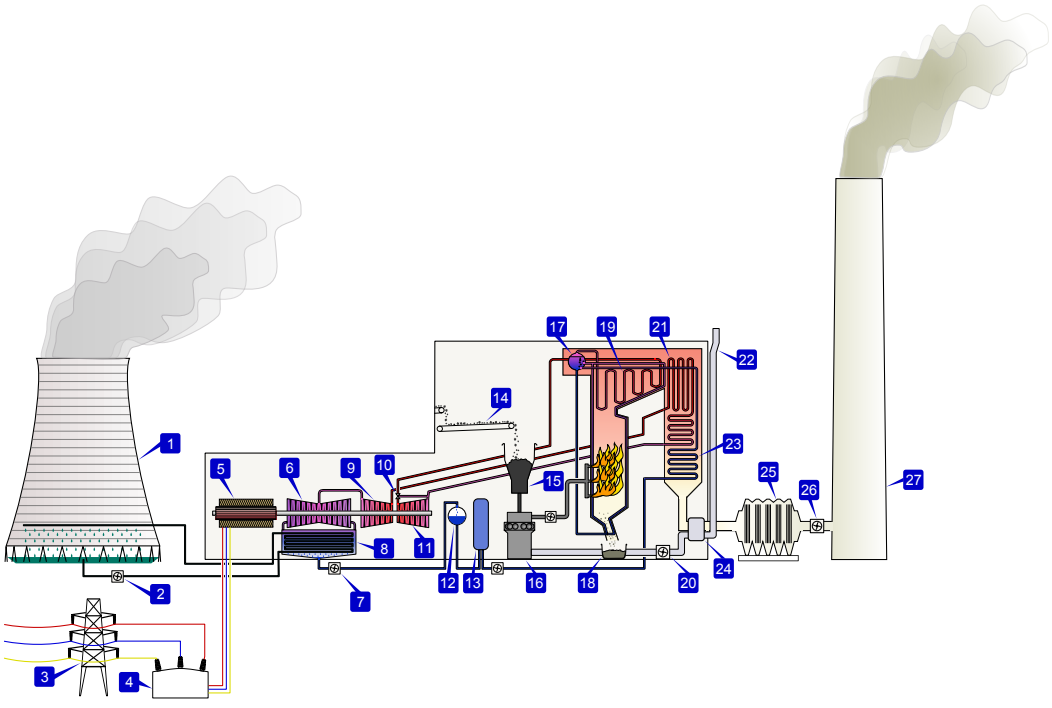

1. Cooling tower
2. Cooling water pump
3. Transmission line
4. Step-up transformer
5. Electrical generator
6. Low pressure steam turbine
7. Condensate pump
8. Surface condenser
9. Interm. pres. steam turbine
10. Steam Control valve
11. High pres. steam turbine
12. Deaerator
13. Feedwater heater
14. Coal conveyor
15. Coal hopper
16. Coal pulverizer
17. Boiler steam drum
18. Bottom ash hopper
19. Superheater
20. Forced draught fan
21. Reheater
22. Combustion air intake
23. Economiser
24. Air preheater
25. Precipitator
26. Induced draught fan
27. Flue gas stack

Figure 1.2: Diagram of a coal-fired power plant (source: Wikipedia).

Figure 1.3: Example of boiler tubes of 50 mm diameter.

(a) Tube cracks (source: Kennametal)

(b) Tube corrosion (source: Power Corrosion Consultants)

(c) Tube pitting (source: Consultant Surveyor)

Figure 1.4: Boiler tubes failures.

Figure 1.5: Example of steam turbine (source: Wikipedia).

1.4.1 Obstacles

Based on the different environments we described, we made a simplified list of the possible structural geometries we can encounter.

The first one is a simple plane, with a measure of its angle of inclination as shown in Figure 1.6. Transitions between two surfaces can be found as inner corners (concave, Figure 1.7(a)), outer corners (convex, Figure 1.7(b)) and surface flips (Figure 1.7(c)). Moving on tubes or blades implies convex (Figure 1.8(a)) or concave (Figure 1.8(b)) curvatures. Moving in tubes also requires to know their internal diameter and minimum radius bends (Figure 1.9). Smaller scale obstacles such as solders (Figure 1.10) or paint drops are present on most structures.

In this thesis, we will describe the mobility of the climbing robots and systems using this list of obstacles.

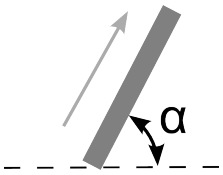

Figure 1.6: Surface inclination angle: 0° on flat, 90° up a wall, 180° on the ceiling, 270° down a wall.

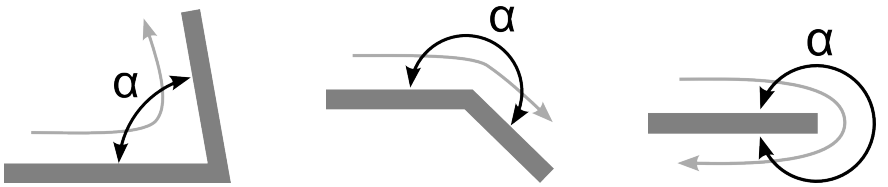

(a) Inner corner: $0 < \alpha < 180°$ (concave angle).

(b) Outer corner: $180 < \alpha < 360°$ (convex angle).

(c) Surface flip: $\alpha = 360°$.

Figure 1.7: Inner and outer transitions.

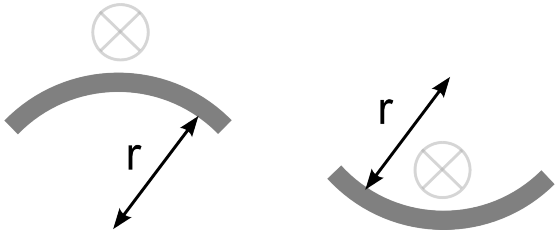

(a) Convex curvature.

(b) Concave curvature.

Figure 1.8: Obstacles curvatures.

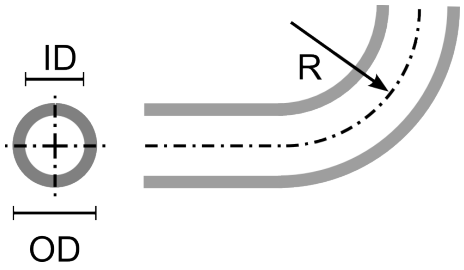

Figure 1.9: Boiler tube specifications: standard inner diameter $25 < ID < 50$ mm, outer diameter OD, minimum radius $R > 150$ mm.

Figure 1.10: Solder making an obstacle of height h.

1.5 State of the art

Inspection robots for industrial structures require a locomotion system, an adhesion system and an inspection system including vision. The state of the art of these different requirements is shown in the following sections. This state of the art description focuses on inspection robots of small size, i.e. with a maximum dimension of 50 cm.

1.5.1 Climbing robots

To reach the inspection location, in most situations the robots need to climb. Climbing robots need a locomotion method and an adhesion principle. The main possibilities are described in the following sections.

1.5.1.1 Locomotion

Climbing robots can be designed using several different locomotion principles. They can be classified in six main categories [CJHH10]:

- Wheel
- Track
- Leg
- Translation
- Cable
- Combination

Wheeled and tracked robots use rolling as basis movement. This approach has the advantage of being a continuous movement, and is usually easy to control.

Legged and translation are point to point displacements. Translation locomotion refers to inchworm like movements, where the body is changing size between two grippers. These locomotion types can be more difficult to control, as the movement is not continuous and the different legs must be synchronized. But it has the advantage of agility, which can be useful in complex environments.

Cable locomotion refers to cable-cars and similar systems. At least one cable needs to be anchored to allow the robot to move on it. Thus, the environment needs some modifications for the robot to move in it.

Hybrid systems exist combining different principles, having wheels at the end of legs for example.

1.5.1.2 Adhesion systems

Climbing robots need an adhesion system to move on very different structures. Adhesion should allow them to stick and climb on structures such as walls, ceilings and other obstacles. Many different methods and solutions exist to create an adhesion force. They can be classified by the nature of the involved forces in five main categories, as found in [LM08]:

- Pneumatic
- Magnetic
- Mechanical
- Chemical
- Electrostatic

The next sections show details on these different forces. As we are interested in miniature robots, only small robots examples are chosen as far as possible. As the environments we are interested to climb in are ferromagnetic, the main focus is done on magnetic forces.

Pneumatic

A pneumatic adhesion force is created by a difference of pressure, which can be generated passively or actively. Pneumatic adhesion can be used on almost all surface types. Most of the systems are active and consume a lot of energy.

Passive suction cups can be used, with legged locomotion such as the CLAUS robot for example [BABE08] (Figure 1.11(a)). Such suction cups have the advantage of not consuming energy during holding, but thex need flat and non-porous surfaces to prevent leakage.

Active systems exist to overcome leakage, and are mainly found on wheeled robots. The Alicia II robot uses a vacuum chamber to create the adhesion force, with flexible seas ensuring the airtightness [Lon04] (Figure 1.11(b)). One problem of theses vacuum chamber is the seals manufacture and wearing, as a failure is critical for the adhesion force.

(a) The CLAUS robot using passive suction cups (source: [BABE08]).

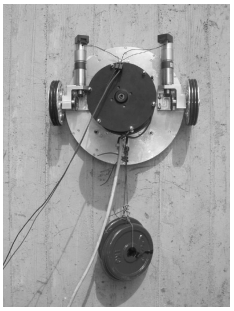

(b) The Alicia II robot using a vacuum chamber (source: [Lon04]).

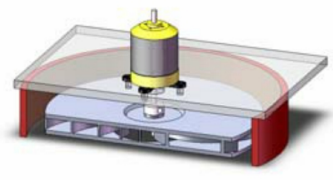

(c) The Alicia VTX vortex active suction cup design (source: [BBLM08]).

Figure 1.11: Pneumatic adhesion robots.

The Alicia VTX robot is using a “vortex active suction cup” created by a centrifugal fan [BBLM08] (Figure 1.11(c)). This technique does not require a sealing to create a strong force. It is thus easier to pass over irregularities and small obstacles, and the seal is not exposed to wearing.

Rachcov and al. developed an hybrid “pedipulator” composed of two grippers: a concentric vacuum gripper and a sealing gripper [RMDA02]. The first one offers good performances over porous surfaces, and the second one over rough surfaces. Mixing different adhesion techniques is very interesting to adapt to various surfaces.

Magnetic

Magnetic forces are created between magnets or electromagnetic coils (electromagnets) on ferromagnetic materials, such as iron, steel and nickel.

A first possible solution to use magnetic adhesion for mobility is to use magnets fixed on the frame of the robot. An example is found on the wheeled robot of Oliveira and al. [OSB10]. This robot can adjust dynamically its adhesion force by changing the distance between the magnets and the surface. An advantage of this solution is that the magnets are not in contact with the ferromagnetic surface, and do not gather ferromagnetic dust. The Mag-Foot robot can walk upside down, using magnets at the end of each legs and a clever design to detach its feet passively [MA09] (Figure 1.12).

Magnetic wheels are another solution. A standard magnetic wheel is composed of a magnet placed between two flux guides [Guy72] (Figure 1.13(a)). The magnetic field closes on any ferromagnetic surface near the wheel and creates an adhesion force. Using a ring shaped magnet can help reducing the weight [YDAL10] (Figure 1.14(a)). An advantage of the magnetic wheels is that the adhesion force is strong, as the air gap is small. However,

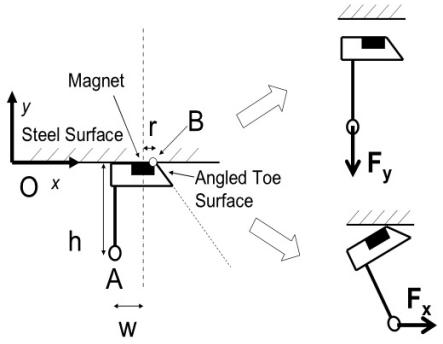

Figure 1.12: The Mag-Foot magnetic legged robot (source: [MA09]).

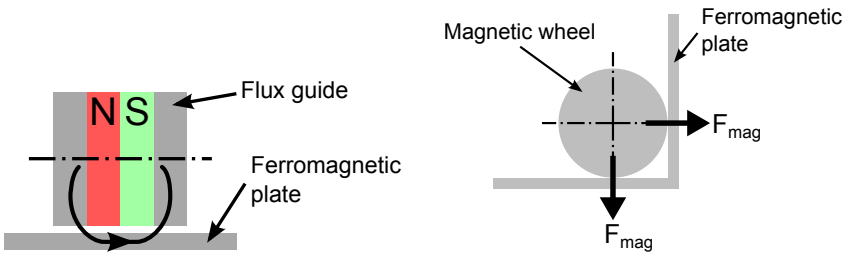

(a) Classic magnetic wheel design. (b) Magnetic wheel blocked in a corner.

Figure 1.13: Magnetic wheel concept and corner problem.

as the force is strongly dependent to the air gap, it can reduce a lot if the wheel passes over a non-ferromagnetic obstacle. Another disadvantage is that it gathers ferromagnetic dust which is difficult to remove.

Inner corner transitions is a problem for magnetic wheels: a strong force keeps the wheel blocked inside the corner (Figure 1.13(b)). A solution is needed to release the force from the old surface. It can be done passively using a multiple wheels configuration [FCSM09], or by using an eccentric outer tire [KYK+95] (Figure 1.14(b)). It can be done actively using mechanical lifters as the MagneBike uses [TFC+09] (Figure 1.14(c)), or by actively controlling the position of the wheels for example [FTS07].

Caterpillars have good performances on uneven terrain, they adapt better than wheels to small obstacles, and can pass over gaps easily. The friction force is also increased compared to wheels. Caterpillars over magnetic wheels are used by Moser and al. [MM07]. In this case the caterpillars have the additional advantage of protecting the wheels from ferromagnetic dust. Caterpillars including magnets have many working examples on vertical walls: the robot from Shen and al. is climbing on oil tanks [SGS06], the SIRUS robot [MSF+08] and the robot from Nagaya and al. can move on curved surfaces [NKY+08] (Figure 1.15(a)). Obstacles passing and ceiling moving remains difficult using magnetic caterpillars only, due to the peeling effect, as a small force perpendicular to the surface is sufficient to detach the whole caterpillar (Figure 1.15(b)).

Electromagnets can be used instead of magnets. Their advantage is a possible fast tuning

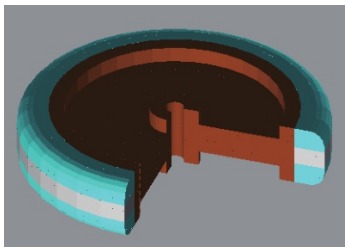

(a) Ring magnetic wheel for reducing the weight (source: [YDAL10]).

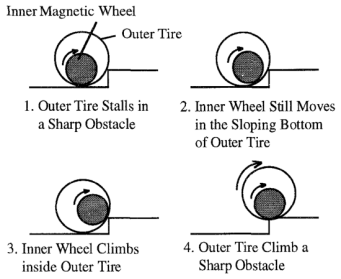

(b) Magnetic wheel outer tyre (source: [KYK+95]).

(c) The MagneBike (source: [TFC+09]).

Figure 1.14: Magnetic wheels variants and robot.

(a) Robot from Nagaya and al. (source: [NKY+08]).

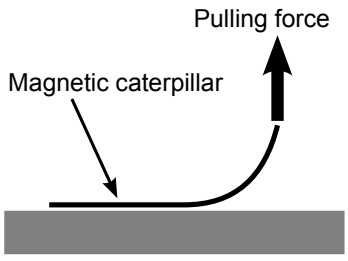

(b) The peeling effect: a small force is sufficient to detach the whole caterpillar.

Figure 1.15: Magnetic caterpillars.

of the adhesion force, which is very useful for legged robots. The main disadvantage is a high electric consumption. An example is the Rest II robot: it has 4 legs, each having an electromagnet [AAF+08]. It can move on ferromagnetic surfaces of any inclinations, but requires a complex locomotion using 4 legs and 12 degrees of freedom.

Another way to control the adhesion force is to use magnetic switchable devices [Coe02]. The idea of such system is to have an adhesion force created by a magnetic system containing a magnet. Changing the magnetic flux path by moving a part of the system allows to create or to cancel the adhesion force on a contact surface (Figure 1.16(a)). This concept is used in the Neptune robot [Sch95] (Figure 1.16(b)). Compared to electromagnets, such systems have the advantage of requiring energy only to switch the force on or off, and not to create the adhesion force.

Mechanical

Gripping mechanisms can be used on structured environments [MGSW09]. This type of adhesion is prone to legged robots: usually one leg is moved and secured before moving the next one [BGJ05] (Figure 1.17(b)). However, the control can become difficult. It is energy efficient, as no energy is needed to keep the holding force once a claw is closed for example. Hooks are used by the Lemur IIb robot, which is able to free climb walls using

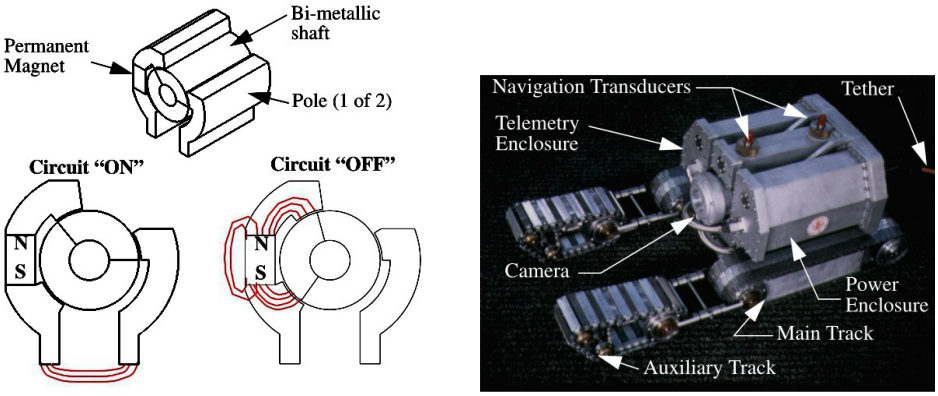

(a) (b)

Figure 1.16: Magnetic Switchable Device (a) from the Neptune robot (b) (source: [Sch95]).

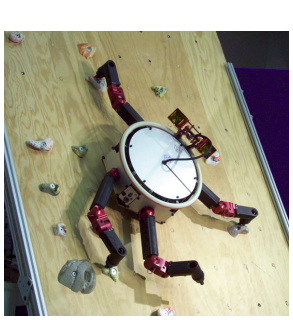

(a) The free climbing Lemur IIb robot (source: [KOA+06]).

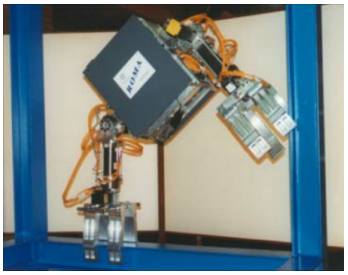

(b) The ROMA II robot using claws (source: [BGJ05]).

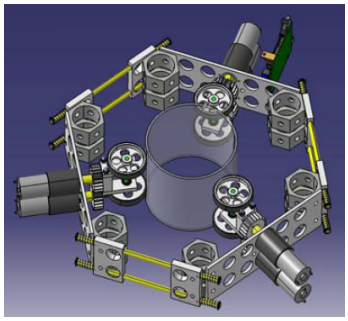

(c) The pole climbing robot from Rodriguez and al. (source: [LBP08]).

Figure 1.17: Mechanical adhesion robots.

holds like a climber [KOA+06] (Figure 1.17(a)). For climbing on cylindrical elements, the adhesion force can be created by pushing from different sides, as does the robot from Rodriguez and al. [LBP08] (Figure 1.17(c)).

Tube climbing

Inside tube climbing is a kind of mechanical climbing, as the main used technique is to push on the sides of the tube to create an adhesion force. Propulsion wheels can be placed longitudinally [Cho02], or having an helical motion [Jam05]. Caterpillars can also be used, and can help steering the robot in T-shaped bifurcations [YSHEJBJ08] (Figure 1.18(a)). Most of the tube robots use a modular construction with flexible connections to allow bends passing [PDvdP+08]. Most of these robots move in 50 mm tubes or bigger, which is larger than the aimed 25 mm boiler tubes.

Smaller robots can pass in 25 mm tubes, as the Toshiba robot [Suz99] (Figure 1.18(b)). The micro robot from Tsuruta and al. has a diameter of only 10 mm [TSK01] (Figure 1.18(c)), and moves with an inchworm motion. It communicates and gets its energy wirelessly. However, these small robots are slow and adapt to very small diameter variations only.

Chemical

Adhesive tapes and especially gecko-inspired synthetic dry adhesive can be used for adhesion force. The later imitates gecko finger surface, and consists of micron-scale diameter polymer fibers (Figure 1.19(a)).

Robots using adhesive caterpillars show good performances on different surface types [GSC+06, MMS04] (Figure 1.19(b)). The Waalbot is using dry elastomer adhesives on rotating legs [MS07] (Figure 1.19(c)). The Geckobot uses elastomer adhesive and gecko inspired cinematic to climb walls up to 85° of inclination [UUAS06].

The main problem of these adhesives is their sensitivity to dust and the resulting loss of performances after a short use.

Electrostatic

An electrostatic force is created when a high voltage (over 1 kV to be significant) is applied between two parts. It is very promising, as the force is created on insulator and conducting materials. Furthermore the energy consumption is very low (less than 1 W) despite the high voltage needed.

It can be used as adhesion force for robots, and examples exist with inchworm movements and with caterpillars [PPS+08, YNH07] (Figure 1.20). However, the achieved forces are

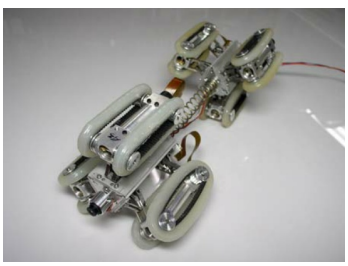

(a) The robot from Young and al. (source: [YSHEJBJ08]).

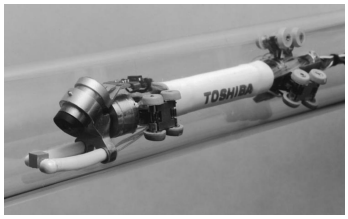

(b) The Toshiba robot (source: [Suz99]).

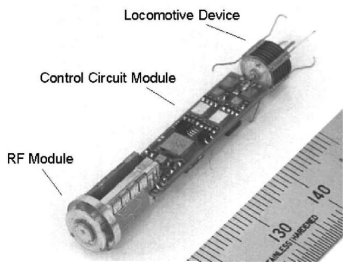

(c) The robot from Tsuruta and al. (source: [TSK01]).

Figure 1.18: Tube climbing robots.

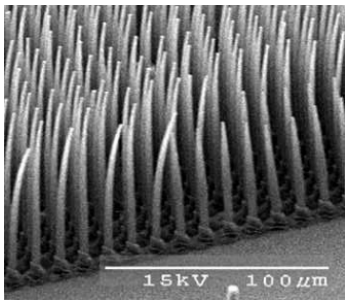

(a) Gecko-inspired polymer fibers (source: [GSC+06]).

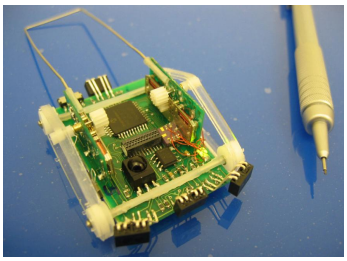

(b) Adhesive caterpillars robot from Greuter and al. (source: [GSC+06]).

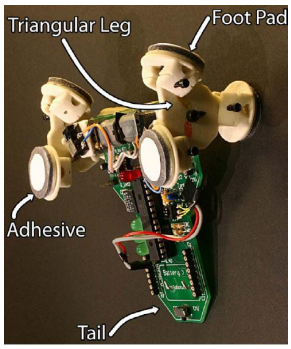

(c) Waalbot using dry elastomer adhesives on rotating legs (source: [MS07]).

Figure 1.19: Chemical adhesion robots.

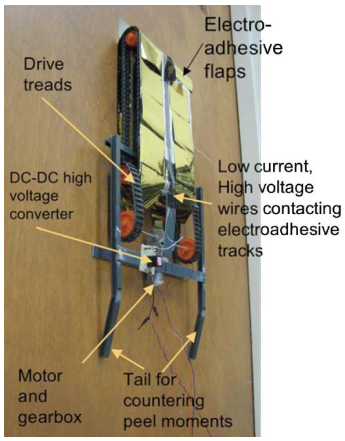

Figure 1.20: Electrostatic force robot from SRI International (source: [PPS+08]).

low, and the robots need to be lightweight to climb using such adhesion system.

1.5.1.3 Other locomotion systems

Caterpillars with variable shape

Caterpillars are interesting for difficult terrain. They can adapt to it and pass over holes easier than other systems. However, their shape is not adapted to all configurations, and changing the shape of the caterpillar actively can be very interesting, as shown by Paillat and al. [PLH08] (Figure 1.21(a)) and Ben-Tzvi and al. [BTIG07] (Figure 1.21(b)).

Flying

Flying can be a good option if there is enough available space, and if the displacement of air is not disturbing the environment. The robot developed by Nishi and al. can fly to a wall and roll on it [NM99]. The SmartCopter can inspect power lines visually and with thermal imaging [BXQ+10]. Indoor flying is also developing and showing interesting results and possibilities, as the quadrotor used by Hurzeler and al. [HMN+08].

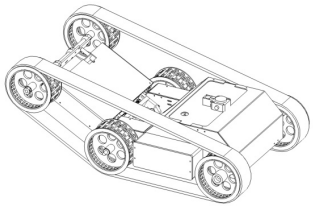

(a) Variable geometry tracked vehicle from Paillat and al. (source: [PLH08]).

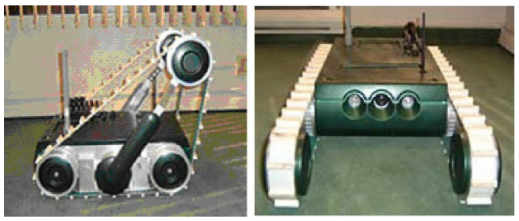

(b) Reconfigurable tracked mobile robot from Bentzvi and al. (source: [BTIG07]).

Figure 1.21: Variable geometry caterpillar robots.

1.5.2 Non-destructive testing

Non-Destructive testing (NDT) is needed for inspecting parts without causing damages. It allows evaluating the state of the parts, and then decide if they must be changed or not before the next outage. There are numerous available techniques, which can be classified in 11 groups [Lue08]:

- Visual and optical testing
- Thermal testing
- Liquid penetrant testing
- Leak testing
- Diverted magnetic flux testing
- Eddy current testing
- Microwave and terahertz testing
- Ultrasonic testing
- Acoustic emission testing
- Radiographic testing
- Magnetic resonance testing

Inspecting industrial structures requires portable equipments, allowing access to the parts to be inspected. This becomes even more important for inspection robots, for which size and weight is critical. Thus, from all these inspections methods, only a few are used in on-site inspection of industrial structures. We also limit the focus on inspection techniques working on ferromagnetic steel, composing most of the parts from the industrial structures we are interested in [Sad06, Bir01, VV06, BVS+02]:

- Visual testing
- Eddy Current Testing (ET)
- Ultrasonic Testing (UT)
- Magnetic Flux Leakage (MFL)

These four inspection techniques are detailed in the next sections.

1.5.2.1 Visual testing

Visual inspection can give a first impression of the state of the part to inspect, and can detect visible defects such as big cracks or holes. However, vision cannot help detecting

hidden cracks or measuring thicknesses.

Endoscopes can be used to inspect complex parts or tubes (Figure 1.22(a)). They allow accessing closed areas through access holes for example. However, the inspection distance is limited, and depending on the geometry the probe cannot be pushed very far.

Tube inspection robots can use a frontal camera for visual inspection [SMG+10] (Figure 1.22(b)). Using a pan-tilt camera can help looking on the sides of the tube [HMT09] (Figure 1.22(c)), but increases the mechanical complexity. Another solution is to use special optics to get an annular view of the tube [LHJH07] (Figure 1.22(d)).

Structured light is used by Duran and al. to inspect road tunnels [DAS03] (Figure 1.23(a)). A light cone is emitted by the robot, and the image is recorded. As the light circle will deform depending on the tube geometry, a full 3D map of the tube size can be created by interpreting the images. The miniature robot developed by Wu and al. uses a similar principle to map very small tubes (⌀ 10 mm) [EYB09] (Figure 1.23(b)).

1.5.2.2 Eddy current testing

Eddy Current testing (ET) is working on conductive materials. The working principle is the following: a coil driven by an alternative current generates a magnetic field (Figure 1.24). When the coil is placed on a conductive material, Eddy currents are induced in this material. Moving over a defect can change the Eddy currents paths, and thus change the inductance of the coil. Measuring the inductance and interpreting it allows to detect and recognize defects.

Different probes exist for different applications, materials, geometries, etc. (Figure 1.25(a) and 1.25(b)). ET probes can be placed in arrays, to inspect the whole circumference

(a) Endoscope (source: GE Inspection Technologies).

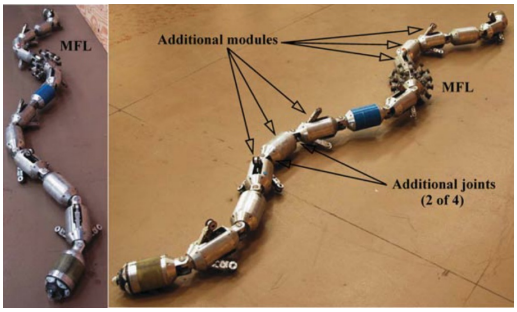

(b) The Explorer pipe inspection robot (source: [SMG+10]).

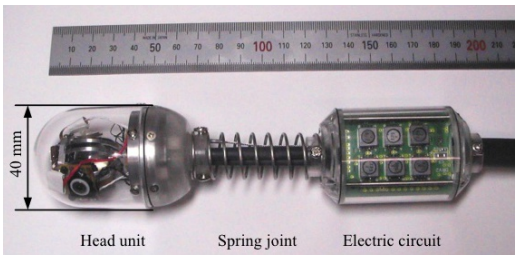

(c) Pan-tilt camera system from Hoshina and al. (source: [HMT09]).

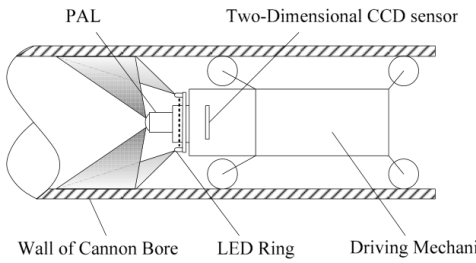

(d) Panoramic optical annular staring inspection from Liefeng and al. (source: [LHJH07]).

Figure 1.22: Visual inspection.

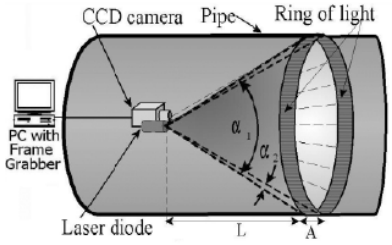

(a) Optical tube mapping from Duran and al. (source: [DAS03]).

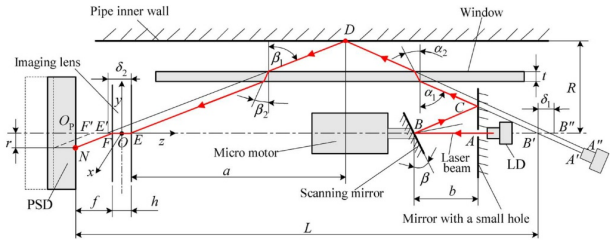

(b) Miniature optical tube mapping from Enqi and al. (source: [EYB09]).

Figure 1.23: Structured light inspection.

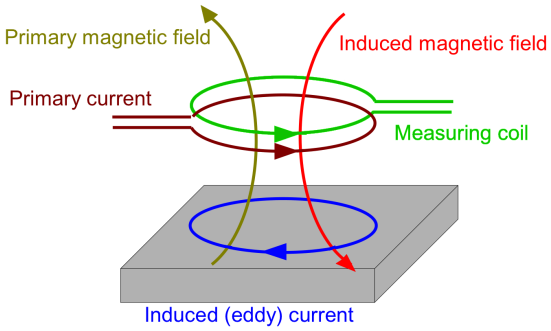

Figure 1.24: Eddy Current inspection principle (source: [Lue08]).

(a) Surface handheld probe (source: Zetec).

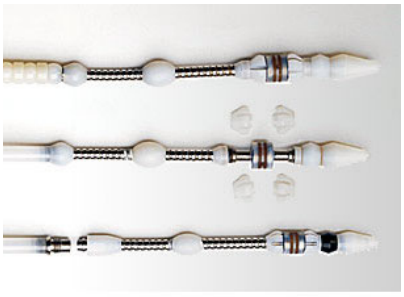

(b) Bobbin tube probe (⌀ 25 mm, source: Zetec).

(c) The TubeCat robot (source: Russell NDE Systems Inc.).

Figure 1.25: Eddy Current inspection.

of large pipes for example [BGP+09].

The TubeCat robot can inspect boiler tubes by remote field testing (Figure 1.25(c)). The difference with standard ET is that the measuring coil is placed at a certain distance from the emitting one. Using this inspection method, the robot can detect pitting in the tube.

1.5.2.3 Ultrasonic testing

Ultrasonic Testing (UT) can be used to look for defects on any material with low sound damping. The thickness can be measured using the time of flight measure (Figure 1.26). A liquid couplant is often used to transmit the sound wave from the probe to the surface.

The robot developed by Mondal and al. can inspect welds on ship hulls [MBS+08, SMB+08] (Figure 1.27(a)). An elastomer dry couplant is used to replace the traditional liquid couplant, which is difficult to implement on a robot. The modular inspection robot platform from Alstom Inspection Robotics (AIR) can carry an ultrasonic probe [ZZM10] (Figure 1.27(b)).

A disadvantage of UT is that the parts must be cleaned or even sand-blasted before inspection. This operation can be reduced using ElectroMagnetic-Acoustic Transducers (EMAT) [Ber03]. Many robots climbing on waterwalls are measuring the tubes thicknesses using this method [BCC+05, PJL02].

The pipeline inspection robot from Wang and al. is using ultrasonic probes on the whole circumference [WCLZ10]. Another solution for smaller tubes inspection is to use an Internal Rotational Inspection Systems (IRIS) [VV06].

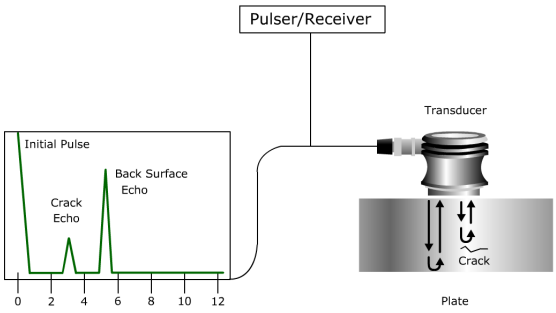

Figure 1.26: Ultrasonic testing time of flight measurement principle (source: NDT Resource Center).

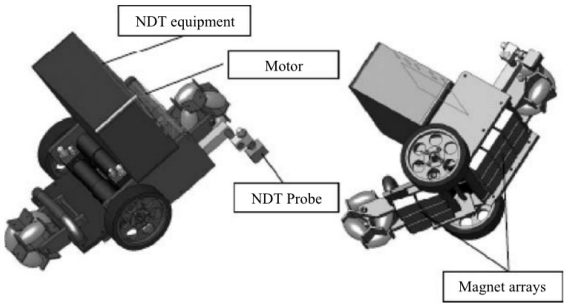

(a) The inspection robot from Mondal and al. (source: [SBS+08]).

(b) Alstom Inspection Robotics (AIR) modular robot (source: AIR).

Figure 1.27: Ultrasonic inspection robots.

1.5.2.4 Magnetic flux leakage

Magnetic Flux Leakage (MFL) testing is working on ferromagnetic materials. The principle is to magnetize the part with a strong magnetic field. The magnetic flux will leak out of the part in defect zones with cracks, holes, etc. (Figure 1.28). Scanning the part with a magnetic sensor allows detecting the defects. As the magnetization can be done using permanent magnets, this inspection method does not need a lot of power. However, it requires strong magnetization and thus big magnets to give good results.

MFL is used in pipelines inspections [BVS+02, BNES97] (Figure 1.29(a)). The wall thickness can also be measured using this technique [ZY07]. Smaller pipes can also be inspected by robots using MFL [Sta07].

The robot from Friedrich and al. is using its magnetic wheels for two functions: magnetic adhesion to be able to climb on ferromagnetic structures, and magnetizing the part to perform MFL inspections [FGHG06]. This robot can move on surfaces of any inclination. A Hall sensor is placed between the magnetic wheels, that allows to inspect a line on the surface when the robot moves. The system can detect holes as small as 1 mm diameter.

Sensing the magnetic flux leakage requires sensors with good sensitivity in low magnetic fluxes. Magnetoresistances are used [CQJ05], as well as Hall effects sensors [JS11]. Arrays of sensors are used to increase the inspected area and thus the inspection speed [HL10, JL08, JJJY11, KL10] (Figure 1.29(b)).

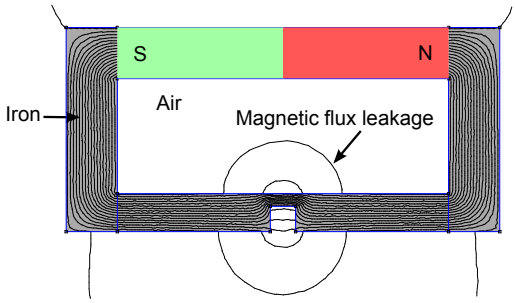

Figure 1.28: Magnetic Flux Leakage (MFL): the magnetic flux leaks outside the magnetized part where defects are located.

(a) PIG used for MFL inspection of pipelines (source: [BVS+02]).

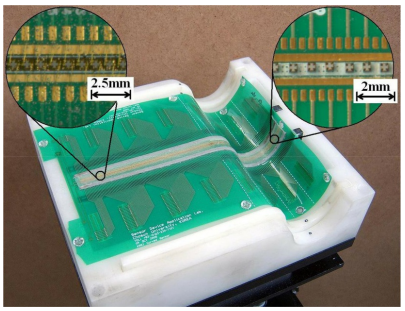

(b) Hall sensor array from Hwang and al. (source: [HL10]).

Figure 1.29: Magnetic flux leakage.

Magnetic particle inspection

Magnetic Particle Inspection (MPI) is a subpart of MFL. Instead of using magnetic sensors, magnetic particles are used to detect the leakage. The particles are put in suspension in a liquid. When dispersed on the magnetized part, they move and gather on places with higher magnetic fields, corresponding to cracks and other defects locations. Using fluorescent particles and UV lighting helps increasing the contrast of the defects (Figure 1.30).

MPI inspections can be done manually, using a hand-yoke for magnetization, and detecting defects visually. Automatic MPI systems are used on production lines [NTTF95].

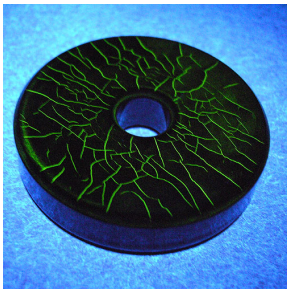

Figure 1.30: MPI test part (source: MR chemie).

2 Magnetic Climbing Robots

2.1 Introduction

This chapter focuses on the design and integration of the mechatronics allowing miniature robots to climb. This is the first step to develop inspection robots and systems able to enter, move within and inspect complex industrial structures. As the target environments are ferromagnetic, we decided to focus our design on robots using magnetic adhesion. Indeed, magnets create a high adhesion force with small volumes and no external energy consumption, which are strong advantages for mobile robots.

The basics of magnetism are reviewed at the beginning of the chapter, showing the main ferromagnetic materials and magnets properties. Magnetic Switchable Devices (MSDs) and their interesting properties for mobile climbing robots are then described. A new method to continuously measure the adhesion force of different magnetic systems is then developed and tested. Sensing the adhesion force allows to increase the safety of the climbing robots, as they can be stopped before falling. Finally, six robots using different mobility principles are presented, illustrating the implementation of the described concepts: two versions of the caterpillar robot Tripillar, two versions of the advanced magnetic wheel robot Cy-mag^{3D}, and two versions of the tube crawler Tubulo. Their mechanics, mobility and electronic design and integration are described. All of these robots embed the required energy and transmission methods to be remote-controlled wirelessly.

The integration of vision sensors and their required electronics are described in detail in Chapter 3.

2.1.1 Magnetism

Magnetism is a physical phenomenon which can create attraction or repulsion forces. It is observable in ferromagnetic materials or around moving electrical charges.

Magnets are the materials that present the strongest magnetic properties. A magnetic field is present around magnets, with field lines going from its north to its south pole (Figure 2.1). Solenoid flowed by electrical current show very similar magnetic fields. Magnets have the advantage over solenoid of keeping stored energy, and thus require no external energy to create an adhesion force.

The magnetic field H is linked to the magnetic flux B by the permeability μ:

$$B = \mu H \tag{2.1}$$

μ is composed of the permeability of vacuum $\mu_0 = 4\pi 10^{-7}$, and the relative permeability μ_r: $\mu = \mu_0 \mu_r$. The relative permeability is high for ferromagnetic materials (>500), which

show strong attraction forces with magnetic fields. It is near 1 for non-ferromagnetic materials, which can be separated in two groups: paramagnetic materials showing small attraction forces ($\mu_r > 1$), and diamagnetic materials showing small repulsion forces ($\mu_r < 1$).

The main source of the magnetization of ferromagnetic materials is the orbital angular motion of the electrons around the atoms' nucleus. Atoms of small regions align and form magnetic domains. Under normal conditions the different domains have random directions, and the resultant magnetic field is zero (Figure 2.2 left). If the material is exposed to an external magnetic field, the magnetic domains will rearrange and align closer to the field direction (center). If the external magnetic field is strong enough, all the domains can align in the same direction (right). When the external field is removed, a remanent magnetization remains. It will stay high for hard ferromagnetic materials, and low for soft magnetic materials.

A hysteresis curve shows the magnetic flux inside the material when exposed to certain field variations (Figure 2.3). The remanent flux points B_R is the point where the curve is crossing the y axis. It corresponds to the magnetic flux left in the material after magnetization. The coercitive force H_C is the point where the curve is crossing the x axis. It corresponds to the field that has to be applied to the material to cancel the remanent flux after its magnetization to saturation. Figure 2.3 shows the hysteresis curve of magnets, hard and soft ferromagnetic materials. A clear differences can be observed between these three material classes, with very different remanent fluxes and coercitive forces. The flux is saturating at high fields, that depend on the materials.

2.1.1.1 Ferromagnetic materials

Ferromagnetic materials are interesting for magnetic applications because they are the only materials that have strong interactions with magnetic fields. Iron, Cobalt, Nickel and some

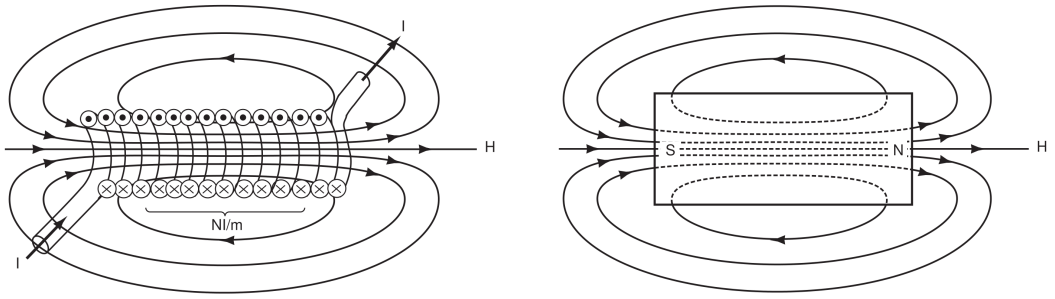

(a) (b)

Figure 2.1: Magnetic field around a solenoid (a) and a magnet (b) (source: [MC00]).

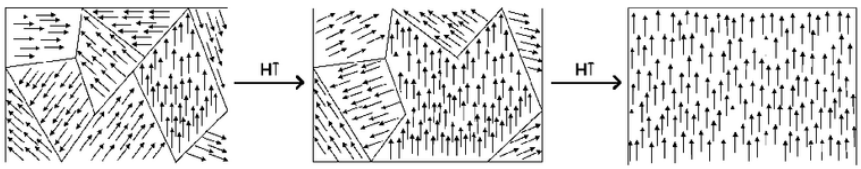

Figure 2.2: Magnetic domains alignment (source: Wikipedia).

rare earths are the main pure ferromagnetic materials. Most of the other materials are alloys composed of these materials.

Table 2.1 shows the relative permeability of different materials and alloys. The highest permeabilities are reached by special alloys used in generators and motors. Nevertheless these materials are expensive and difficult to machine. Mild steels (low carbon steels) show good permeabilities and are machined using standard tools.

A common idea is that stainless steel is not ferromagnetic, as the most used form of it, austenitic stainless steel, is not ferromagnetic. However, martensitic steels are a little magnetic ($50 < \mu_r < 400$), and ferritic steels show very good ferromagnetic properties ($500 < \mu_r < 3000$).

2.1.1.2 Magnets

Table 2.2 shows the principal characteristics of different magnet types, which are: the remanance (B_R), the coercivity (H_C), the energy product ($(BH)_{max}$) and the Curie temperature (T_C). The remanance is the remanant magnetic flux after magnetization. The coercivity is the required magnetic field to reduce the magnetization to zero. The energy product is the density of magnetic energy. The Curie temperature is the temperature at which the magnet looses its magnetization. Figure 2.4 shows the energy product evolution over time of the main magnet types. We see clearly the gain of the rare earth magnets

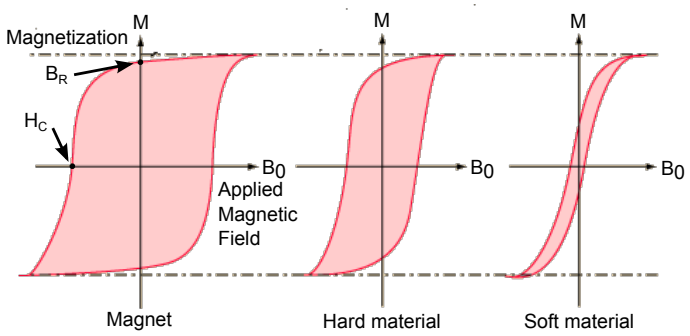

Figure 2.3: Hysteresis curve of magnets, hard and soft ferromagnetic materials (source: [YH92]).

Table 2.1: Different materials relative permeabilities (source: [MC00])

Material	μ_r
Superpermalloy	1000000
Mu-metal	100000
Permalloy	8000
Iron pure (99.8%)	5000
Mild Steel (0.2% Carbon)	2000
Ferritic stainless steels	500-3000
Nickel (99%)	600
Martensitic stainless steels	50-1000
Cobalt (99%)	250
Austenitic stainless steels	1.002-4
Air	1

Table 2.2: Different magnet types properties (source: [PJHN08])

Magnet	$\mathbf{B_R}$ **[T]**	$\mathbf{H_C}$ **[kA/m]**	$\mathbf{(BH)_{max}}$ **[kJ/m^3]**	$\mathbf{T_C}$ **[°C]**
$Nd_2Fe_{14}B$	1.0-1.4	750-2000	200-440	310-400
$SmCo_5$	0.8-1.1	600-2000	120-200	720
$Sm(Co,Fe,Cu,Zr)_7$	0.9-1.15	450-1300	150-240	800
Alnico	0.6-1.4	275	10-88	700-860
Sr-ferrite	0.2-0.4	100-300	10-40	450

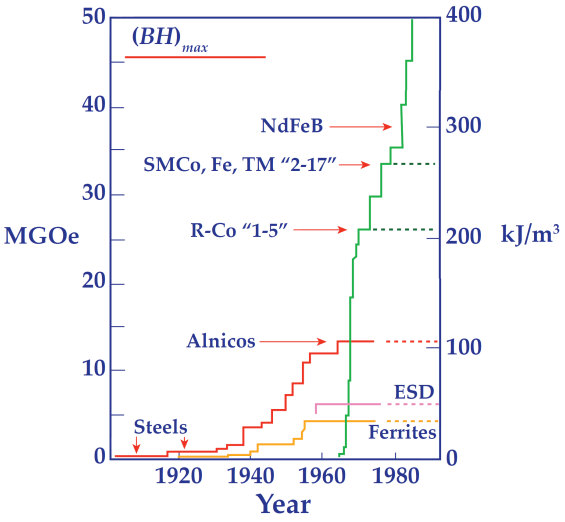

Figure 2.4: Development of permanent magnets using the laboratory record values of energy product (source: [Str90]).

(green curve) over the other magnet types.

Neodymium magnets (NdFeB) have the strongest magnetic fields, but have a low Curie temperature. Samarium-Cobalt magnets are weaker and more expensive, but have a higher Curie temperature, and are thus used for applications with working temperature higher than 200°C. Older Alnico and Strontium ferrite magnets have much lower coercivities, which means they can be demagnetized easily.

Neodymium magnets (NdFeB) were developed in the 80s, and are now the most used magnets. They are produced by sintering rare-earth powders. A coating is often applied on the magnet to prevent corrosion. Neodymium magnets have different grades, coded by a letter and a number. The letter indicates the maximum temperature of use. The number indicates the maximum energy of the magnet in MGOe (1 MGOe = 7.96 kJ/m^3). The higher is the usable temperature, the lower is the maximum energy. The maximum achievable energy of each temperature categories are shown in Table 2.3. For room temperatures, the N grade gives the strongest magnetic fields, N52 being the highest commercial grade at the moment. As the record grade of N56 was achieved in 2002 by Rodewald and al. [RWKU02], there is not much improvements to be expected in the near future for this type of magnets.

Magnets are very difficult to machine after production, as they are composed of powders which disintegrate under classic machining tools. Limited modifications such as holes can be performed by electrical discharge machining. However, magnets of custom shapes can

be easily obtained at low cost.

2.1.2 Magnetic switchable devices

Standard magnets and magnetic systems have strong adhesion forces, but are difficult to remove for the same reason. To detach them, the same force that they hold has to be applied. This is not suitable for miniature mobile robotic applications, as this needs a lot of energy, requiring strong actuators or big reduction systems.

Magnetic switchable devices (MSDs) remove this disadvantage, by giving the possibility to turn off the adhesion force easily [RSB+10]. MSDs are used in the industry to hold tools in workshops for example (Figure 2.5).

The concept of MSD is shown in Figure 2.6. A magnet is enclosed in a ferromagnetic stator. By rotating the magnet, the flux is either closing outside of the system, which creates an adhesion force (this state is called active or on), or the flux is closing inside the system, which gives no force (this state is called inactive or off). On ferromagnetic surfaces, the flux path is similar in all magnets positions, and the magnetic torque applied on the magnet is very low. A very low force is thus needed to switch between on and off positions compared to the adhesion force. On non-ferromagnetic surfaces, the flux path is no longer similar in all directions. It closes better in the off position of the magnet, which is thus attracted to this position. The rotation torque is thus higher on non-ferromagnetic surfaces.

Table 2.3: Properties of Neodynium magnets on the market (source: `http://www.supermagnete.ch`)

Quality	$\mathbf{B_R}$ **[T]**	$\mathbf{H_C}$ **[kA/m]**	$\mathbf{(BH)_{max}}$ **[kJ/m^3]**	$\mathbf{T_{use}}$ **[°C]**
N52	1.42-1.47	860-995	380-422	80
50M	1.4-1.46	860-995	374-406	100
48H	1.37-1.42	860-995	358-382	120
45SH	1.32-1.37	860-995	342-358	150
40UH	1.26-1.29	860-995	303-318	180
35EH	1.17-1.21	860-915	263-279	200

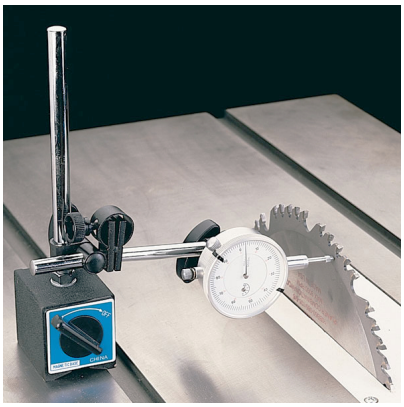

Figure 2.5: Magnetic Switchable Device (MSD) used to hold tools (source: `http://www.woodcraft.com`).

The MSD showed in Figure 2.7 has a size of 5.7x5.7x16 mm for a weight of 4 grams[1]. Its adhesion force on steel is up to 38.4 N, with an activation torque of only 1.74 mNm. The torque in air is of 5.63 mNm.

There is a significant difference between the energy to turn off the system, or to pull it up. The energy for switching the MSD (torque times rotation angle) is of 1.4 mJ. If the system is pulled in on position, the energy (force times distance) rises to 46.2 mJ. This MSD needs thus 30 times less energy to detach than an equivalent magnetic system.

2.2 Magnetic adhesion monitoring

Being able to attach and detach from a structure are important aspects for a climbing system, but the safety of the system is strongly based on the reliability of the adhesion system. Therefore, measuring the current adhesion force is a key issue for a climbing robot. The adhesion force can change a lot depending on the material, the paint thickness, or because of screw heads that can rise above the surface. Thus, if the measured force is too low, the system can react accordingly, avoiding for instance to fall. Falling can generate damages to the robot and, worse, to the inspected structure, which is unacceptable. Therefore a sensor of adhesion force is a key component of an adhesion system. This section presents the development of this type of sensor and its integration into three different magnetic systems.

To measure the adhesion force, we exploit the fact that the flux paths around a magnetic system alter when a ferromagnetic object is approached, as the magnetic flux will tend to pass through the highest permeance path. Thus, one solution to indirectly measure the

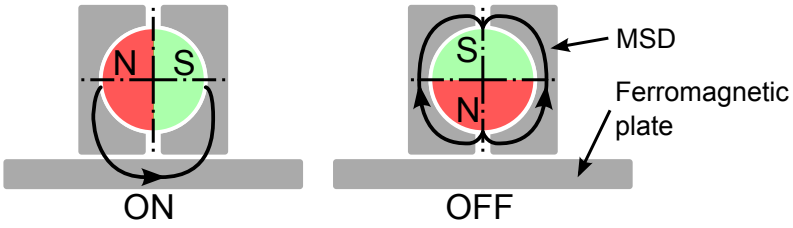

Figure 2.6: Magnetic Switchable Device (MSD) concept.

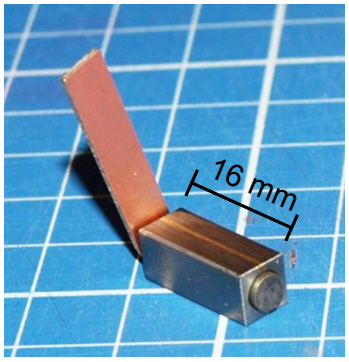

Figure 2.7: The classic MSD measures 5.7x5.7x16 mm, weights 4 grams and holds up to 38.4 N.

[1]MSDs for mobile robots applications were developed by Frédéric Rochat in his PhD [Roc11].

adhesion force is to measure the flux intensity near the magnetic system. The measuring position needs to be located where the magnetic flux changes depending on the adhesion force. It also has to be where the magnetic flux is within the range of the sensors.

Linear Hall effect sensors are used to measure the magnetic flux, and have a typical range of ±100 mT. For example, the SS49E linear Hall sensor from Honeywell is a good sensor for mobile robotics. It is small, with a size of only 4.1x4.1x1.6 mm, and even smaller for the surface mount package: 4.4x2.4x1.3 mm (Figure 2.8(a)). It has a small energy consumption of 5 mW, with a supply voltage between 3 and 6.5 V. The measuring range is around ±100 mT, with a sensitivity of 14 mV/mT (Figure 2.8(b)). The following equation can be used to convert the measured voltage in magnetic flux density:

$$B = \left(U_{meas} - \frac{U_{alim}}{2} \right) \frac{1}{s} \tag{2.2}$$

where B is the magnetic flux density [T], U_{meas} is the measured voltage [V], U_{alim} is the sensor supply voltage [V], and s is the sensitivity of the sensor [mV/mT].

We used simulation and test to optimize the sensor position for different magnetic systems. The next sections show the design and results of magnetic flux monitoring for three different cases: a single magnet, an MSD and a magnetic wheel.

2.2.1 Single magnet

For the first case study of magnetic flux monitoring, a single cubic magnet is used, with its magnetization axis parallel to the surface. Figure 2.9 shows the flux intensity in the y direction in two 2D simulations of the magnet in air and close to a steel plate. The simulations are performed using the software COMSOL Multiphysics[2].

The simulations allow to find possible sensor positions. A good position of the flux sensor is near one pole of the magnet, measuring the flux perpendicularly to the surface (y direction), as shown in Figure 2.9. It is placed at mid-height of the magnet, so that the flux is null when the magnet is in air, as the flux is symmetrical around the magnet in this case. We can simulate the magnetic flux at this location and the adhesion force of the system using such a configuration. Varying the thickness of the plate (0.1-5.1 mm) with a fixed air gap (0.5 mm) gives a linear relation between the flux and the force (Figure 2.10, blue). Varying the air gap (0.5-15.5 mm) with a constant plate thickness (1 mm) gives another non-linear curve (Figure 2.10, black).

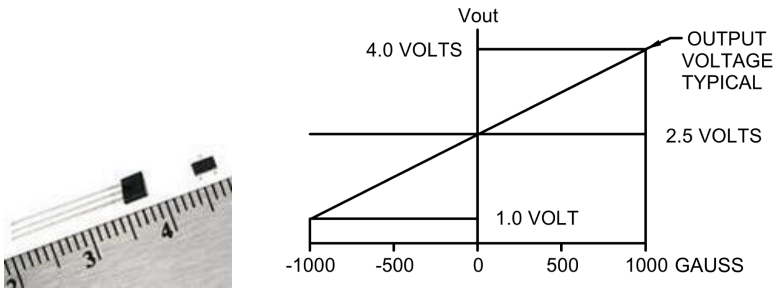

(a) Packages. (b) Transfer characteristics (source: Honeywell).

Figure 2.8: SS49E linear Hall sensor.

[2]COMSOL - Multiphysics Modeling and Simulation Sowftware: `http://www.comsol.com/`.

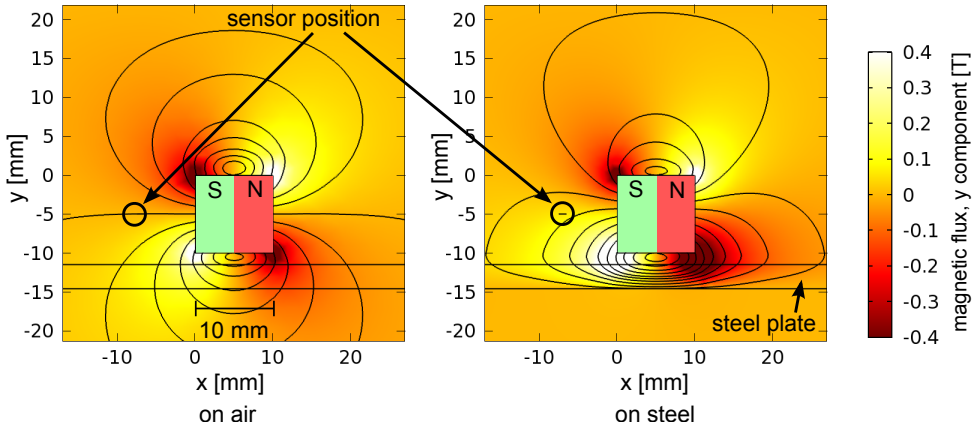

Figure 2.9: 2D simulation of the magnetic flux in the y direction around a single magnet (10x10x10 mm) in air and above a steel plate. A possible sensor position is shown.

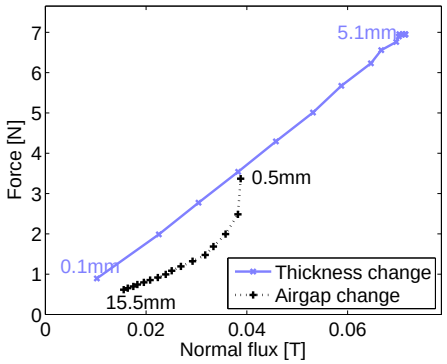

Figure 2.10: Simulation of a single magnet adhesion force depending on the magnetic flux, for a steel plate with varying thickness or air gap.

The difference between the two curves shows that only sensing the flux beside a magnet cannot measure the holding force. However, if we put some restrictions, like keeping a constant air gap, the force is linked to the measured flux. Depending on the application, the curve can be measured and calibrated, which allows to measure the holding force.

2.2.2 Magnetic switchable device

Magnetic flux sensing also applies on MSDs. A classic MSD is chosen, with a size of 5.7x5.7x16 mm (already shown in Figure 2.6). Figure 2.11 shows the flux intensity in the y direction in two 2D simulations of the active MSD in air and close to a steel plate. We observe that the flux changes on the top side of the MSD depending on the presence of the steel plate. When the MSD is in air, the flux is symmetrical on both sides of it. When a ferromagnetic material is present on one side, more flux closes in the material, and the flux reduces on the other side. Thus, the higher the adhesion force, the lower the flux will be on the other side.

We measured the magnetic flux of a real MSD using a linear Hall sensor for the following different cases: on and off in the two magnetizing directions, on air and steel. The

sensor position used for the measures is shown in Figure 2.11. The results are shown in Figure 2.12(a). In the off position, the flux are small and similar on air and steel (around 5-10 mT). We expected for such a result, as all the flux should be enclosed in the MSD. In the on position, the flux on steel is around half the one on air.

Figure 2.12(b) shows the magnetic flux depending on the adhesion force of the MSD placed on a steel plates with variables air gaps. Five measures were done for each point of the graph. The error ellipses represent the absolute maximum error of the measures. We see that there is a nonlinear relationship between the two variables. Thus, by knowing the magnetic flux value, we can compute the adhesion force.

However, as we saw in the previous section, the curve may be different for different conditions. Thus, the curve must be calibrated for the target environment before use. This is feasible, by measuring the adhesion force and magnetic flux for different conditions on the target environment.

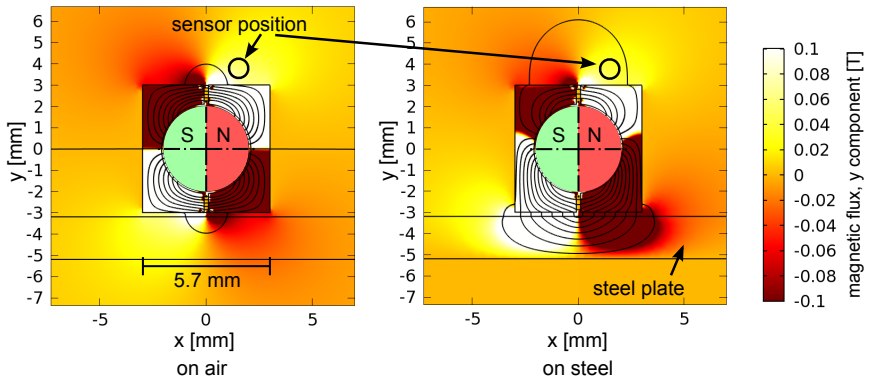

Figure 2.11: 2D simulation of the magnetic flux in the y direction around an MSD in on position in air and on a steel plate. A possible sensor position is shown, on the opposite side of the adhesion surface.

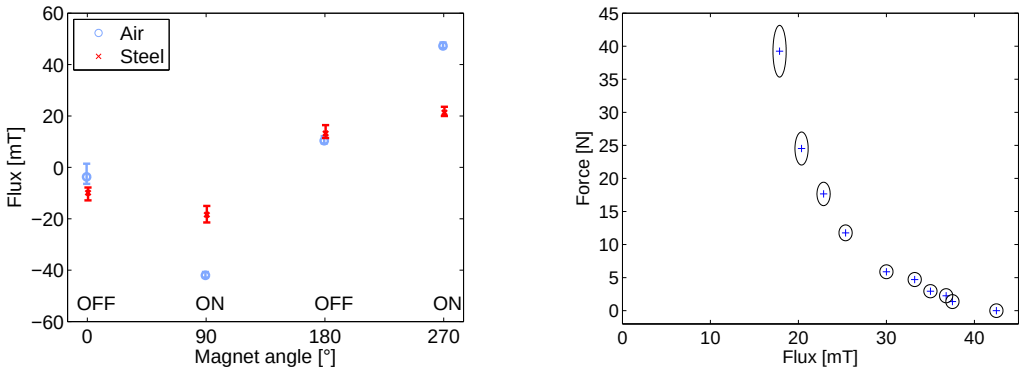

(a) Measures of the magnetic flux on air and steel for different magnet positions.

(b) Measured adhesion force depending on the measured flux on a steel plate of 5 mm thick for varying air gaps.

Figure 2.12: Magnetic flux monitoring of an MSD.

2.2.3 Magnetic wheel

The same principle of flux measurement can also be applied to wheels. The tested wheel has a diameter of 10 mm, a width of 20 mm and a magnet of 10 mm width placed between 5 mm width steel flux guides[3].

In this case, the simulations show that an interesting placement of the Hall effect sensor is above one steel part of the wheel, measuring the flux parallel to the axis of the wheel (Figure 2.13).

Measures were performed with a sensor placed at this location on a real wheel. The force as a function of the measured flux is plotted in Figure 2.14. The curve is very similar to the one obtained for the MSD. It is thus also possible to monitor the holding force of a wheel by measuring the magnetic flux around it. The force can be computed by measuring the flux and interpolating the curve showed in Figure 2.14.

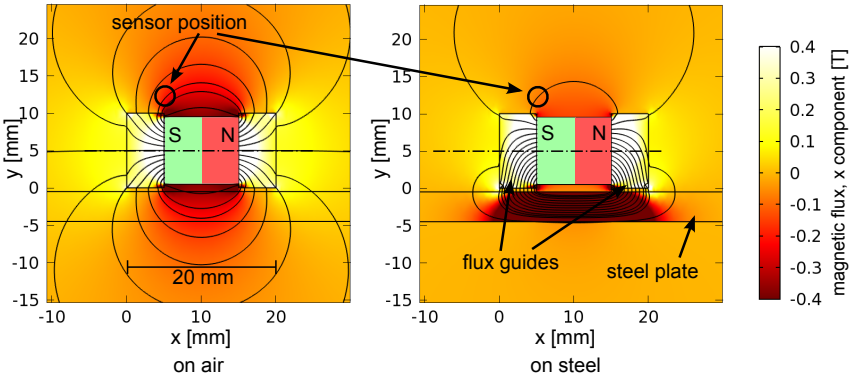

Figure 2.13: 2D simulation of the magnetic flux in the y direction around a magnetic wheel in air and on a steel plate. A possible sensor position is shown, on the opposite side of the adhesion surface.

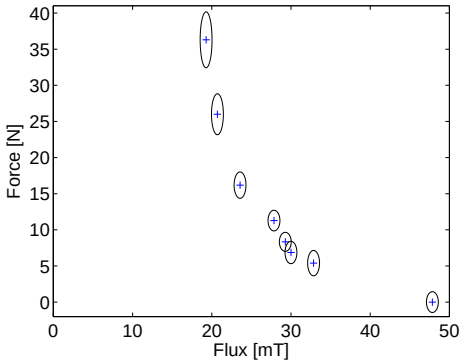

Figure 2.14: Magnetic wheel Hall sensor measures. Adhesion force depending on the flux on a steel plate of 5 mm thick for varying air gaps.

[3]This magnetic wheel was designed by Frédéric Rochat in his PhD [RSM+10].

2.2.4 Conclusions

Magnetic flux monitoring allows to measure indirectly the adhesion force of a magnetic system using a Hall sensor only. It requires to find an optimal placement for the sensor around the magnetic system, and to calibrate the flux-force curve depending on the working conditions. Knowing the current adhesion force is very useful to control the robot safely, as it allows, for instance, to stop the robot before it falls when the force is becoming too low.

Integrating the sensor on the system can be difficult and lead to compromises. In certain cases it is not possible to place the sensor at the optimal magnetic position as there is simply no mechanical space for it. It is usually possible to place it further away from the magnetic system, which reduce the sensitivity of the system, as the signal variations will be lower.

The tested sensor saturates when placed too close to the magnetic systems. Indeed, the sensor's range is of ± 100 mT, and the magnetic flux close to the magnetic systems reaches easily ± 500 mT. Having smaller magnetic sensors able to measure higher magnetic flux would increase the placement possibilities. This could increase the measurable informations, as we could place many sensors directly in the air gap between the magnetic system and the adhesion surface for example, and have a more precise knowledge of the adhesion state of the system. However such sensors were not found on the market and would need to be designed specifically for this application.

2.3 Robots using caterpillar mobility

After this section showing the possibilities of adhesion sensors on different magnetic systems, we will now see different examples of climbing robots with high mobilities, starting with caterpillar robots.

Caterpillars have many advantages over other locomotion systems. They can adapt to irregularities and pass over holes. Their large contact surface gives them better friction and driving force compared to other systems, as it is more likely that at least one part of the caterpillar will get a good grip.

However, caterpillars also have disadvantages. Their rolling efficiency is lower than that of wheels, because of the friction on the rolling axes induced by the caterpillar's tension, and because of internal friction when the caterpillar bends. Turning also induces a lot of friction and slippage. The necessary slippage required for turning makes odometry difficult to achieve, as slippage is not constant and can vary on different surfaces.

Climbing on ferromagnetic structures requires magnetic adhesion. The magnetic adhesion can be embedded in the caterpillars or on the robot frame. The next sections describe two miniature caterpillar robots we designed to assess the potential performances of this type of locomotion. The first one uses magnetic caterpillars. The second one uses normal caterpillars, and embeds more advanced electronics.

2.3.1 Tripillar I

Embedding magnets on the robot is needed to create an adhesion force allowing to climb on ferromagnetic structures. We can embed magnets directly in the caterpillars, which has some advantages. As the force is distributed between many magnets over the length of the caterpillars, it is more robust, as the robot will not fall if one magnet fails to hold,

which can happen if the robot rolls over a screw head for example. The friction force is also increased when magnets are embedded in the caterpillar, as we will see later.

We could not find any record of caterpillar climbing robots able to pass obstacles such as inner corners for example. We designed a magnetic caterpillar robot to take advantage of caterpillars interesting characteristics, with the goal of passing inner angles to increase the mobility of such robots[4].

2.3.1.1 Magnetic caterpillars

The core of the system being in this case the magnetic caterpillars, we started by designing this sensible part first[5]. The technical feasibility of this part has generated constraints on the global robot design.

The design is based on the double-sided T5 belt standard. These timing belts have a 5 mm pitch between their teeth, a thickness of 3.3 mm, standard width between 6 to 25 mm and lengths up to several meters. The teeth of one side are used for transmission, and the teeth of the other side embed the magnets.

The caterpillars are manufactured by molding rubber over steel cables and magnets in a mold (Figure 2.15). The final caterpillars are 6 mm width, 170 mm long and 3 mm thick. The molded NdFeB magnets are 1x1.5x5 mm in size with a N52 grade. The air gap is of 0.1 mm, which gives an adhesion force of 1 N for each magnet.

The first experiments with the caterpillars showed that the magnetic caterpillars were not strong enough to hold a robot for angles bigger than 85°. This is due to the peeling effect: if the caterpillar is pulled perpendicularly to the surface from one side, it can be easily detached (Figure 2.16). We use this principle to remove tape for example. Thus, magnets need to be added on the robot to prevent this peeling: they are fixed on the frame near the caterpillar ends, to increase the force needed to detach the caterpillars. The magnetic caterpillars are still useful, as we will see later with the friction force.

2.3.1.2 Mechanical design

A triangular shape is chosen for the caterpillars, so that the front top point can help detaching the robot from the first plane when making an inner corner transition. Using

Figure 2.15: Caterpillar embedding magnets. It has a length of 170 mm, a width of 6 mm and thickness of 3 mm.

[4]The Tripillar I was developed by Olivier Truong-Dat Nguyen in a semester project under the supervision of Frédéric Rochat and myself [NRS+08].

[5]The magnetic caterpillars were developed by Alain Bock in a semester project under the supervision of Frédéric Rochat and myself [BRS+08].

this triangular shape, passing an inner angle can be decomposed in 6 phases, as shown in Figure 2.17. Phase 2 and 3 are critical for the forces point of view, as magnets must detach from a surface in each of these phases. The triangular shape is optimized to reduce the required forces during an inner corner transition. The computations are shown here.

Phase 2

Figure 2.18 shows the state of the robot in phase 2 with the static forces. We start by computing the force F_C applied on the caterpillar required to detach the wheel B. The condition for the wheel B to detach is expressed by the following mathematical expressions: $R_B = F_B = 0$. There are four different magnetic forces acting in points A, B, C and D. The first three forces are exerted from frame magnets, the fourth is the compound of the magnets of the caterpillars counted, as if the caterpillars were a rigid body. We thus neglect the peeling effect, which would make detachment easier. The static equilibrium equations give:

$$\sum F_x \quad : \quad F_C + G\sin\alpha + M_A - R_A = 0 \tag{2.3}$$

$$\sum F_y \quad : \quad R_C - M_C - M_D - \cos(\alpha)G - M_B + F_A = 0 \tag{2.4}$$

$$\sum T_C \quad : \quad F_C r - M_D\frac{a}{2} - \cos(\alpha)G\frac{a+b}{2} - \sin(\alpha)G\frac{h}{2} - M_B a + F_A(a+b+r) + (R_A - M_A)h = 0 \tag{2.5}$$

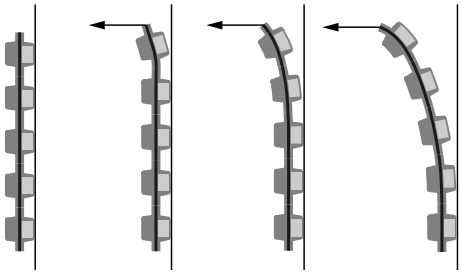

Figure 2.16: Peeling of the magnetic caterpillars. The force to pull one magnet is enough to detach the whole caterpillar.

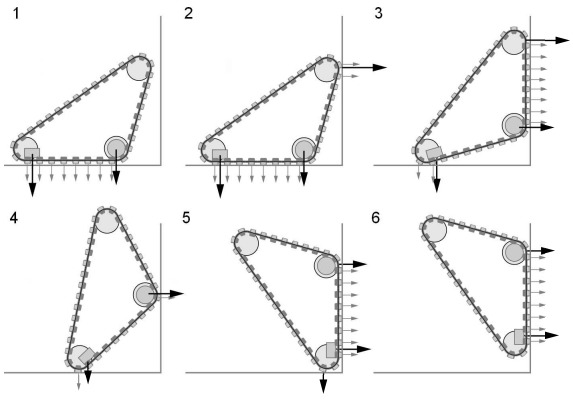

Figure 2.17: Inner corner transition phases, the arrows represent the magnetic forces.

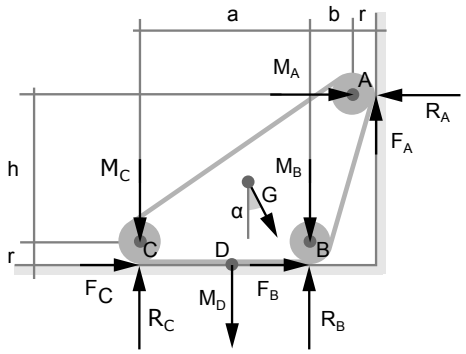

Figure 2.18: Static forces representation for inner corner transition in phase 2.

with the following friction relations:

$$F_A \leq \mu_A R_A \tag{2.6}$$
$$F_C \leq \mu_C R_C \tag{2.7}$$
$$\frac{F_A}{F_C} = f \tag{2.8}$$

where R_x are reaction forces, M_x magnetic forces, F_x friction forces, G the gravity force acting on the robot and f a chosen coefficient. The necessary force F_C to pass phase 2 of the corner transition is computed from this group of equations:

$$F_C = \frac{M_D \frac{a}{2} + M_B a + \cos(\alpha) G \frac{a+b}{2} - \sin(\alpha) G \frac{h}{2}}{r + h + f(a + b + r)} \tag{2.9}$$

R_A and F_A are extracted, and the minimum friction coefficient μ_{Amin} required to pass this phase is:

$$\mu_{Amin} = \frac{F_A}{R_A} = \frac{f F_C}{F_C + M_A} \tag{2.10}$$

Now we will present the situation for three different conditions. The first condition corresponds to the case where the wheel A is not driven and has no magnetic force. In the second condition, the wheel A is driven by the caterpillar but with no magnetic force. Finally, in the third condition, the wheel A is driven and has a magnetic force. The goal is to lower the motor torque and facilitate plane transition.

Condition 1: $F_A = 0$; $M_A = 0$

We analyze the first case when $F_A = 0$. This means that no torque is applied on the wheel A, hence it behaves like a free wheel, not driven by the caterpillar. If we compute F_C using the following numerical values: $M_B = 5$ N, $M_C = 5$ N, $M_D = 5$ N, $a = 32$ mm, $r = 7.5$ mm, $G = 0.215 \cdot 9.81$ N, $\alpha = 0°$, we get the curve showed in Figure 2.19 when varying parameters h and b, which are the position of the wheel A as shown in Figure 2.18.

The circle in Figure 2.19 is representing the actual final size (h_0 and b_0) of the Tripillar I for comparison convenience. We can clearly verify that while increasing h, the minimal force to pass the first phase of plane transition decreases. This force can be converted to a torque on the axis of the wheel C. Its value ranges between 50 and 130 mNm, which is high for a robot of the aimed size. Thus, we are looking for ways to reduce this torque.

Condition 2: $F_A > 0;\ M_A = 0$

If the wheel is driven in A by the caterpillar, a force F_A is acting to lift the robot. With the magnetic force in A still null: $M_A = 0$, we get $\mu = f$. Therefore, if we take a realistic friction coefficient of 0.5 while keeping the other values as in the section above, we get a much lower value of F_C for h_0 and b_0 (Figure 2.20). With the three driven wheels, the required force is almost half of what was necessary with only two driven wheels.

Condition 3: $F_A > 0;\ M_A > 0$

If we add a magnetic force on wheel A, μ cannot be simplified as for the second condition. Thus, we need to choose the force coefficient f, compute the force F_C and the needed friction coefficient μ. We can observe that with $f = 1$, the needed μ stays below 0.5 (Figure 2.21). This means that with the same force applied on wheel A and C, there is no slipping, as the needed friction coefficient μ is low. The minimal force F_C is once again reduced (Figure 2.20, condition 3). As we have at least twice the magnetic force acting on the bottom, we assume the friction coefficient in point C is not a problem.

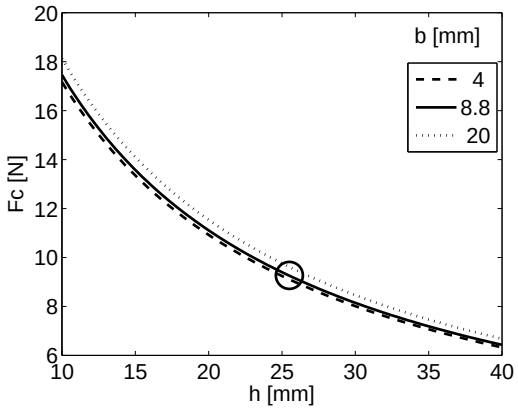

Figure 2.19: F_C for $F_A = 0$ with varying parameter h, the height of the front wheel A for three values of b, the horizontal distance between A and B. The circle represents the prototype robot dimensions (h_0 and b_0).

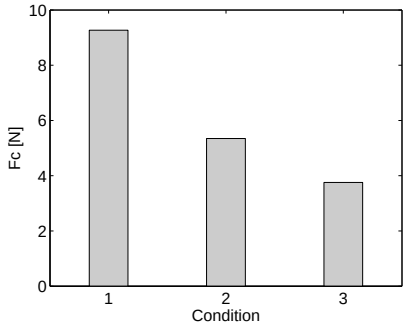

Figure 2.20: F_{C0} for h_0 and b_0 for the 3 different conditions 1) $F_A = 0;\ M_A = 0$, 2) $F_A > 0;\ M_A = 0$, 3) $F_A > 0;\ M_A > 0$.

Phase 3

We continue with the configuration found in condition 3, i.e. with a magnetic force in A. Once the wheel B has been detached and the robot has advanced to the state represented in Figure 2.22, the robot still needs to detach the wheel A to finish the plane transition. We assume here that the wheel B is distant enough from the first plane to neglect a possible vertical magnetic force.

Calculations for phase 3 are similar to the previous one, and we obtain a new equation for the force needed to pass:

$$F_{C2} = \frac{\cos(\alpha)Ga_2 + 2h_2M_A + h_2M_E + \sin(\alpha)G(-b_2 + h_2)}{2(b_2 + a_2 f + r)} \tag{2.11}$$

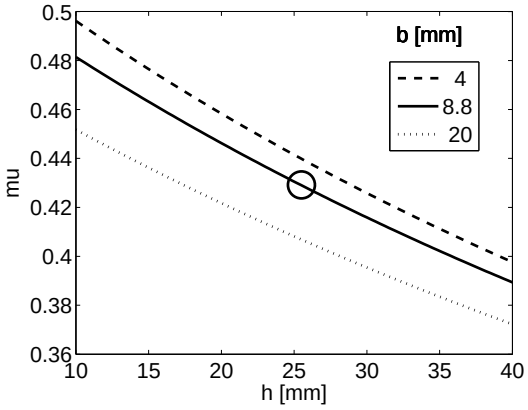

Figure 2.21: Minimum μ_A required for no slipping with $f = 1$, $M_A = 5$ N, for a varying h, with 3 different values of b.

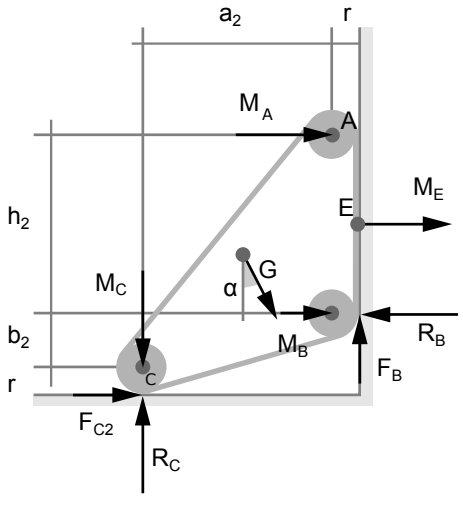

Figure 2.22: Static forces for inner corner transition phase 3.

with the geometrical distance relations:

$$H_2 = \sqrt{b^2 + h^2} \tag{2.12}$$

$$a_2 = \frac{ah}{H_2} \tag{2.13}$$

$$b_2 = \frac{ab}{H_2} \tag{2.14}$$

Figure 2.23 shows the resulting forces of phase 2 (ascending) and 3 (descending) for varying h and b.

Phase 5

To fulfill the corner transition, the phase 5 consists in detaching the wheel C, which requires $F_C > M_C$ in the worst case, which is around M_C (5 N).

Optimization

Based on those results, an optimal size for h and b can be calculated to get the minimal torque out of the motors according to phase 2 and 3. For a chosen b, the optimal h is laying at the intersection of the corresponding ascending and descending curves in Figure 2.23. In our case, for a chosen b of 8.8 mm, the optimal h is just above 20 mm (Figure 2.23, square). Nevertheless, the final chosen shape depended equally on the manufactured caterpillar length, component sizes and integration (Figure 2.23, circle).

The Figure 2.24 shows a picture of the final robot. The different elements composing the robots are details in Figure 2.25. The tension of the caterpillars can be adjusted independently. A screw pushing on the "tensioning bar" shown on the figure allows to change the bar angle and thus the caterpillar tension.

2.3.1.3 Electronics

To control the Tripillar I, we need an electronic able to drive two motors, use some distance sensors and receive commands from the user. The electronic schematics of the Tripillar I is shown in Figure 2.26. A dsPic33 from Microchip is the center of the system. It drives the two motors through H-bridges, manages two front IR distance sensors and receives commands over the Bluetooth module.

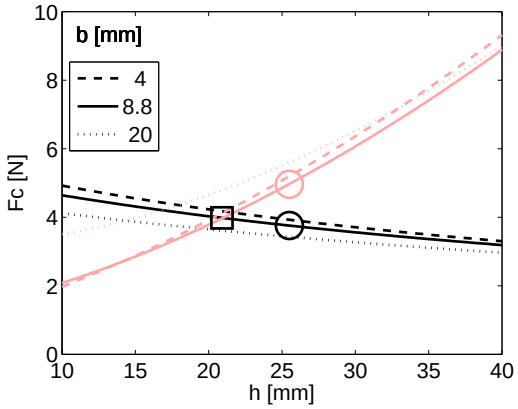

Figure 2.23: F_C for the phase 3, the ascending curves, and phase 2, the descending curves, for varying h and b.

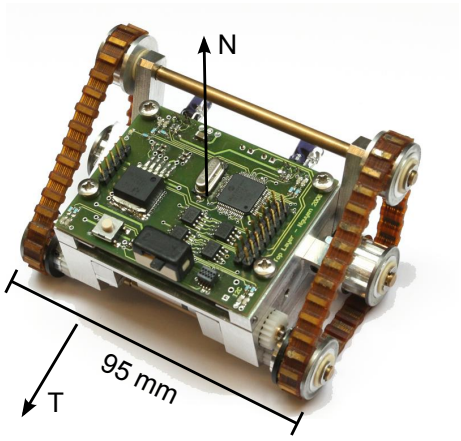

Figure 2.24: The Tripillar I, with the adhesion force N and friction force T.

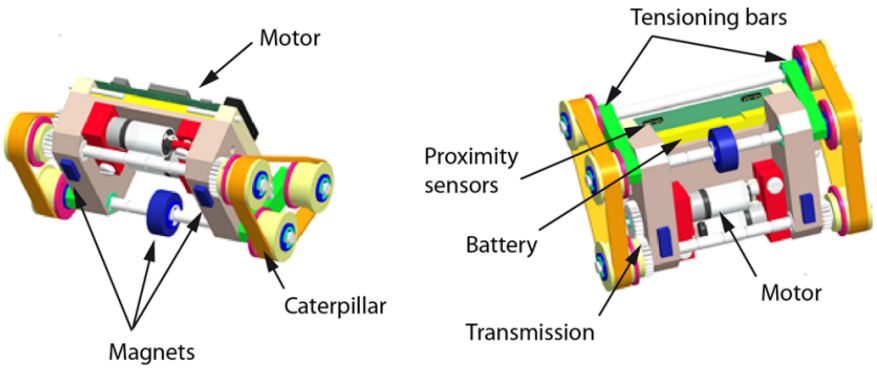

Figure 2.25: Tripillar I components.

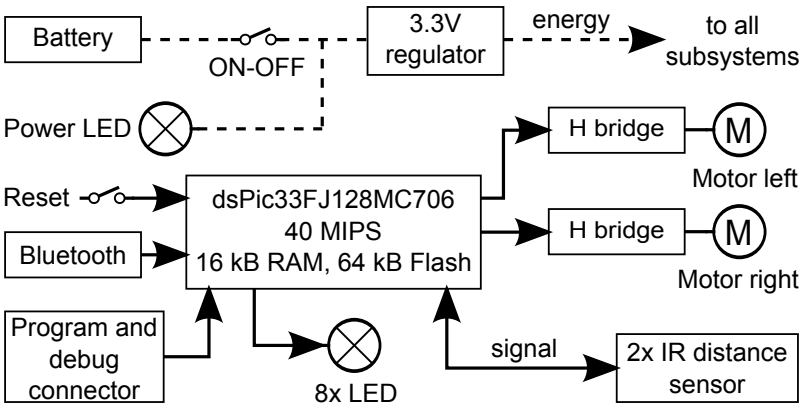

Figure 2.26: Tripillar I electronics.

The motors are open loop controlled. As both motors are identical and as the mechanics is symmetric, the possible speed differences between the two sides are not a problem. The IR distance sensors allow measurements up to 4 cm in front of the robot, which is sufficient to detect obstacles. A 3.7 V Li-ion battery of 800 mAh is used, and gives more than 1 hour of autonomy.

Details about the electronics, which is composed of different standard modules, can be found in Appendix A.1.

2.3.1.4 Control

The control of the robot is done by a user interface on a computer. The control commands are transmitted to the robot over Bluetooth. The speed can be increased or decreased, as well as the rotation speed. The user interface displays the IR sensors measures.

2.3.1.5 Results

The Tripillar I using magnetic caterpillars achieves the expected results in terms of mobility. The robot can move on ferromagnetic surfaces of any inclinations. It can pass inner angles of 90° in any inclination with one exception (Figure 2.27): passing from ceiling to wall must be done backward, otherwise the robot falls. In this case, the triangular shape is not required to detach the back wheel, as the gravity is helping.

The magnetic caterpillar has very interesting frictions results. The friction coefficient μ_f is linked to the friction force T and the normal force N by the formula (Figure 2.24):

$$T \leq \mu_f N \tag{2.15}$$

We measured the normal force and the friction force on a non-magnetic surface and on a ferromagnetic surface, for different tensions of the caterpillars (Figure 2.28(a)). The friction force does not depend on the caterpillar tension. However, it is more than 8 times bigger on ferromagnetic surfaces than on non-ferromagnetic ones due to the adhesion force.

The normal force depends on the caterpillar tension, because of the peeling effect. The force increases when the tension in the caterpillar is increased, because more magnets are pulled on at the same time when the caterpillars becomes almost rigid. Due to these behaviors, the friction coefficient can rise above 1, up to 2.8 with a low caterpillar tension (Figure 2.28(b)).

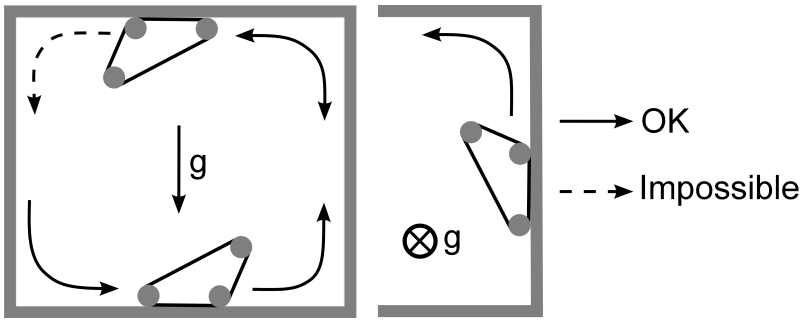

Figure 2.27: Tripillar I mobility results.

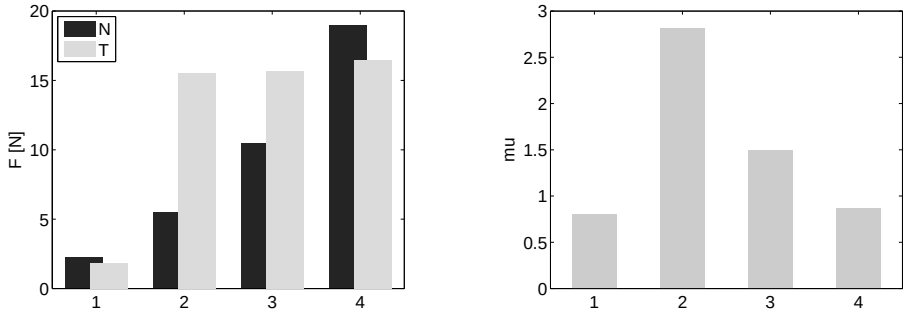

(a) Force N to lift the robot and the tangential force T to drag the robot.

(b) Resulting friction coefficients $\mu = T/N$.

Figure 2.28: Forces and friction coefficient of the magnetic caterpillars on non-magnetic stainless steel (1), on ferromagnetic smooth iron with low caterpillar tension (2), medium tension (3) and high tension (4).

2.3.1.6 Conclusions

With its magnetic caterpillars and magnets fixed on the frame, the Tripillar I can move on ferromagnetic surfaces of any inclination, and pass inner angles of 90°. These performances are achieved using only two degrees of freedom and an easy remote control.

The magnetic caterpillars of the Tripillar I have a strong friction coefficient, up to 2.8, which is very interesting for applications where the surface may be slippery. This case can arise when performing ultrasonic inspection, as a liquid couplant is required between the sensor and the surface to transmit the ultrasonic energy. The liquid leaks on the surface which becomes slippery.

The caterpillars also transmit the motor torque to all wheels. This integration allows to reduce the size of the robot.

The high friction force over the full length of the caterpillar is not necessary for passing inner corners, as the caterpillars do not touch the surface during the transition. For robots aiming to pass such obstacles, the embedded magnets in the caterpillars are thus not required.

As expected, the Tripillar I cannot pass outer angles. Linking two similar robots with an articulated arm could be a solution to pass these angles. But it would add one or more degrees of freedom, and make the control of the robot more complex.

2.3.2 Tripillar II

Based on the good results of the Tripillar I, a new version of the robot is designed[6]. The goal is to embed more sensors and electronics, allowing the robot to move autonomously, for instance by following a line. Distance sensors are embedded to detect a wall and a line on the floor. A Hall sensor in embedded to measure the adhesion quality. It allows to stop the robot if the force becomes too low.

The mechanics is also improved. The caterpillars are completely encircling the robot (Figure 2.29). This makes it more robust, as the caterpillars protect the electronics, which

[6]The mechanics of the Tripillar II was designed by Ludovic Daler in a semester project under the supervision of Frédéric Rochat and myself [DRSM10].

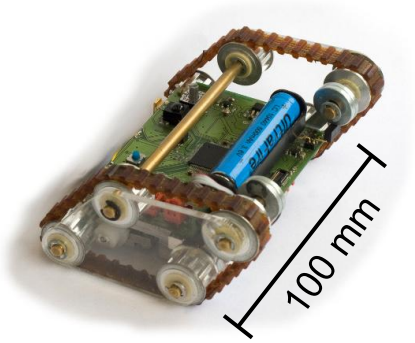

Figure 2.29: Tripillar II.

was exposed to falls on the first version. The robot can also fall on its back, in which case it will not be blocked as it will be able to turn over by rolling against a wall: the robot will start moving as a normal inner corner transition, but as there is no magnet on the top central axis, it will fall back on its correct side and will be able to continue moving.

Because the magnetic caterpillars do not improve angle passing, as they are not in contact with any surfaces during the transition, non-magnetic caterpillars are used. The caterpillars are still molded in rubber, to get a good friction coefficient. The adhesion force is coming only from fixed magnets placed on the frame. Compared to the Tripillar I, magnets are added on the top front axis, to allow passing from ceiling to wall in the forward direction, which was not possible on the first version.

2.3.2.1 Magnetic flux monitoring

Hall sensors can be used to monitor the adhesion force, as shown in section 2.2. For the Tripillar II, a Hall sensor is placed on the side of one of the front magnets. The configuration is similar as the one shown in Figure 2.9. As the distance between the magnet and the surface is not changing when moving on a flat surface, the force can be determined from the flux. Results are presented in Section 2.3.2.4.

2.3.2.2 Electronics

Figure 2.30 shows the electronic schematics of the Tripillar II. It is highly improved compared to the first version of the robot, with many additional sensors.

A dsPic33 is the core of the system. The motors have now a full control electronic module, with current sensing and encoders (see Appendix A.1.3 for details). In addition to the two front distance IR sensors, three IR sensors are looking at the bottom of the robot for line following. A 3D accelerometer gives information about the orientation of the robot. Two Hall sensors measure the flux intensity around the magnets, to detect the ferromagnetic quality of the surface. An IR receiver is added to the Bluetooth, to simplify the manual control of the robot. A 3.6 V Li-ion battery of 500 mAh is used, and gives more than 45 minutes of autonomy. A second battery can be added easily, but the electronics to put them in parallel has to be added on a different PCB (see Appendix A.1.4). The voltage of the battery can be measured by the microcontroller through a voltage divider. If the voltage becomes too low, it can turn off the motors and sensors to prevent a low voltage on the battery.

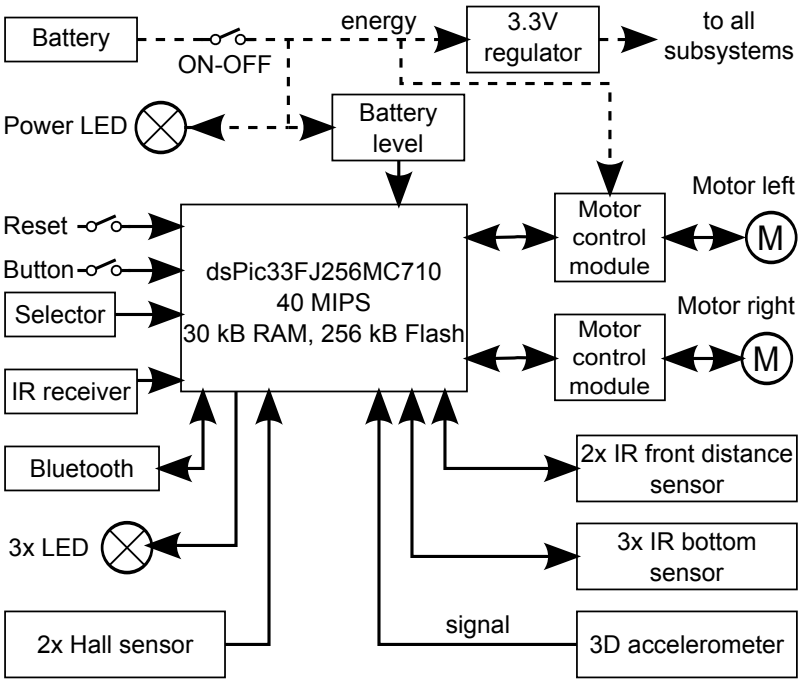

Figure 2.30: Tripillar II electronics.

The microcontroller is programmed using the Aseba framework[7] (see Appendix A.2.2 for details).

2.3.2.3 Control

There are two main control methods of the robot: manual and autonomous.

The manual control can be done through infrared, using a remote control, or through Bluetooth, using a computer. Both ways offer the same control commands: the user can increase or decrease the forward speed, increase or decrease the rotation speed and stop the robot. The Bluetooth connection allows to see the measures of the IR sensors, Hall sensors and accelerometer on a user interface.

The autonomous control offer three main features: line following, inner angle passing and ferromagnetic surface monitoring. These features are managed by the state machine shown in Figure 2.31. The line following is achieved by using the three IR bottom sensors. Different motion command are given to the motors depending on the measures of the sensors. The inner angle passing is done in two stages: first the robot aligns perpendicularly to the new surface using its IR front sensors. Then the robot moves forward a predefined distance to pass the angle. The Hall sensors continuously measure the field around the magnet. When this field becomes too low, the force is becoming too low to hold the robot and it stops to prevent falling. The accelerometer is used to limit the speed when the robot is not on the bottom surface, to lower the risks of falling.

[7]The low-level was mainly programmed by Philippe Rétornaz.

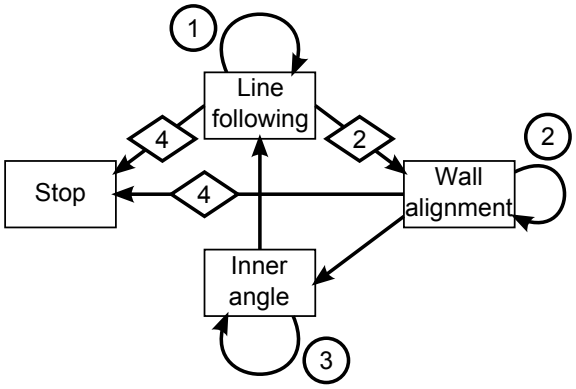

Figure 2.31: Autonomous line following state machine and sensors: (1) IR bottom sensors, (2) IR front sensors, (3) encoders, (4) Hall sensors.

2.3.2.4 Results

The Tripillar II has a slightly improved mobility compared to the first version of the robot. It can move on surfaces of any inclinations, pass inner angles in any orientation, but cannot pass outer angles. The improvement is the ability to pass the inner angle from ceiling to wall in forward motion.

Due to the encircling caterpillars, the Tripillar II can recover after falling on its back by rolling against a wall: it will rotate in the corner until it is up again.

The robot has an adhesion force of 17.8 N, and a friction force of 16 N. This gives a friction coefficient of 0.9.

The adhesion sensor is not working as expected. Due to mechanical constraints, the Hall sensor is not placed at an ideal location. The signal variations are thus smaller than expected, and the force can thus not be monitored precisely. However, it is sufficient to detect if the robot is on a ferromagnetic surface or not, using a simple threshold on the sensor value. The robot can thus stop automatically when reaching the end of a ferromagnetic plate.

Using its IR sensors, the Tripillar II can follow a line, align against walls and pass inner angles. A test route was done on a folded steel plate, where the robot follows a line, passes two inner angles from floor to ceiling, and comes back to the bottom (Figure 2.32). The robot can follow the path without problems. It detects the end of the ferromagnetic plate using its Hall sensor and stops.

An autonomy of 45 minutes is reached using one battery.

2.3.2.5 Conclusions

The Tripillar II shows a good mobility in complex ferromagnetic environments. The robot is able to move on surfaces of any inclinations, and pass inner angles of 90° of any orientation.

The embedded electronics allows the wireless remote control of the robot. The Tripillar II is also able to follow a line, pass inner angles and stop before non-ferromagnetic surfaces autonomously using IR distance sensors and Hall sensors. To our knowledge, it is the smallest caterpillar climbing robot with this ability.

We can compare the adhesion and friction forces of the Tripillar I and II, the first one having magnetic caterpillars, the second one standard ones. First, when the caterpillars

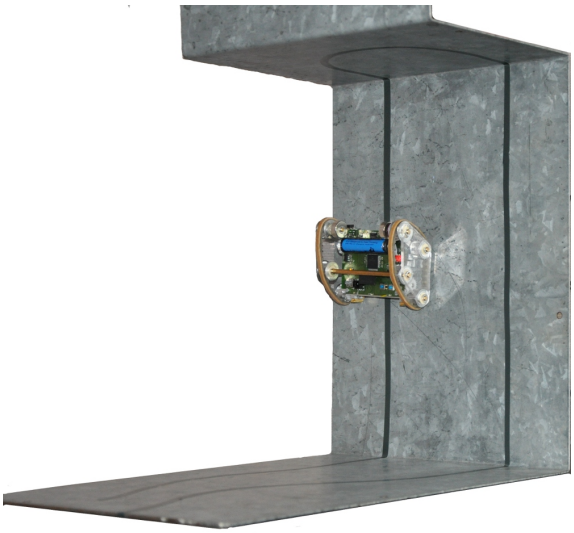

Figure 2.32: The Tripillar II following autonomously a line on a test structure.

of the Tripillar I have a high tension, they behave almost like a rigid plate and there is no peeling effect. In this case, both robots have an almost equal adhesion force. The magnets fixed on the frame of the Tripillar II are stronger, which compensates the non-magnetic caterpillars. As the rubber used for the caterpillars is the same on both robots, the corresponding friction force and friction coefficient are also almost equal. Secondly, when the caterpillars of the Tripillar I have a normal (medium) tension, the adhesion force is 40% lower. However, the friction force stays the same, thanks to the magnetic caterpillars.

The adhesion force of the Tripillar II does not depend on the caterpillars tension, but only on the adhesion force of the magnets fixed on the frame. This is an advantage for inner corner transitions, as the force is kept constant, even though the caterpillars are not touching the surface during the transition. Using magnetic caterpillars on the Tripillar II would increase the friction force on flat surfaces, but not during the plane transitions.

With these mobility properties, the Tripillars are good miniature platforms to carry sensors for the inspection of moderately complex areas. The description and results of the assembly of an Eddy current sensor on the Tripillar II are shown in Chapter 4.

2.4 Robots using advanced magnetic wheel

We saw the development and performances of two climbing robots using caterpillars. They achieve a good mobility, but cannot pass external angles. We will now describe two robots using an advanced magnetic wheel concept.

Standard magnetic wheels (as shown in Figure 1.13, page 8) have some advantages. Thanks to their adhesion force, they allow climbing on ferromagnetic surfaces by rolling. Using wheels also allows a continuous motion, which is easier to control than walking robots, for example.

However, they also have disadvantages. Most wheels are heavy compared to their adhesion force. This is mainly because not all of the magnetic flux is closing in the adhesion surface, but closes in air, as the top half is too far away from the surface. The main

disadvantage of magnetic wheels is that they get blocked in inner corners: when making an inner corner transition, the wheel must be pulled off the first surface, with a force that is usually too strong. There are solutions to this problem, such as the lifters from the MagneBike [TFC+09] that create a mechanical force to detach the wheel from the plane, or special wheel arrangements similar to those on the Tripillars [FCSM09].

Another solution to this problem was developed. The concept is to have a magnetic system able to rotate inside the wheels[8]. Two similar robots have been developed using this concept. The first robot is very small and validates the concept. The second robot is bigger and embeds more advanced electronics and sensors. Both are described in the next sections.

2.4.1 Cy-mag^{3D} I

The Cy-mag^{3D} I uses the principle of having a magnetic system rotating inside a wheel[9] (Figure 2.33). The torque of the motor is applied between the magnetic system and the wheel. When there is no obstacle, the torque created by the magnetic system holds it in position, the wheel rotates around the magnetic system and the robot moves forward. When the wheel is blocked in an inner corner, the magnetic system rotates, which switches the force from the first to the second plane. The wheel can then move on the new plane.

In the case of the Cy-mag^{3D} I, the magnetic system is placed on the central structure of the robot, and a wheel rotating around the robot is placed on each side (Figure 2.34).

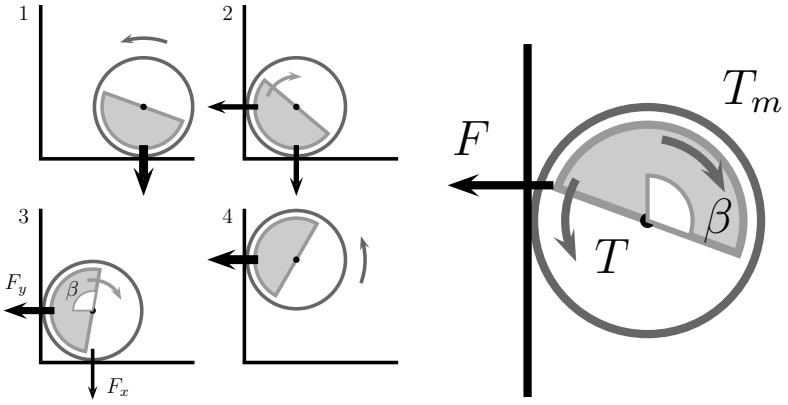

Figure 2.33: (a): Transition phases of an inner straight angle regardless of the gravity. When the wheels cannot rotate forward due to an obstacle, the magnetic system rotates backwards and thus transfer the adhesion force to the new surface. When the transfer is finished, the holding force is sufficient to move on the new surface. (b): Magnetic force F, magnetic holding torque T and motor torque T_m between the magnetic system and the wheel.

[8]This idea was developed by Frédéric Rochat in his PhD [Roc11].

[9]The magnetic system and mechanics of the Cy-mag^{3D} I was developed by Barthélémy Lüthi in a semester project under the supervision of Frédéric Rochat and myself [LRSM09].

2.4.1.1 Magnetic system design

The magnetic system must fulfill two requirements. It must have a sufficient force to hold the robot in any orientation. In the case where the robot has to hold on the ceiling, the force must be greater than the robot weight. The magnetic system must also have a sufficient holding torque, allowing it to go up on a wall. If this torque is too low, the magnetic system will roll back and the robot will fall.

Analytical computations

Analytical computations are done to have a first estimation of the required magnetic system. We consider a cylindrical magnet, with steel flux guides on the sides (Figure 2.35). The worst case arises during flips from one side of a plate to the other side. A 2 mm thick steel sheet is used to design the magnetic system to hold in this situation.

The permeance of the flux guides is considered as infinite. The external permeance Λ_e (Equ. 2.17) is the sum of the air gap permeance Λ_δ, the surface permerance Λ_s, and the leakage permeance Λ_σ (Equ. 2.16). For the following, l_α will represent the corresponding length of each part α, and S_α will represent its cross section.

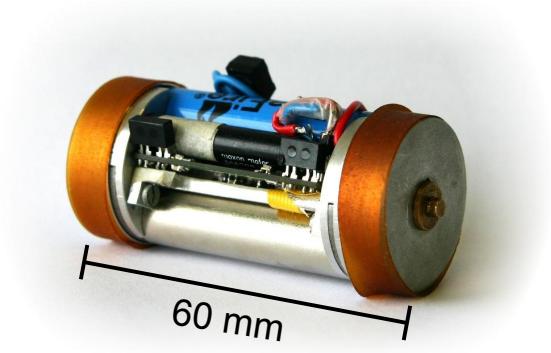

Figure 2.34: The Cy-mag^{3D} I.

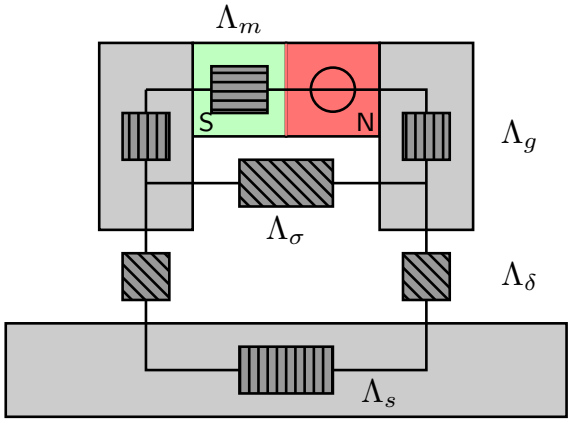

Figure 2.35: Magnetic model of the system. The stripped boxes show the permeances Λ of all different sub-parts (m: magnet, g: flux guide, s: surface, δ: air gap, σ: leakage).

$$\Lambda_\delta = \frac{\mu_0 S_\delta}{2\delta}, \Lambda_\sigma = \frac{\mu_0 S_\sigma}{l_\sigma}, \Lambda_s = \frac{\mu_0 S_s}{l_s} \tag{2.16}$$

$$\Lambda_{\delta+s} = \frac{1}{\frac{1}{\Lambda_\delta} + \frac{1}{\Lambda_\delta}}, \Lambda_e = \Lambda_{\delta+s} + \Lambda_\sigma \tag{2.17}$$

The load line slope K of the magnet is then computed:

$$K = \Lambda_e \frac{l_m}{S_m} \tag{2.18}$$

The final induction in the magnet B_m is the intersection of the magnet B-H curve with the load line:

$$B_m = B_r + \mu_m \mu_0 H_m = -K H_m \tag{2.19}$$

$$B_m = \frac{B_r}{1 + \frac{\mu_m \mu_0}{K}} \tag{2.20}$$

B_r being the residual induction of the magnet, μ_m its relative permeability, and H_m the coercitive force. The flux is dividing in two parts and pass through $\Lambda_{\delta+s}$ and Λ_σ. The induction in the air gap can thus be computed:

$$B_\delta = B_m \frac{S_m}{S_\delta} \frac{\Lambda_{\delta+s}}{\Lambda_{\delta+s} + \Lambda_\sigma} \tag{2.21}$$

Finally, the attracting force F is:

$$F = \frac{B_\delta^2 S_\delta}{2\mu_0} \tag{2.22}$$

We expect the robot to weigh around 100 g. Using these equations, the following values are expected to create an adhesion force of 720 g, which makes a good safety margin: $B_r = 1.27$ T, $\mu_m = 1.05$, $\delta = 1$ mm, $S_\delta = 6 \times 2$ mm^2, $l_m = 40$ mm, $S_m = \pi \times 4.9^2$ mm^2, $S_\sigma = 300$ mm^2, $l_\sigma = 40$ mm, $S_s = 100$ mm^2 and $l_s = 40$ mm give an adhesion force F of 7.2 N.

Magnetic simulations

As the theoretical computation requires a lot of hypotheses, and as some values like the leakage surface is difficult to estimate, 3D simulations of the magnetic system are done using the software *Comsol* to get a more precise force estimate[10]. Forces and torques acting on the system in different conditions can be computed.

Figure 2.36(a) shows the force and torque applied to the magnetic system rotating around its axis on a vertical plate (as in Figure 2.33(b)). The maximum force is around 12 N, which is 50% higher than expected. An important point here is the maximum torque: it must be big enough to maintain the robot when going up. For a 100 g robot, with wheels of 14 mm radius, the required torque is of $T = 0.1 \times 14 = 14$ mNm. The maximum computed torque is of 22 mNm, which is enough.

Figure 2.36(b) shows the force evolution on the first and second plate during an inner corner transition. The total force decreases a bit, but stays strong enough to hold the robot. A very interesting point is that the torque stays very low at only 0.13 mNm. It requires thus almost no force to rotate the system in the corner. These values show that this system has no problems passing inner angles, and that it does not stay blocked in the corner as standard wheels do.

[10]The Cy-mag^{3D} I simulations were done by Frédéric Rochat in his PhD [Roc11].

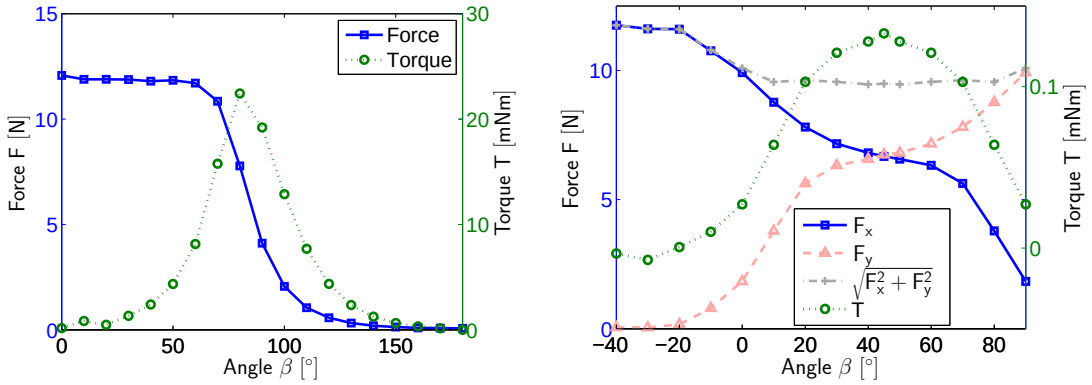

(a) (b)

Figure 2.36: (a) Simulation of the magnetic force and torque of the magnetic system rotating around its axis above a plate (as shown in Figure 2.33(b)) and (b) Simulation of the magnetic forces F_x and F_y and torque T on each surfaces during an inner corner transition (as shown in Figure 2.33(a)).

2.4.1.2 Mechanical design

Figure 2.37 shows the mechanical design with the different elements of the robot.

The cylindrical magnet has a diameter of 10 mm and a length of 40 mm. It has a longitudinal magnetization of N40. Two steel flux guides are placed on the end of the magnet, inside the wheels. They help redirecting the flux to the bottom of the robot to maximize the adhesion force.

Two Maxon motors of 6 mm diameter are used with gearheads of ratio 1:221. With an efficiency of 50% and an additional reduction of 2:1, the final output torque for each motor is of 72 mNm. It is sufficient compared to the previously computed 14 mNm required to drive the robot up a wall.

The wheels are placed on each end of the robot. They are placed over the magnetic flux guides, to impose a minimal air gap. This prevent the system from sticking to a surface, which would block the robot.

A lithium-ion battery of 500 mAh provides energy to the robot. The wheels must be removed to change the battery. The PCB is placed below the motors.

2.4.1.3 Electronics

The electronics of the Cy-mag^{3D} I (Figure 2.38) is very similar to the one of the Tripillar I. A dsPic33 microcontroller controls two motors in open loop and two IR distance sensors. It receives commands through an IR receiver. A 3.6 V Li-ion battery of 500 mAh is used, and gives more than 30 minutes of autonomy.

The microcontroller is programmed using the Molole library (see Appendix A.2.1 for details).

2.4.1.4 Control

The control of the robot is done by an IR remote control. The speed, as well as the rotation speed, can be increased or decreased.

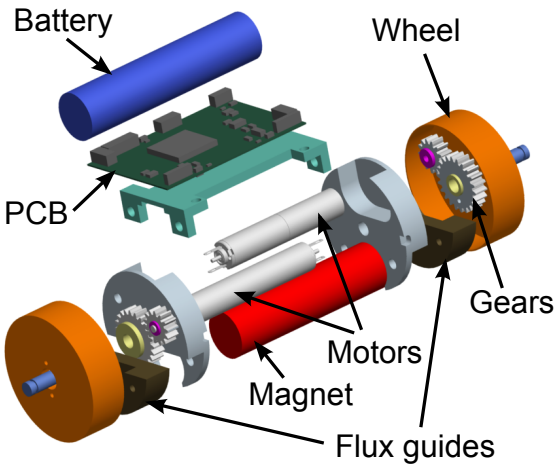

Figure 2.37: Exploded view of the Cy-mag^{3D} I.

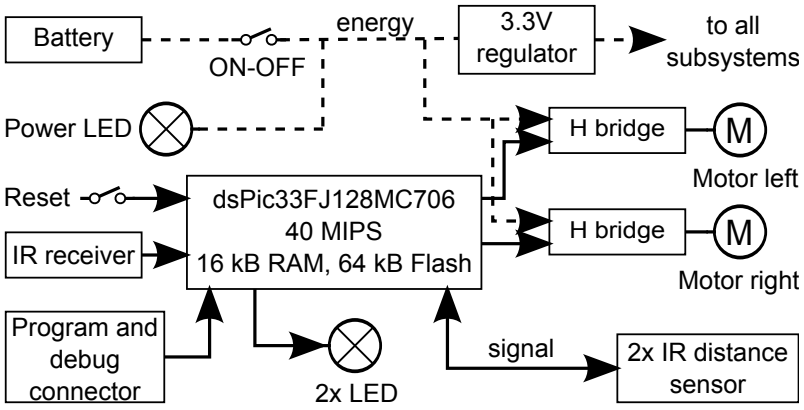

Figure 2.38: Cy-mag^{3D} I electronics.

2.4.1.5 Results

The robots achieve very interesting mobility results (Figure 2.39, 2.40 and 2.41). It is able to move on ferromagnetic surfaces of any orientation. It can pass inner angles (between 30 and 180°) in any orientation.

It can pass outer angles of many types, but with some limitations. On the outer transitions where the robot is going down after the edge, the robot must be driven slowly, because it passes from one equilibrium position of the magnetic system to the other one. It thus makes a fast forward movement which is uncontrolled and might result in detachment of the robot (shown as ⚠^{a} on the figures). Insufficient friction reduces the chances of passing some outer corners depending on the orientation of gravity and their sharpness (shown as ⚠^{b} on the figures). In most cases the robot slips on the edge and start to oscillate back and forth, to finally pass to the new surface. In these cases it is better to pass the angle at maximum speed.

Surfaces flips are also possibles in the orientations where the robot does not go up at the beginning of the transition.

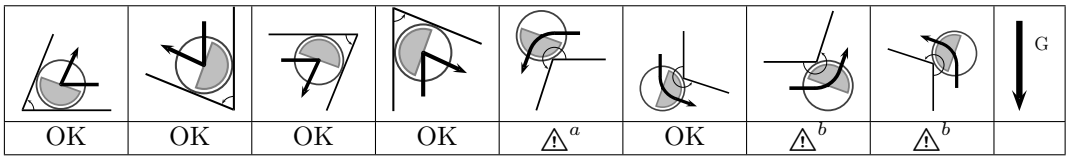

Figure 2.39: Inner and outer angles transitions in different orientations, for angles ranging from 10 to 300°.

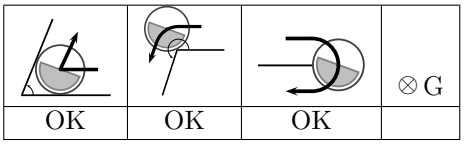

Figure 2.40: Transitions with lateral gravity.

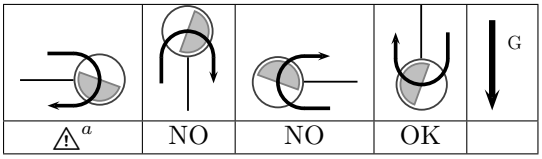

Figure 2.41: Surface flips in different orientations of gravity.

2.4.1.6 Conclusions

The Cy-mag^{3D} I demonstrates the good performances of this new magnetic wheel system. Passing inner angles is easy and requires almost no force, which is an advantage over standard magnetic wheels. Passing outer angles is also possible in most cases, as well as surface flips. This is a strong improvement compared to the Tripillars, that could not pass these last two obstacles.

The robot configuration with one wheel on each side is easy to control with only two degrees of freedom.

Increasing the mobility performances could be achieved by linking two similar robots one after the other with an arm. The robot from the back could thus push the robot slipping in the difficult situation for example. However, the control would be more difficult.

2.4.2 Cy-mag^{3D} II

Based on the good mobility results of the Cy-mag^{3D} I using the new magnetic wheel system, we want to design a similar robot to inspect complex structures. For this, we need to embed in the robot a camera and other sensors allowing the inspection of the environment as well as the remote control of the robot. The robot thus needs to be bigger, providing the available room to integrate more electronics.

The design of the Cy-mag^{3D} I was not just scaled up to design the Cy-mag^{3D} II[11]. To have some modularity and to be able to test other robots configurations, we made an independent wheel module embedding a magnetic system, a motor, a battery and the required electronics. For the Cy-mag^{3D} II configuration, two wheels are connected by a common axis (Figure 2.42), obtaining the same cylindrical shape as the first version of

[11]The Cy-mag^{3D} II was developed by Olivier Marti in a diploma project under the supervision of Frédéric Rochat and myself [MRS+11], and is referred as Cy-mag^{3De} in the published works.

the robot. A central body is placed on this central axis. It embeds all the electronics, including a processor, a camera, a Wifi card and a microcontroller.

The body is driven by a motor and can rotate around the axis. This allows to change the camera view direction. It also allows to push the robot with a tail that can be connected to the body. The tail can help passing difficult obstacles, by pushing or slowing down the robot. It can also help to stabilize the robot movements.

2.4.2.1 Magnetic system design

Figure 2.43 shows the magnetic system with the magnet (1), the holding part (2) and the two flux guides (3). The magnetization of the magnet is along the axis of the wheel.

We designed the shape of the magnet based on 3D simulations[12]. We then ordered magnets to the exact shape we wanted, to meet our sizes requirements.

Measures of the adhesion force done on the final system are validating the simulations results (Figure 2.44). A force of 100 N is achieved with an air gap of 4 mm.

The forces transitions in an inner angle have very similar shapes to the ones obtained for the Cy-mag^{3D} I (shown in Figure 2.36(b)).

2.4.2.2 Mechanical design

Figure 2.45 shows a split view of the wheel mechanics. The main elements are the central axis (2), the bell (1) and the flange (3). The central axis of the wheel is connected to

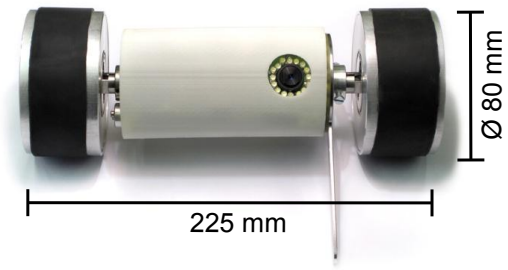

Figure 2.42: The Cy-mag^{3D} II.

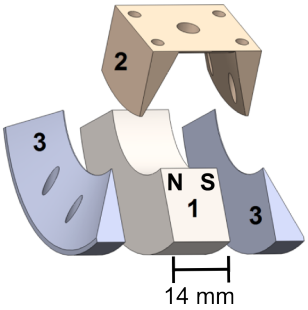

Figure 2.43: View of the magnetic system: (1) magnet, (2) holding part and (3) flux guides.

[12]The Cy-mag^{3D} II magnetic system simulations and design were done by Frédéric Rochat in his PhD [Roc11].

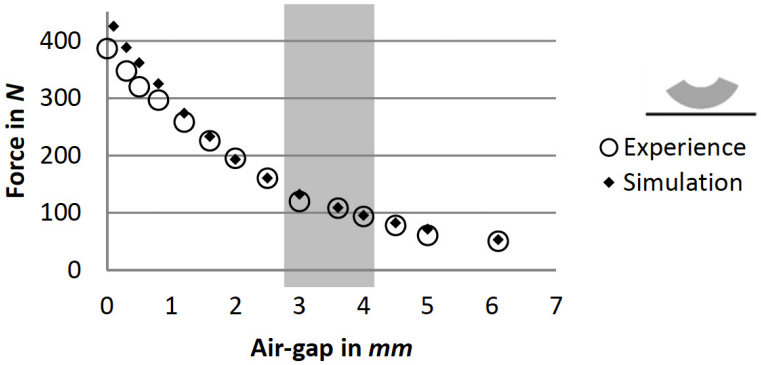

Figure 2.44: Comparison of the simulated and measured adhesion forces of the Cy-mag^{3D} II magnetic system on a steel plate for various air-gaps. The gray area shows the area of interest for the robot.

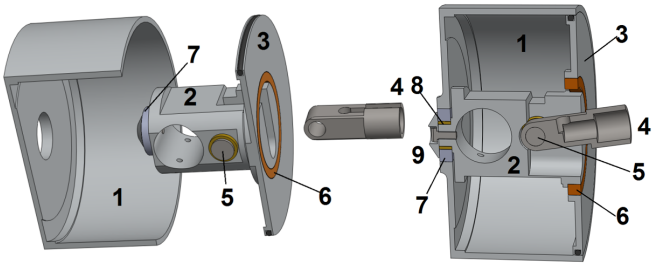

Figure 2.45: Split view of the wheel: (1) bell, (2) axis, (3) flange, (4) output axis, (5) fixation pin, (6) big ball bearing, (7) small ball bearing, (8) bearing, (9) washer.

the rest of the robot. It does not rotate in the Cy-mag^{3D} configuration. The bell and the flange are the only rotating elements of the wheel. They are mounted on the central axis on ball bearings. This design was chosen because the magnetic system inside the wheel must be able to rotate with respect to the outer part of the wheel.

The other elements composing the wheel are shown in Figure 2.46. The main elements are the motor (1), the conical gears (3-4) transmitting the torque from the motor to the outer wheel, and the magnetic system with its magnet (5) and flux guides (6). Figure 2.47 shows a cut view of the wheel. It shows clearly how tight it is, and how difficult it is to include all the needed elements.

The tail construction is shown in Figure 2.48. A magnetic braking system is included in the design. It is done using magnets rubbing on the ferromagnetic tail. This system makes a torque protection to the robot: if the robot falls down on the tail, the high forces will not be transmitted in the motor, but the disks will slip and dissipate the energy.

Figure 2.49 shows the rotation contact. It is composed of a rolled flexible PCB, fixed on the axis on one side, and on the body on the other one. A rotation of one turn is possible.

Figure 2.50 shows the different electronic boards included on the robot central body.

The friction coefficient of the wheel is important for the mobility. If it is too low, the wheel may slip, which could prevent passing an obstacle. The raw aluminium wheels do not succeed to pass some inner angles for example.

There is a trade off between the slimness and the durability of the material. The slimmer

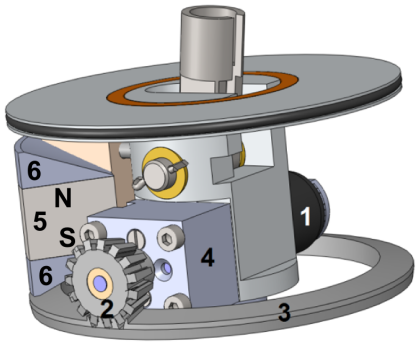

Figure 2.46: View of the wheel (whithout the bell): (1) motor, (2-3) conical gears, (4) motor support, (5) magnet and (6) flux guides.

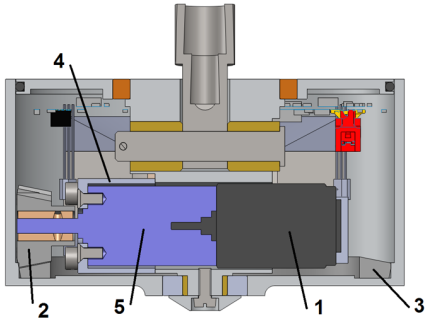

Figure 2.47: Cut view of the wheel: (1) motor, (2-3) conical gears, (4) motor support, (5) motor gears.

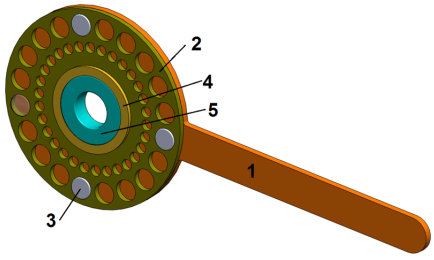

Figure 2.48: View of the tail: (1) tail, (2) bored disc, (3) magnets, (4) holding cylinder, (5) ball bearing.

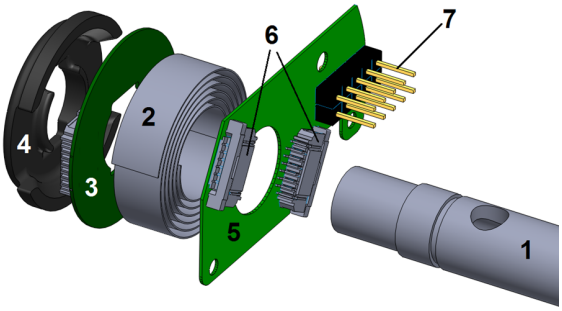

Figure 2.49: Split view of the rotation contact: (1) robot axis, (2) flexprint, (3) axis PCB, (4) guide, (5) body PCB, (6) flexprint connector, (7) body connector.

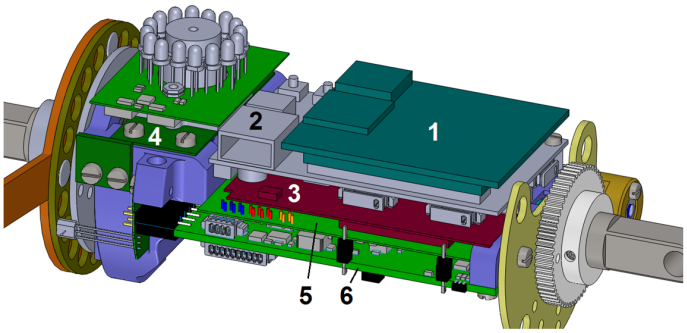

Figure 2.50: Body with its electronics: (1) processor board, (2) mother board, (3) Wifi module, (4) camera and LEDs, (5) translator, (6) function board.

the material, the higher the adhesion force. However, the durability will be lower with slimmer material, and the part will need to be changed often.

Different materials and fixation methods were tested. Finally, inner tubes are used. They offer a good friction coefficient, and are solid enough to keep their properties over time, even under the strong forces involved. The measured friction coefficient is of 0.76. It is almost three times that of the aluminium (0.28).

The inner tubes hold on the wheels by their elasticity. Thus, they can be changed easily. A small groove is machined in the wheel to improve their holding capabilities.

An encoder is used on the wheel motor. However, its measuring system is based on Hall sensors, which are saturated by the proximity of the magnetic system. We added a ferromagnetic "cap" around it to shield it (Figure 2.51). This cap is guiding the flux around the encoder, and the residual field inside is reduced. Using this shielding cap, the encoder can be used without problems on ferromagnetic surfaces. On non-ferromagnetic surfaces, the field is still a bit too high and can cause some problems. The cap could be made thicker to reduce the effect, but the available room does not allow it. A speed controller based on the induced voltage is thus also implemented on the robot in case the encoder is not usable.

The final weight of the robot is of 1700 grams. Each wheel has an adhesion force of 100 N, which makes a safety factor of more than 10.

2.4.2.3 Magnetic flux monitoring

Measuring the adhesion force of a climbing robot can be very useful for the control and the safety of the robot, as already shown in Section 2.2.

On the Cy-mag^{3D} II, based on magnetic simulations and the available space, Hall sensors are placed at both ends of the magnetic system (Figure 2.52(a) and 2.52(b)). They measure the flux intensity on each end of the magnetic system, and give informations about the system position and about the ferromagnetic properties of the surface.

To calibrate the system, the wheel was blocked on a ferromagnetic plate, and the magnetic system rotated one full turn, while measuring the Hall sensors output. Figure 2.53(a) shows the measurements obtained during this procedure. The maximum value of the Hall sensor arises when the end of the magnetic system is the closest to the adhesion surface. The angle difference between the peak of each sensor is of 105°, which corresponds to the angle of the magnetic system.

The same experiment was done with the wheel blocked in a 90° corner. Figure 2.53(b) shows the results. In this case we have two peaks per sensor. The smallest ones correspond to the case when the magnetic system is in the corner. The flux closes in both sides of the corner and is thus lower. The angle between these two peaks will depend on the corner angle and the magnetic system angle (fixed). In this case we have $105 - 90 = 15°$.

Knowing these characteristics, the user or the designed of an automatic control can monitor these sensors, recognize in which situation the robot is, and thus control the

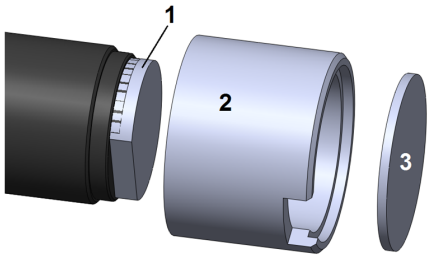

Figure 2.51: Magnetic shielding of the motor encoder (⌀17 mm): (1) the motor encoder, (2-3) the shielding cap parts.

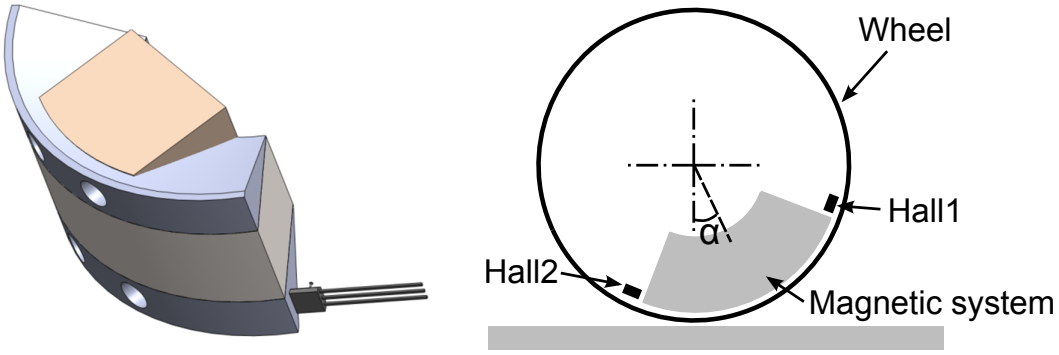

(a) (b)

Figure 2.52: Cy-mag^{3D} II hall sensors locations. The Hall1 sensor is located at the front, the Hall2 sensor at the back.

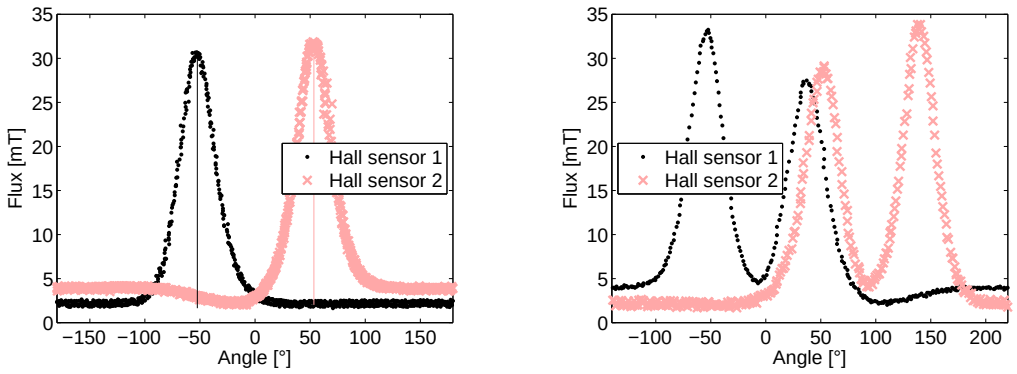

(a) On a flat surface. The angle between the peaks is of 105°, which correspond to the angle of the magnetic system.

(b) In a corner.

Figure 2.53: Cy-mag^{3D} II hall sensors measures. The magnetic system is rotated in the blocked wheel.

robot better and in a safer way.

2.4.2.4 Electronics

To control this robot we decided to use a more complex electronics, supporting video processing and Wifi transmission. The general electronic schematics is shown in Figure 2.54. An *mx31moboard* is used as the main electronic board on the robot. It embeds an i.MX31 processor (see Appendix A.1.2 for details). This card handles a camera and Wifi transmission of the images and control commands.

Apart from this computer, microcontrollers are needed to control the actuators and sensors of the robot. One dsPic33 microcontroller is used in each wheel, and two in the body. Electronic modules to measure the motor current, speed and position are used for each motor (Appendix A.1.3). All the different electronic boards communicate together through a CAN bus.

The body microcontroller board controls a motor used for the rotation of the body. This board also controls a servo motor that locks and release the tail from the body, and the lighting LEDs for the camera. It embeds an accelerometer and a gyroscope to measure the orientation of the body.

Each wheel microcontroller board controls the wheel motor. They also embed an accelerometer, and two Hall sensors.

Battery modules can be plugged on the body and in the wheels. They can work in parallel thanks to ideal diodes and protection circuits.

The microcontrollers are programmed using the Aseba framework[13] (see Appendix A.2.2 for details).

2.4.2.5 Control

The i.MX31 receives the commands from the user through the Wifi connection. It interprets them and transmits them to the other microcontrollers. As the i.MX31 cannot

[13]The low-level was mainly programmed by Philippe Rétornaz.

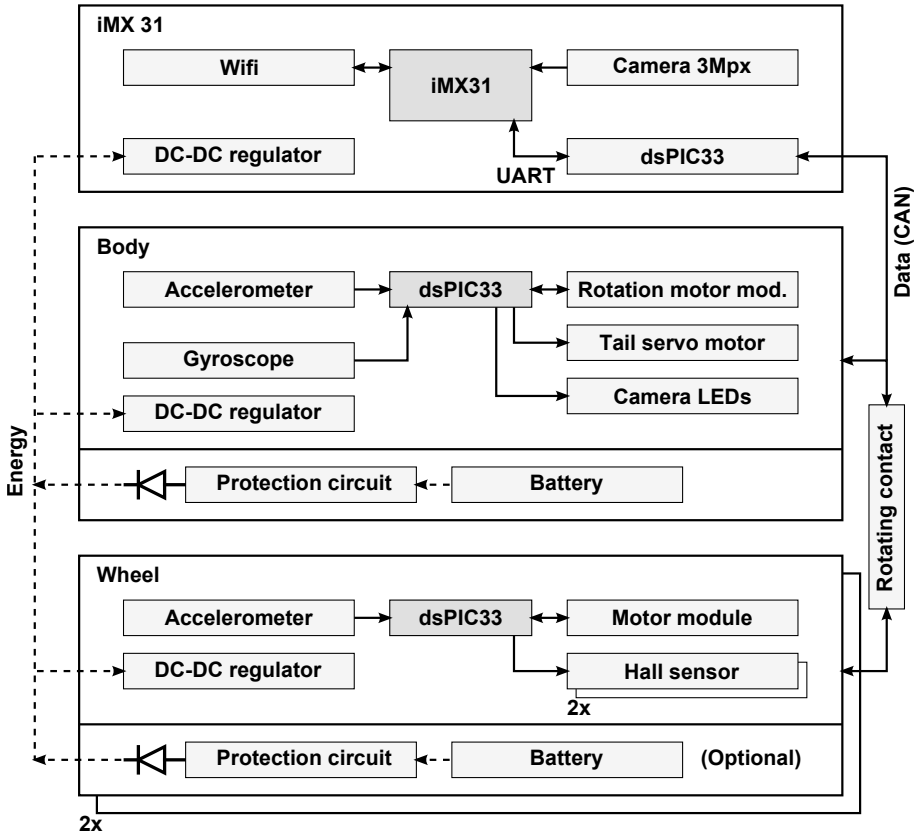

Figure 2.54: Cy-mag^{3D} II electronics.

communicate directly through a CAN bus, a microcontroller is used to translate the communication between CAN and UART.

A joystick connected to the computer allows to control the robot in speed and rotation. The body rotation is controlled by a second joystick. The tail can be fixed or released using a slider button.

A user interface on the computer displays the image from the camera, the orientation of the robot and the Hall sensors measures.

2.4.2.6 Results

The Cy-mag^{3D} II robot achieves a better mobility than the first version (Figure 2.55). For structures with vertical walls and 90° angles, the robot can pass inner and outer angles with no problems. The tail allows to pass in some situations that were not manageable with the first version of the robot. The tail can help to push the robot when going up, or slow down when going down.

The robot fails to pass angles where the tail is needed to push before passing and to slow down after passing, as the tail is not quick enough to pass from one side to the other in time. Inner angles smaller than 45° are also not possible to pass (depending on the orientation), as the magnetic system is not wide enough and will not get enough force on the new surface before loosing force on the first one.

The robot survived to two falls of an approximate height of 2 m. Some small damages occurred, but it could be fixed quickly. Making strong and solid robots is indeed important

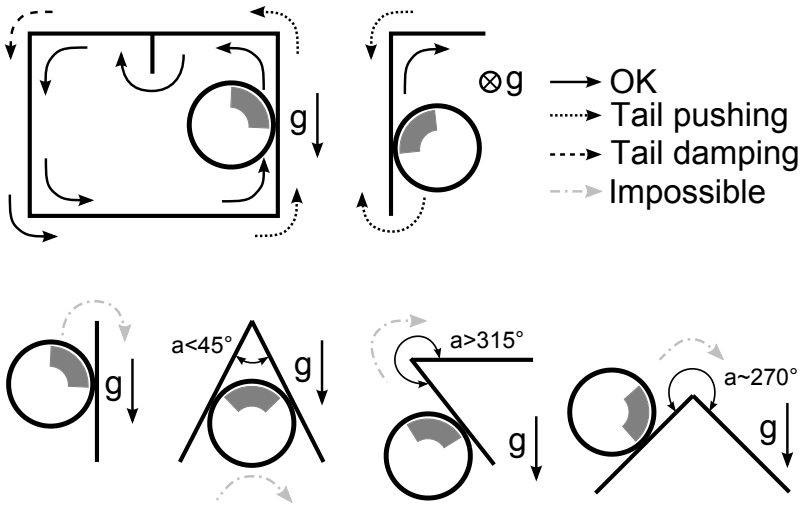

Figure 2.55: Cy-mag^{3D} II mobility results.

for climbing robots.

The body battery allows an autonomy of 30 minutes. Adding the wheel batteries doubles this time.

The magnetic flux monitoring works as expected. However, the signal is more noisy than on the calibration measures, as the robot oscillates back and forth around the equilibrium position. An example is shown in Figure 2.56(a), where the robot passes an inner angle and continues on the vertical wall. The signal is clean in the angle (the robot is stable), but a strong oscillation appears after the angle, corresponding to the mechanical oscillation of the system. However, the information is sufficient to help controlling the robot. Indeed, the user can control that the adhesion force is enough and corresponds to an inner corner transition phase. When the robot continues on the wall, the sensor gives information about the position of the magnetic system. The user can thus stop the robot if an unexpected signal is measured.

Figure 2.57 shows the signal when the robot reaches the end of a flat ferromagnetic plate. It corresponds to the rotation of the body, until the applied torque exceeds the magnetic torque, and the robot continues on the non-ferromagnetic surface. By monitoring this signal, the user can thus stop the robot before it falls down. This shows that these sensors increase highly the safety of the Cy-mag^{3D} II.

Another robot configuration was tested, by placing a wheel module behind another one, linked by a rigid structure (Figure 2.58). This bicycle configuration resolves the problems encountered before, when the tail can not push and slow down at the same time. Indeed, the back wheel can push or retain the front one and vice versa.

In this case the magnetic flux monitoring is very useful, as the magnetic systems are not linked any more. It is thus difficult to know their position and control the robot without this information.

This configuration requires at least an additional degree of freedom to be able to turn, but the tail is not needed anymore.

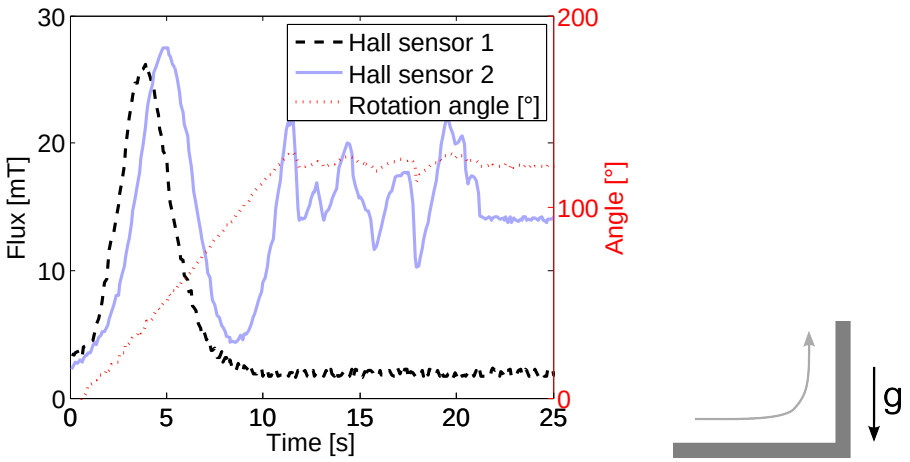

(a) (b)

Figure 2.56: Measures from the Hall sensors and rotation angle computed from the accelerometer, when the robot passes an inner corner from bottom to wall. The transition is finished when the rotation angle becomes constant. Hall sensor 1 is the front sensor, Hall sensor 2 the back sensor (as shown in Figure 2.52(b)).

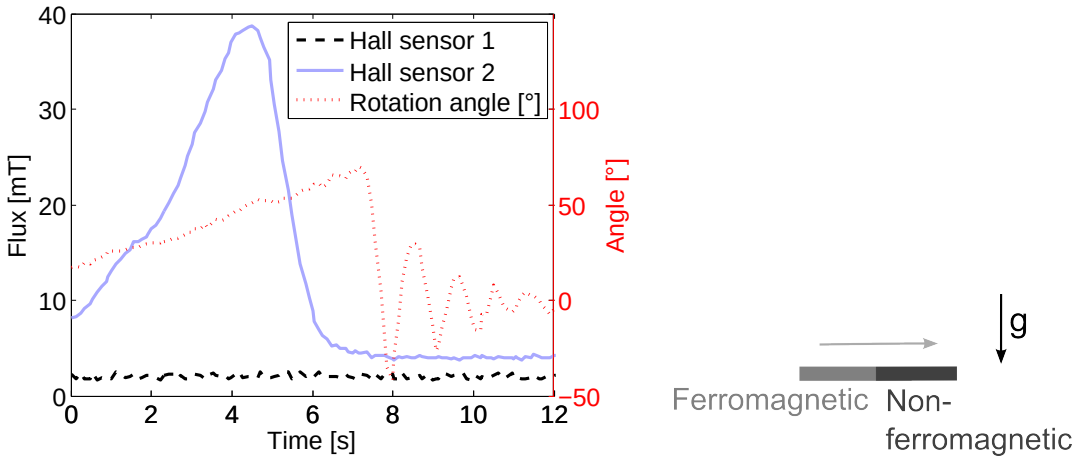

(a) (b)

Figure 2.57: Measures from the Hall sensors and rotation angle, when the robot passes from a ferromagnetic surface to a non-ferromagnetic one. The magnetic system rotates at the surface interface and the robot does not move, until the retaining torque becomes too low and the robot continues. Hall sensor 1 is the front sensor, Hall sensor 2 the back sensor (as shown in Figure 2.52(b)).

Figure 2.58: The bicycle configuration using the wheel modules.

2.4.2.7 Conclusions

A new version of the Cy-mag^{3D} is developed with added inspection capabilities. For this purpose, a camera and other sensors are integrated, which requires a bigger robot.

A wheel module using the Cy-mag^{3D} concept is designed and used on the new robot. The Cy-mag^{3D} II has the same mobility concept as the first robot, having a wheel on each side of a cylindrical shape. It achieves a better mobility thanks to its tail, allowing to push or slow down the rotation movements of the robot.

Hall sensors placed at each end the magnetic system give information about its position, and about the ferromagnetic properties of the surface the robot moves on. This feedback is important and helps controlling the robot. We would get more information if we could place many Hall sensors directly below the magnetic system. However, the flux is too strong for the typical range of Hall sensors ($< \pm 100$ mT), and the available room is too small.

Another robot configuration using two wheel modules is tested. The two wheels are placed one after the other, which allows each wheel to push or pull the other one. This improves the passage of some angles, and removes the need of the tail. However, another degree of freedom is required for the rotation of the robot, and the control is more difficult. The wheel module can also be used alone, or in other configurations such as tricycle or 4-wheel.

The vision performances and results of visual inspection using the Cy-mag^{3D} II are presented in Chapter 3.

2.5 Tube crawler robots

After these two types of climbing robots using caterpillars or advanced magnetic wheel, able to move on ferromagnetic surfaces and pass obstacles, we will now see the development of two tube crawler robots.

There are kilometers of tubes in power plants that require periodic inspections (see Section 1.4, page 2 for details). Most solutions to inspect small size tubes ($\varnothing$<50 mm) use endoscopic devices. These endoscopes have some limitations in terms of reachable distance, especially after bending. They also need a lot of room outside of the tube for the technician to push the endoscope, sometimes with high force. To overcome these

limitations, two robotic solutions were designed and tested. The aim is to increase the reachable distance in complex tubes with lots of bending, and to be able to inspect the tubes with many robots in parallel to increase the inspection speed.

The two Tubulo robots are designed to move in ferromagnetic tubes of 25 mm diameter. The locomotion principles use the fact that the tubes are ferromagnetic by using magnetic wheels for the first version, and MSDs for the second one. The expected advantage of magnetic adhesion is to adapt easily to different tube sizes, as the robots will stick on one side of the tube only. This is opposed to most tube climbing robots, which have systems that push mechanically on all sides of the tube. These systems usually adapt to diameters up to two times bigger than the smallest diameter they can move in.

The robots are made of different modules, connected to each other by flexible joints, so that they can pass the tube curvatures.

2.5.1 Tubulo I

The Tubulo I is composed of different modules having specific functions[14] (Figure 2.59(a)). It is designed to test the modular integration of a simple locomotion, a camera, sensors, communication, electronics and power on a tube crawler. Each module has a frame composed of two PCBs, that embed the electronics and are also used as mechanical structure. The modules have two magnetic wheels that keep them attached to one side of the tube.

Four main modules are used for the robot: the locomotion module, the energy module, the control and communication module and the visual inspection module. They communicate with each other through a CAN bus. The control and communication module (Figure 2.59(b)) sends commands to the others. The locomotion module has one motor driving a magnetic wheel, and is able to push or pull the entire robot. The energy module supplies energy to the other modules using a battery. The visual inspection module has a camera, LEDs and an accelerometer on board.

Using these four modules, the robot has a total length of 350 mm and a weight of 100 g. More than one module of each type, or new modules, can be connected to the robot. Details about the modules are presented in the next sections.

(a) Complete view of the robot Tubulo.

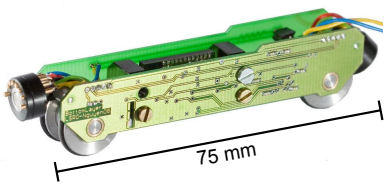

(b) Close-up of the communication module.

Figure 2.59: The Tubulo I.

[14]The Tubulo I was developed by Olivier Truong-Dat Nguyen in a master project under the supervision of Frédéric Rochat and myself [NRS+09].

2.5.1.1 Modules design

Moving in small curved tubes sets some geometrical constraints. The robot must be able to pass curvatures in the tube, and pass possible tube defects. Typical boiler tubes are in ferromagnetic steel of 25 mm in diameter, with 150 mm radius bends and weld joints up to 2 mm thick (which can reduce locally the diameter to 21 mm).

We chose to make the full robot by attaching several modules together like a train. It has the advantage of being flexible, so that it can pass curvatures, and it is more versatile, as modules can be added or changed easily.

The size of a module must allow it to pass in bendings. It must also allow to embed the crucial components such as motors, batteries and electronics. The size of the module is thus optimized to maximize its volume and pass bendings. Figure 2.60(a) shows a module in a bending. The maximum length L it can have depending on its width W is when its corners touch the external circle, i.e. position (x_1, y_1). The coordinates of this point are related with the circle equation:

$$x_1 = \sqrt{R_2^2 - y_1^2} \tag{2.23}$$

with $L = 2 \cdot x_1$, $y_1 = R_1 + W$, the bending radius $R = 150$ mm, tube diameter $d = 21$ mm, $R_1 = R - d/2$ and $R_2 = R + d/2$. A diameter of 21 mm has been chosen because of the possible diameter reductions due to weldings. The volume of the module, $W^2 \cdot L$ with respect to its width W is shown in Figure 2.60(b). The optimal width is around 16.7 mm with a length of 73.3 mm.

Similar calculations can be done to compute the wheels diameter so that the body does not touch the tube in down curvatures. We want the wheels to pass possible steps of up to 4 mm. They need to be at least twice this height to be able to pass this kind of obstacles. The final wheels are 12 mm in diameter.

Keeping in mind some constraints such as motor sizes, electronics and a safety margin, the final modules are approximately 75 mm in length with a square section of 15 mm width. This small size imposes a lot of restrictions for the mechanical and electronic design of the different modules.

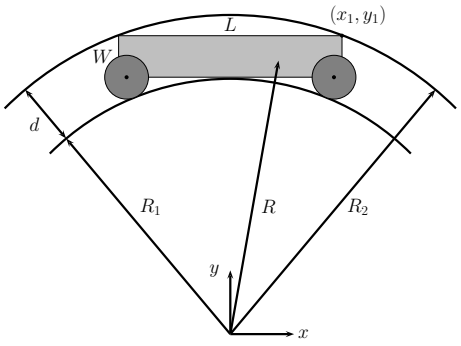

(a) Module length L and width W constraint.

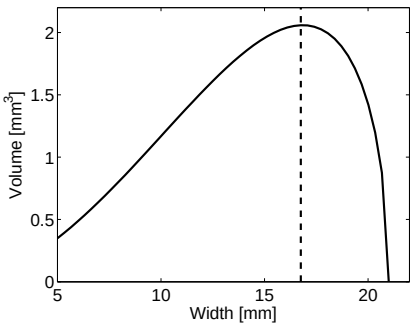

(b) Volume of one module depending on its width, the length being dependent on the width so that the module can pass bendings.

Figure 2.60: Tubulo I module size design.

2.5.1.2 Magnetic wheels

As the robot must move in tubes of any inclination, it needs a holding system. We choose to use magnetic adhesion to stick on one side of the tube. One advantage is that the robot can adapt to various tube sizes. Most tube climbing robots mechanically push on the sides of the tube, but they have usually diameter variations lower than 2 times.

We designed standard magnetic wheels, with a central magnet and two iron flux guides on the sides (Figure 2.61). One particularity is that they have no central axis passing through, leaving more space for the magnet.

Tests showed that the traction wheel can slip when pulling the robot. As the friction force F_f is proportional to the friction coefficient μ_f and the normal force F_n ($F_f = \mu_f \cdot F_n$), we can increase both values to reduce slippage. Increasing μ_f is difficult, as the rubber used has already a good friction coefficient (around 0.55). Reducing the air gap increases the normal force following an inverse-square law. We thus reduced the air gap from 0.85 to 0.15 mm, which increased the adhesion force from 250 to 600 g. This increased the friction force proportionally, which is now enough to pull the robot.

2.5.1.3 Electronics

All modules embed a dsPic33 microcontroller to control the communication, motor or camera. They are programmed using the Molole library (see Appendix A.2.1 for details), and communicate between each other through a CAN bus. The general electronic schematics is shown in Figure 2.62.

The control and communication module has a Bluetooth link to a computer. It allows receiving commands from the user, and sending the state of the robot such as its orientation, traveled distance or battery state. It works well in the small test tubes we tested (less than 1 m), but will not work in longer ones.

The locomotion module receives command information such as *forward*, *backward* or *stop*. This module keeps track of the traveled distance by odometry, counting the gear turns with a self made optical encoder. No commercial encoder could be integrated due to their size and the limited available space.

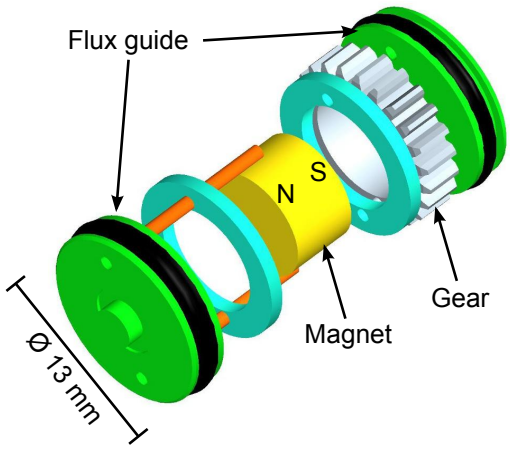

Figure 2.61: Magnetic wheel mechanical construction, with the magnet in the middle (yellow), and the flux guides on the sides (green).

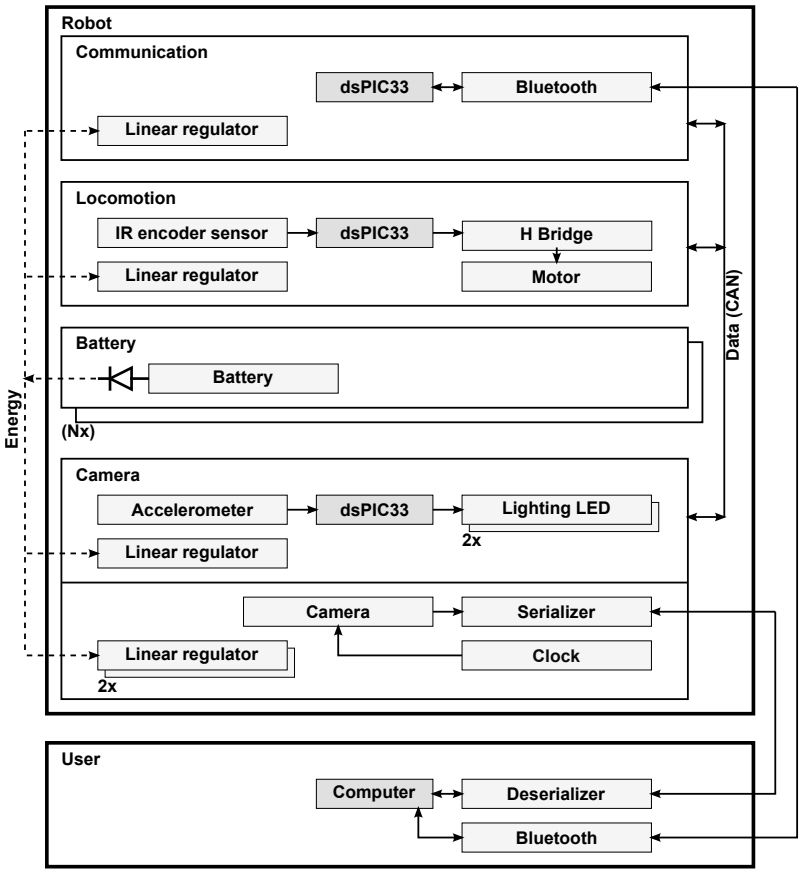

Figure 2.62: Tubulo I electronics.

A microcontroller in the camera module is used to control the lightning LEDs, and interface a 3D accelerometer. It receives commands and sends the orientations values through the CAN bus. The camera is independent from this electronics, it just takes its energy from the modules. The camera is plugged on a serializer, which allows to transmit the images over a twisted pair of cables. This will be explained in details in Chapter 3.

Several battery modules can be plugged in parallel on the robot, increasing its autonomy. Ideal diodes chips prevent batteries to charge from other batteries when their voltages are different (see Appendix A.1.4 for details).

2.5.1.4 Results

The Tubulo can move in straight ferromagnetic tubes of any orientation. It achieves a mean speed of 6 mm/s.

However, some difficulties arise in curves. The robot can pass tube bendings that are going up (Figure 2.63(a) and 2.64(a)), but get stuck in lateral and down bends (viewed from the robot), because of the friction from the modules structures, and because the front wheel comes off the tube on one side which reduces a lot the adhesion force (Figure 2.63(b)). Percentages of bend passing success depending on the angle are shown in Figure 2.64(b). 0° is the angle corresponding to an incoming up bend, 90, 180 and 270° correspond to left, down and right bends respectively. The graph was obtained by making 35 experiments, letting the locomotion module move in a bending of 150 mm radius with

(a) Tubulo I passing a curve going up.

(b) Tubulo I stuck in a lateral curve.

Figure 2.63: Tubulo I in curves.

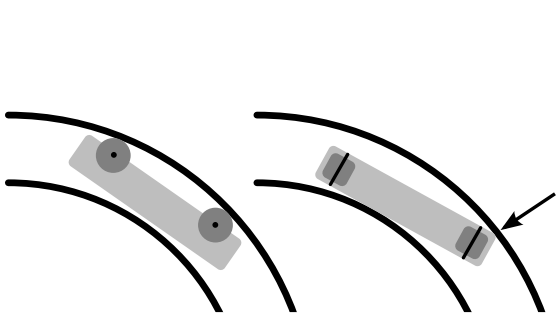

(a) Up bendings pass easily, but the robot get blocked in lateral and down ones.

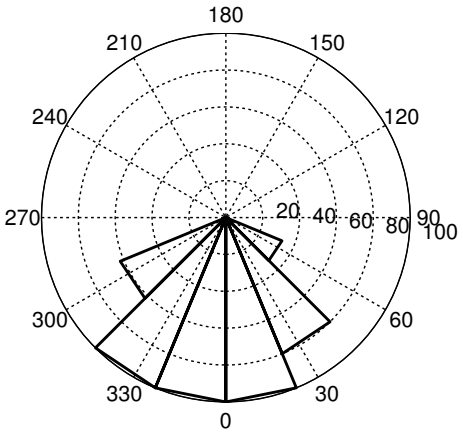

(b) Success of bend passing in %. 0, 90, 180 and 270° correspond to respectively up, left, down and right bends respectively. The bending has a 150 mm radius. Only upward bends are passing well, the robot is easily blocked in the other ones.

Figure 2.64: Tubulo I bend passing.

different orientations. We see that the robot can pass only the bendings going up.

Another problem is that the magnetic wheels tend to gather the ferromagnetic dirt. This dirt is difficult to clean. It also wears the gears of the locomotion wheel.

The self made encoder is unfortunately not fully reliable, as some counts are missed, and as the traction wheel can slip. Using a commercial encoder would give better results, but it would require a bigger module which would limit the mobility. Measuring the traveled distance on a free wheel would also be better, as there would be less problems due to slippage.

2.5.1.5 Conclusions

The Tubulo is a modular miniature tube crawler robot. It uses magnetic wheels to stick to one side of the ferromagnetic tubes it aims to move in. The small tube size (⌀ 25 mm) generates big constraints in the mechanics and electronics design.

The robot can move in straight tubes of any orientation. It passes bendings of 150 mm of radius going up with respect to the robot. However, it get blocked in left, right and down bendings. Increasing the radius of the bending would give better results, as the robot would touch less the tube with its structure. Increasing the magnetic and friction force would also increase the bend passing performances. Adding traction wheels, on the locomotion module or by adding another module, would also allow better locomotion results.

The magnetic wheels are gathering ferromagnetic dirt. It wears the gears of the locomotion module, and is difficult to remove.

Due to the locomotion and dirt problems, this solution is not convincing in terms of mobility performances. The next section shows a new robot design, aiming to overcome these problems.

2.5.2 Tubulo II

As the first version of the Tubulo was too much exposed to the environment (dust, ferromagnetic particles...), we designed a new version, with a focus on the environment resistance[15].

2.5.2.1 Modules design

To design an environment resistant robot, we kept a modular construction, but each module is enclosed in a capsule (Figure 2.65). This capsule protects the module from dust, particles, liquid and anything that could damage it. Each capsule is made by a cylindrical POM tube, closed by a cap on each side. The modules are connected by a silicon flexible joint. The joints are molded in the cap on each side to ensure a good tightness (Figure 2.66). Except the locomotion module, the capsules are waterproof. The modules must follow the same size rule as computed for the Tubulo I (Section 2.5.1.1).

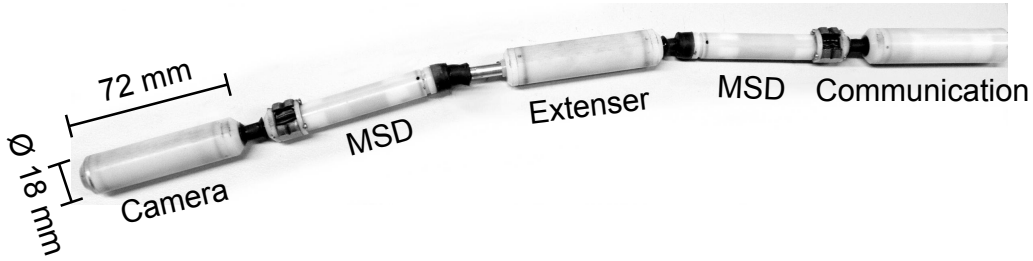

Figure 2.65: The Tubulo II with its different modules.

[15]The Tubulo II was developed by Olivier Truong-Dat Nguyen under the supervision of Frédéric Rochat and myself [NSRM09], except the extenser module which I redesigned.

2.5.2.2 Locomotion module

As the magnetic wheels have dust problems on the Tubulo I, another principle was applied by using MSDs. An inch-worm locomotion is used, with two MSDs placed between a module which can extend. The MSDs are switched on and off sequentially, and the central module extends and retracts accordingly, so that the robot moves forward (Figure 2.67).

For a better adhesion in the tubes, and for a better mechanical integration, the used MSD have a different functioning mode as the classic one[16] (Figure 2.68). Two cylindrical magnets with diametral magnetization are place side by side in a flux guide. The flux is switched on or off by turning one of the magnet by 180°. The MSD have a size of 16x16x10 mm (Figure 2.69). They achieve an adhesion force of 50 N on a steel tube of 25 mm diameter and 2 mm thick. The maximum activation torque of the MSD is 40 mNm.

The rotation of the magnet is done with a ⌀ 10 mm Faulhaber DC motor. Its output torque is 1.28 mNm. With a gearbox of ratio 64:1 and efficiency of 70%, the final output torque is of 57 mNm, which is enough to rotate the magnet. The half turn rotation required to activate or deactivate the MSD takes 0.22 s. The motor is enclosed in a module, with the MSD on one end (Figure 2.70).

Figure 2.66: Tubulo II silicon flexible connection between two caps.

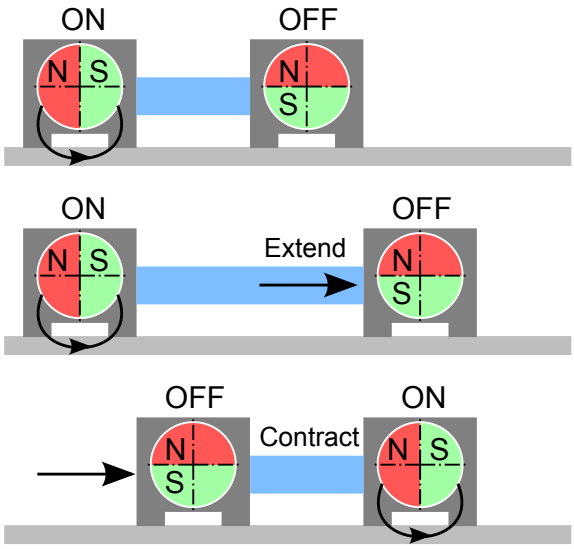

Figure 2.67: The Tubulo II inchworm locomotion principle.

[16]The MSDs from the Tubulo II were developed by Frédéric Rochat in his PhD [Roc11].

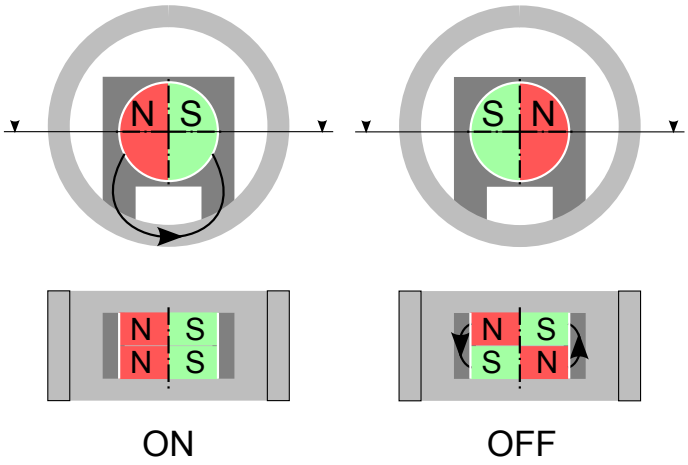

Figure 2.68: The MSD concept used for the Tubulo II.

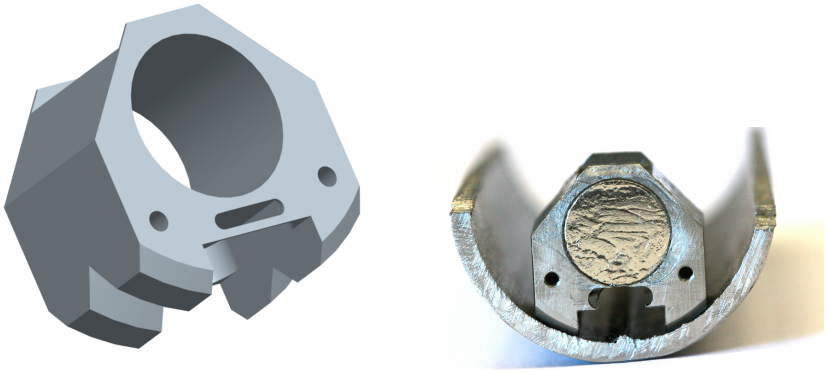

(a) (b)

Figure 2.69: (a) 3D view of the MSD Stator and (b) picture of the MSD in a cut tube.

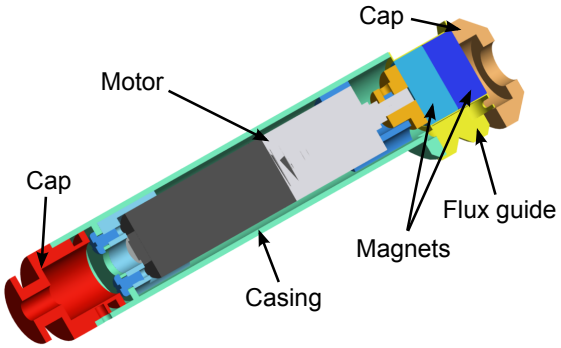

Figure 2.70: MSD module design (⌀13x86 mm).

The extenser module uses a linear screw-nut drive (Figure 2.71). To design the system, we need to compute the torque required on the screw, knowing that the system will have to pull a mass of 250 g. We can equate the work of the force to an estimate of the rotation work:

$$Fd = \eta T \alpha \tag{2.24}$$

with F the output force, d the traveled distance, η the efficiency, T the torque and α the traveled angle. The used screw has a M3 thread, with a pitch of 0.5 mm per turn. We can thus compute the required torque on the screw to push or pull the 250 g of the robot:

$$T = \frac{Fd}{\eta\alpha} = \frac{0.25 \cdot 9.81 \cdot 0.5}{0.2 \cdot 2\pi} = 0.98 \text{ mNm} \tag{2.25}$$

using an estimated efficiency of 20%.

A Maxon RE8 motor with a reduction gear of 1:15 (77% of efficiency) gives a usable torque of 7.23 mNm. This gives a good margin to overcome all the possible frictions that can occur. The final system has a stroke of 17 mm. It can be moved in 1 second, pushing up to 1 kg.

The final module has a size of 89 mm in length (minimum), and a diameter of 18 mm. The design of this module is difficult due to the difficulty to find small motors able to deliver such a torque. No encoder could be placed due to size restrictions. The module must also contain a PCB driving the extenser motor and the two MSD motors.

2.5.2.3 Electronics

The electronics is very similar to the first version of the Tubulo (Figure 2.72). Each module contains a microcontroller, programmed using the Molole library (see Appendix A.2.1 for details). They communicate together through a CAN bus.

The main difference is in the locomotion module, which needs to control three motors instead of one. The extenser motor is open loop controlled, but has magnetic bumpers at the ends of the stroke (Figure 2.71). A magnet is fixed on the moving part, and Hall sensors are placed on each end of the stroke. The motor is stopped when the Hall sensor detects the magnet. The MSD motors are also open loop controlled, using mechanical bumpers to stop the stroke. They are activated for a certain time to ensure the rotation of the magnet was complete.

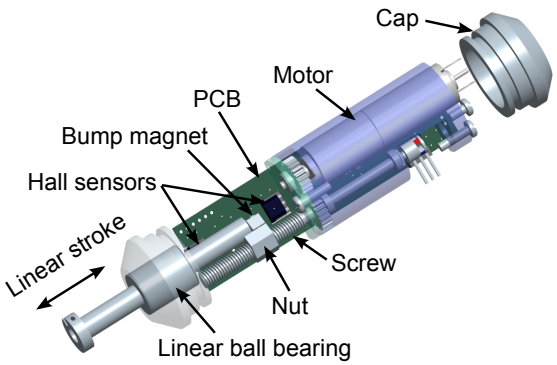

Figure 2.71: Extenser module design (⌀18x95 mm).

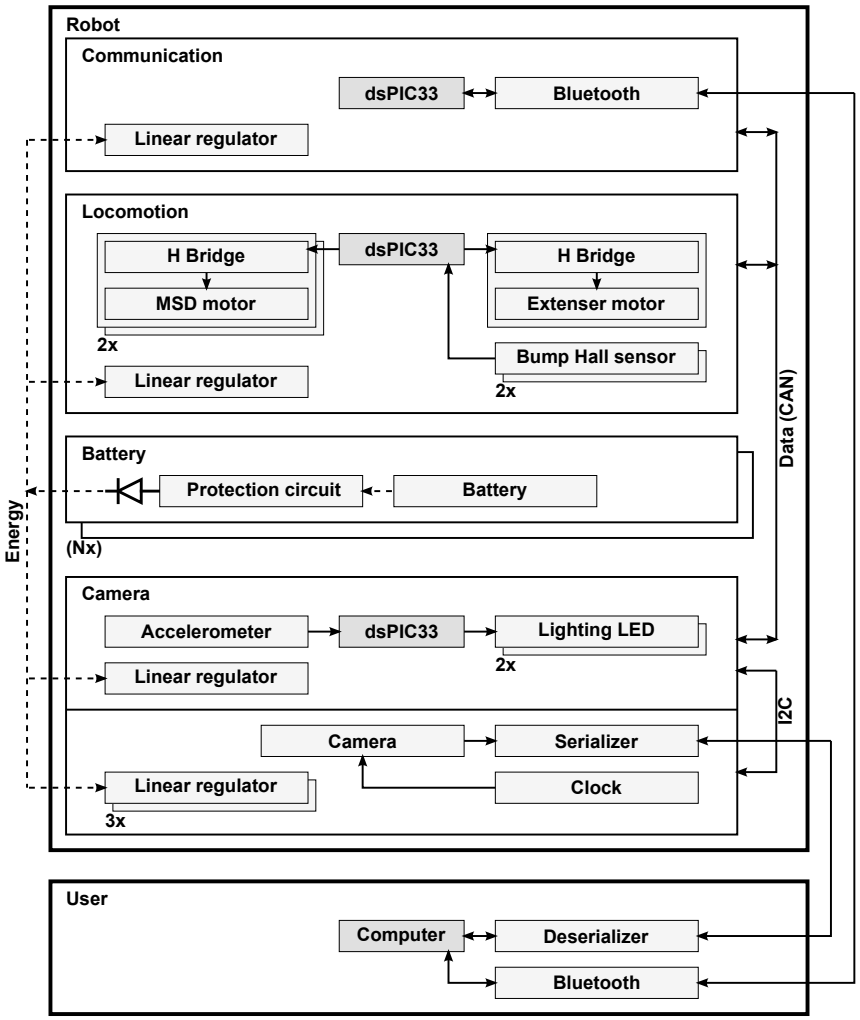

Figure 2.72: Tubulo II electronics.

The new smaller dsPic33MC802 microcontroller is used on the locomotion module. It has less connection pins, but enough for the needs. It allows to reduce the size of the PCBs and thus reducing the overall size of the module.

The battery module includes a protection chip that allows a safe use, avoiding over-charge, over-current or complete discharge of the lithium-ion battery (see Appendix A.1.4 for details). Several of these modules can be plugged in parallel on the robot, increasing its autonomy. Each battery has a measured capacity of 660 mAh. The mean consumption of the locomotion module is around 300 mA. Taking into account the other modules, the estimated time of use per battery is around 1.5 hour.

Six cables are required to connect the modules together (2 for the power, 2 for the CAN bus and 2 for the camera signal). Cabling in these modules is difficult because of the reduced available space, and very small cables are used (⌀ 3 mm).

2.5.2.4 Results

The locomotion principle is working well in the target tubes of ⌀ 25 mm (Figure 2.73). The robot achieves a mean speed of 18 cm per minute in straight tubes.

Up and down bends are easily passed through. However, left and right bends can cause difficulties, as the MSDs contact the tube surface on their sides, which have less adhesion force. Tubulo II achieves thus a similar mobility as Tubulo I in curves (Figure 2.64(b)).

The energy autonomy is of one hour using one battery module. It can be increased by adding other battery modules.

The robot was tested in used and dirty tubes of 50 mm diameter. The protection capsules are working well. No dust or particles were found inside the robot after the tests. The MSD are very easy to clean in the off position, even in such dusty environments (Figure 2.74).

Moving in bigger tube sizes is not a problem with low tube angles. However, in vertical tubes, the robot falls back and the MSD do not contact the tube surface with the correct side. This can lead to the fall of the robot.

2.5.2.5 Conclusions

The Tubulo II is a modular miniature robot moving in ferromagnetic tubes of 25 mm diameter. It combines two MSDs and an inchworm movement for locomotion.

To protect the robot from the dirty environment, the modules composing the Tubulo II are encapsulated in dust resistant casings. The MSDs are easily cleaned from the dust

Figure 2.73: Tubulo II in a ⌀25 mm tube.

Figure 2.74: Magnetic dust on the MSD. It is easily removable when the adhesion force is switched off.

and ferromagnetic particles when they are in the off position. The robot is thus resistant to the real environment of boiler tubes.

The robot can move in straight tubes and pass up and down bendings. It has problems to pass left and right bendings due to the fact that the MSDs have a lower adhesion force on the sides. This could be improved by making the MSDs cylindrical.

In bigger tubes, the robot has problems to stick on the surface and stay aligned in the tube axis. The expected advantage of the MSDs over mechanical systems to achieve a wider diameter range is thus not reached.

The Tubulo I and II robots were developed to increase the accessible range for tube inspection, as endoscopes are limited to tens of meters, and even less in presence of curves and other obstacles. The other aimed advantage of robots over endoscopes is that many robots can be launched in parallel tubes, decreasing the inspection time. However, the achieved speed and range are lower than endoscopes. Speed is difficult to improve for such small robots, but the range could be increased by increasing the mobility performances. Other systems should thus be explored like for instance adding a pulling system on the tip of endoscopes.

2.6 General conclusions on ferromagnetic mobility

In this chapter, we explored and designed new miniature magnetic climbing robots using innovative locomotion principles. The developed principles were an attempt to overcome the problems of the standard magnetic wheels, which get blocked in inner corners, may have too low friction forces and are difficult to clean of ferromagnetic particles. Simple locomotion systems allowed reducing the size of the robots and make their control easier. Embedding sensors on the adhesion systems allowed a safer control of the climbing robots.

Fixing a magnetic system on the frame of a robot, with an air gap between the system and the surface, reduces the adhesion force, but has a main advantage: a distance variation between the magnetic system and the surface induces fewer force variations than for a smaller air gap, as the force decreases exponentially with distance. Passing over paint, screw heads or other non-ferromagnetic obstacles reduces less the adhesion force, and controlling the robot in unknown environments is thus safer. The Tripillars use magnets fixed on the frame to create an adhesion force, and show good mobility using their caterpillars.

Magnetic wheels can have limited friction, when a liquid is present on the surface, for example. The friction force can be increased using other locomotion methods, such as caterpillars embedding magnets, as used on the Tripillar I.

To overcome the problem of the blocked magnetic wheel in inner corners, a new concept embedding a magnetic system rotating in a wheel was used on the two Cy-mag^{3Ds}. The system allows for passing inner angles with a very small force compared to the one required with standard magnetic wheels. The wheel module used for the Cy-mag^{3D} II can be used on other robot configurations, which can thus be designed quickly for specific applications.

Dust and small particles in the encountered ferromagnetic environments are often ferromagnetic. These particles are attracted by magnetic forces and difficult to detach if they are directly in contact with the magnetic systems. Particles attaching on magnetic wheels are difficult to remove and can reduce the wheel mobility by creating small obstacles and increasing the air gap. Magnetic systems fixed on the frame of the robot attract fewer of these particles due to the air gap. Particles attaching on the magnetic systems have no direct impact on the mobility of the robot, but may reduce the adhesion force by

closing the magnetic flux between the poles. The magnetic systems of the Cy-mag^{3Ds} are protected from these particles by the wheels. Even if particles are attracted to the wheel surface, they will fall when the wheel turns, as the particles will no longer be in front of the magnetic system. The MSDs of the Tubulo II are also easy to clean, as they can be switched off.

Adding sensors measuring the magnetic flux near the magnetic systems allows for measuring the adhesion force. This allows a safer control of the robots, as they can be stopped before falling when the force reduces.

All the developed robots can carry cameras or other NDT sensors. The vision systems integrated on the Cy-mag^{3D} II and the Tubulo II are shown in the next chapter. The Eddy current sensor embedded in the Tripillar II is described in Chapter 4.

3 Vision for Inspection and Control

3.1 Introduction

Now that we have mechatronic systems able to climb and move in complex ferromagnetic structures, the next step is to add sensing capabilities to inspect these environments. Visual inspection using a camera is the most straightforward inspection technique applicable. Moreover a camera does not only allow for inspecting visually, but it also allows for controlling the robot, as we may drive it into places where we can not see it anymore.

Sufficient processing power, memory and/or communication bandwidth is needed to save or transmit the images. Lighting is needed in most cases, as the environments are often closed and dark.

The choice of different components and methods such as cameras, image storage, processing and/or transmission are shown in the next sections. The use of a camera on the Cy-mag^{3D} II and the Tubulos is then detailed, showing the impact of several aspects on remote operation and inspection.

3.1.1 Camera

Many different camera types exist. Very small analog cameras can be plugged directly to analog monitors. They are easy to use and can be connected with cables over 100 m easily. However, their resolution and image quality is limited. Finally, a conversion is needed between the analog signal and the digital signal required for microcontrollers or computers.

We choose to restrict ourself to the use of digital cameras, which signals can be read and processed directly by digital electronics. We use two cameras that are well documented and can be easily integrated in a system: the small PO6030K and the bigger MT9T031.

The PO6030K camera from Pixelplus[1] is a very small CMOS color camera. It has a sensor of 2.36x1.78 mm, with a resolution of 640x480 pixels, and a pixel size of 3.6x3.6 μm. It has an external size of 21x6x4 mm, including the optics and the connectors. The focus can be slightly modified by turning the optics in the screw thread. It is used on the e-puck robot, developed in our laboratory [MBR$^+$09], and therefore we already have all the software to control it. We use this camera on the smallest robots, such as the Tubulo I and II for example. As the embedded microcontrollers are too slow for complex video processing, the image signal is transmitted to an external computer using a SerDes, which keeps a digital data format (see Section 3.1.3).

[1] Pixelplus Co., Ltd - CMOS Image Sensor: `http://www.pixelplus.com/`.

The MT9T031 camera from Aptina has a bigger sensor (6.55x4.92 mm) and resolution (3 Megapixels, 2048x1536 pixels), but slightly smaller pixels (3.2x3.2 μm). It can capture and transmit up to 12 frames per second at full resolution, and higher rates at lower resolutions. It has built-in digital pan, tilt and zoom functions. The camera has no auto-focus, but the focus distance can be modified manually by rotating the lens. This camera is used on the Marxbot robot [BLM+10], developed in the laboratory, and therefore we already have all the software to control it. We use this camera on the Cy-mag^{3D} II, directly connected to a processor by the camera bus.

3.1.2 Processor for image processing

The processor embedded in the robot is a limiting factor for image acquisition. For instance, the e-puck [MBR+09] embeds a microcontroller (dsPic30, 14 Mips) that can read color images of 40x40 pixels at a frame rate of 4 images per second only. The microcontroller can only read images of less than 4000 pixels (62x62 for example) due to its low amount of embedded memory (8 Kbytes of RAM). A raw 640x480 8-bit image needs already $640 \times 480 = 307.2$ Kbytes of memory.

The readable image size can be increased on the e-puck by writing the image on an SD card. However, the image must be read sequentially, reading 80 block of 480x8 pixels that can be stored on the microcontroller and copied to the SD card one after the other. In this case measures show that it requires 36 ms (9% of total time) to reconfigure the camera to read the next block, 333 ms (87%) to read the sub-images and 13 ms (4%) to copy it on the SD card. It takes thus more than 30 seconds to read the full resolution image (80 blocks). This is mainly due to the microcontroller, which has a limited speed to read the images. Even if this time would be shorter on newer microcontrollers of the same type, it is too long and other solutions must be used.

A first solution we used is to transmit the data directly to a computer. A SerDes is used to convert the data and transmit it on a twisted pair of cables (see next section). The data is then decoded and saved on the computer. This solution is good when a cable can be connected to the robot without limiting its mobility.

A second solution is to use a more powerful processor. The i.MX31 processor from freescale is used on the Cy-mag^{3D} II. It is mounted on an mx31moboard electronic board, which can process images from the Aptina camera in real-time. Details about this processor and board are found in Appendix A.1.2.

3.1.3 SerDes

A Serializer/Deserializer (SerDes) is a transmitter/receiver pair that converts parallel data to serial data for transmission, and vice-versa for reception [Lew04]. It allows to reduce the number of cables needed to transmit parallel data by using Low-Voltage Differential Signaling (LVDS). Differential signaling methods transmit the information as a voltage difference on a twisted pair of cables. This transmission method is well resistant to noise. Using low voltages (typically 350 mV), LVDS allows to transmit information at very high speed and increase the transmission distance between two devices.

For cameras, it allows to reduce the typical 10-bit data stream (8 bit for the image, and 2 for end of line and end of image data) to a single bit data stream running at a higher frequency. This signal can then be transmitted over a twisted cable pair over 10 meters. The signal is then converted at the receiver to parallel again.

A SerDes electronic board pair was developed in the laboratory[2] (Figure 3.1). The SerDes uses the DS90UR241Q serializer from National Semiconductor, which is mounted on a PCB which size is 33x12x4 mm. The deserializer is the DS90UR124Q chip, and is mounted on a bigger PCB which measures 90x19x17 mm. This PCB also includes a microcontroller (CY7C68013 FX2 from Cypress), which ensures an high speed USB connection with the computer. The serializer is connected to the deserializer by 2 cables. Two other cables are required for the power, and two others for the I^2C connection used to initialize the camera. The power cables can be removed if batteries from the robot can power the onboard electronics. The I^2C cables can also be removed, if a microcontroller on the robot sends the initializations data to the camera directly.

The final system can transmit 640x480 color images at 15 frames per second, over a distance of 10 meters. This is a data rate of 37 Mbits/s.

3.1.4 Wireless transmission

To remove the cable connection from the robot, we need a wireless transmission method. Many different numerical wireless communications protocols exist. Important characteristics of some of the most used ones are shown in Table 3.1.

We need a range higher than 10 m, and a data rate above 25 Mbit/s to transmit 640x480 color images (8 bits) at 10 frames per second ($640 \cdot 480 \cdot 8 \cdot 10 = 24.6 \cdot 10^6$). We must thus exclude the Wireless USB and Bluetooth because of the limited range, and the ZigBee because of the low data rate. WiMax needs a complex infrastructure. We thus choose the Wifi protocol, which has a good data rate (100 Mbit/s), a good range (100 m) and is widely spread.

One problem of high data rate wireless transmission is the high energy consumption. For example, the Wifi dongle we are using is consuming 1.2 Watts on average, which is equivalent to one motor of the robot.

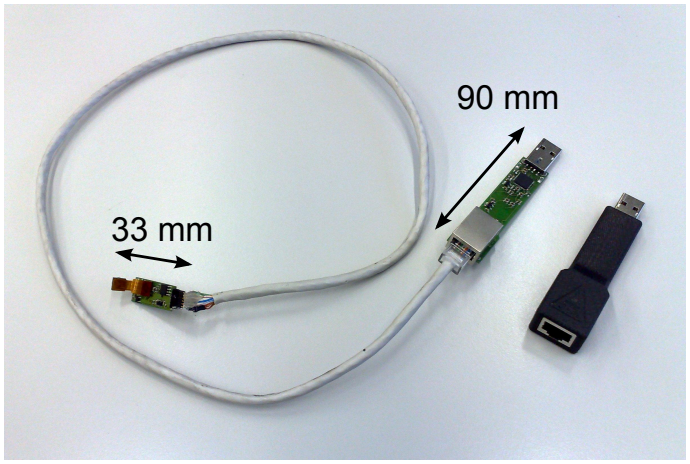

Figure 3.1: SerDes full system, with the camera and serializer on the left PCB, and the deserializer, microcontroller and USB on the right PCB.

[2]The SerDes electronic was developed by François Rey [Rey09].

Table 3.1: Numerical wireless communication protocols

Type	**Frequency**	**Typical data rate**	**Range**	**Comments**
Wifi (802.11n)	2.4 & 5 GHz	100 Mbit/s	100 m	+ Good range and data rate - High power
Wireless USB	3.1-10.6 GHz	110 Mbit/s	10 m	+ Good data rate - Limited range
WiMax (802.16)	2-66 GHz	70 Mbit/s	50 km	+ Excellent range and data rate - Complex infrastructure
Bluetooth 2.0	2.4 GHz	2.1 Mbit/s	10 m	+ Low power and reasonable data rate - Limited range
ZigBee (802.15.4)	868 kHz	20-250 kbit/s	200 m	+ Good range and low power - Low data rate

3.1.4.1 Tube as a waveguide

Standard wireless transmission is not usable over long distances in metallic tubes, as the signal is attenuated in the tube. However, a conducting tube can be used as a waveguide for electromagnetic signal transmission. A cutting frequency exists, under which the attenuation of the signal is very strong. This cutting frequency depends on the tube diameter, as given in Equation 3.1, with an example for a diameter of 25 mm [Eom04].

$$f_c = \frac{c}{2\pi}\frac{\chi'}{r} = \frac{3 \cdot 10^8}{2\pi}\frac{1.841}{0.025/2} = 7.03 \text{ [GHz]} \tag{3.1}$$

where c is the speed of light, r is the radius of the tube, and χ' is a constant depending on the wave mode. For a tube of 25 mm diameter, we need a frequency above 7 GHz. We can see from the formula that if we reduce the tube diameter, the cutting frequency increases (Figure 3.2). A special antenna is also needed to create the right wave form. Here the $TE_{1,1}$ mode (transverse electric field) is chosen, which has the lowest cutting frequency.

Using standard 2.4 GHz communication, we cannot transmit data efficiently in tubes smaller than 75 mm in diameter. This value reduces to 35 mm for 5.2 GHz.

The miniature tube crawler from Tsuruta and al. is transmitting 2.5 Mbit/s wirelessly in ⌀ 10 mm tubes at 22 GHz [TSK01]. However, no standard electronics is available, and it requires specific developments and designs.

3.1.5 Storage supports

Another solution to get high resolution images from the robot is to store them on the robot, and read them when the robot comes back from the inspection. For this we need storage capabilities on the robot. Physically removable storage is an advantage: if the data is saved on a removable card, we can then just take the card and plug it in a computer to look at the images, like on standard cameras.

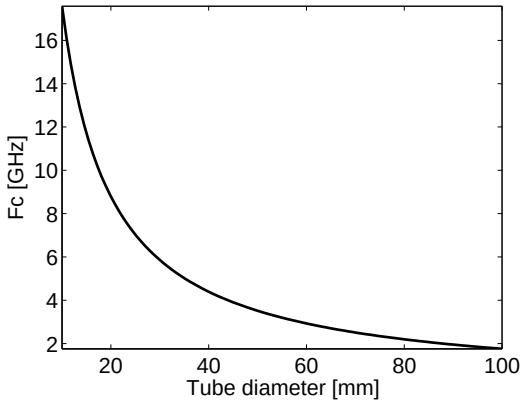

Figure 3.2: Cutting frequency of electromagnetic signal transmission in tubes, depending on the tube diameter.

SD cards are ideal for this applications. They contain up to 32 GB of flash memory in a very small volume. MicroSD cards have a size of only 15x11x1 mm for example. One of the standard protocol (SPI - Serial Peripheral Interface Bus) to read and write on SD cards is open, it is thus easy to interface them with microcontrollers, and allows data rates up to 50 Mbit/s. Another advantage of flash memory is the low power consumption, less than 0.3 W for a microSD card for example.

3.1.6 Conclusions

Embedding a vision system on an inspection robot requires the integration of several components allowing to create, process, transmit and view images. The choice of different components and technologies was showed and explained in the previous sections.

Wireless transmission of the images is preferred, as the robot mobility is not reduced by cables in this case. However, it is not always possible to transmit the images wirelessly. The electronics requires some space, which is not always available on miniature robots. The environment can prevent the transmission of electromagnetic signals, as in ferromagnetic tubes for example. In these cases the transmission of the images over cables is needed. A SerDes electronics allows to use a twisted pair of cables only for image transmission, and can transmit images over 10 m.

The vision systems embedded on the Cy-mag^{3D} II and the Tubulo robots are now described, as well as the obtained performances and results.

3.2 Vision with the Cy-mag^{3D} II

The Cy-mag^{3D} II locomotion principle, mechanics and electronics were presented in Section 2.4.2. We focus now on the vision part, embedding a camera and the required electronics on the robot to perform visual inspection and remote control the robot. To compensate for some weaknesses of the visual feedback of the camera, a distance sensor is designed using a laser coupled with the camera. The distance information included in the camera view enhances the perception of the remote operator and demonstrated to be very useful in inspections.

3.2.1 Electronics

The electronics should support a camera on the robot and transmit the images to the user. For this purpose we need a wireless transmission, as cables would reduce the mobility of the robot. We decided to use the standard Wifi protocol as discussed before in Section 3.1.4. We need thus a sufficient computing power to read, use and transmit the images.

To achieve the requested performances we use an i.MX31 processor on an mx31moboard as the main computer (see Appendix A.1.2 for details).

The Aptina 3 Megapixels camera is connected to the processor (see Section 3.1.1). The camera has a 42° horizontal field of view with the chosen optics. It is equivalent to a standard 50 mm focal length on a reflex camera, which is close to the human natural viewing angle.

A Wifi USB dongle is connected to the board. It allows communication between the robot and the user computer, and the transmission of the images.

As the robot will inspect dark places, lighting LEDs are needed to have sufficient illumination for the camera. An LEDs ring is fixed around the camera (Figure 3.3). It contains 16 LEDs, divided in 2 groups, each one controlled by a LED driver. The intensity of each group can be driven separately.

Figure 3.4 shows an image taken by the camera in an air duct. It is difficult to know the scale of the different components in the image. The next section shows the design of a distance sensor, which will allow to make measurements and get a better knowledge of the environment.

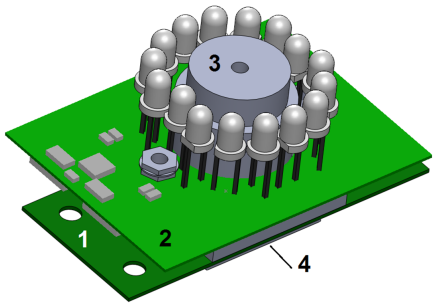

Figure 3.3: LEDs ring around the camera of the Cy-mag^{3D} II. (1) Camera PCB, (2) LED PCB (40x29 mm), (3) camera and (4) camera connector.

Figure 3.4: Camera view of the Cy-mag^{3D} II in an air duct.

3.2.2 Laser triangulation distance sensor

When we control the robot without viewing it, the main source of information comes from the camera. However, it is difficult to estimate sizes and distances in unknown environments only by looking at an image. Therefore adding a distance information within the image would radically improve the information available for the remote operator.

Distance sensors such as infrared or ultrasound sensors are often used to detect obstacles in mobile robots. The main principles used to measure distances are: reflected light IR, triangulation IR, ultrasonic time of flight and laser time of flight (ToF) or triangulation. Table 3.2 shows the main characteristics of one sensor of each type.

One disadvantage of the ultrasonic sensors is that they measure the shortest distance found in a cone in front of them: it is thus not possible to know the exact location of the measure. The triangulation IR sensors are focused, but we cannot check precisely where the measurement is done. The laser triangulation sensors are precise, but big and expensive. These sensors may also be disturbed from the reflections of the signals on the metallic surfaces found in the environments.

As we already have a camera, a laser triangulation sensor is a good solution, as we only have to add a laser to the system [GCMD11]. The working principle of laser triangulation is shown in Figure 3.5. A laser is placed beside a camera, with its beam crossing the optical axis with a certain angle. The laser will light a dot on the first surface it encounters. The image position of the dot will change depending on the obstacle distance. The distance to the laser dot can thus be calculated from the laser image position. A big advantage of this laser sensor is that we can see exactly where the measure is done, integrating the information directly on the video feedback of the operator.

3.2.2.1 Theory for optimization

To optimize the laser triangulation sensor, we need to know the theoretical function of the distance with respect to the laser image position. As the laser and camera positions are exchanged in our system compared to the standard ones, we need to compute this function as it is slightly different from the existing systems [JL89]. First we compute the

Table 3.2: Comparison of different types of distance sensors

Type	**Model**	**Dim. [mm]**	**Range [cm]**	**Precision [mm]**	**Price [$]**
Reflected IR	Vishay TCRT1000	7x6x2.5	2-10	>0.2	∼1
IR triangulation	Sharp GP2Y3A-002K0F	40x20x18	20-150	>2	∼35
Ultrasonic	MaxBotix LV-MaxSonar-EZ4	20x22x16	0-645	>25	∼25
Laser triangulation	Micro-Epsilon optoNCDT 1710-1000	200x83x48	100-200	>0.1	∼200 (?)
Laser ToF	Dimetix DLS-C 15	150x80x55	0-6500	>1.5	∼1200

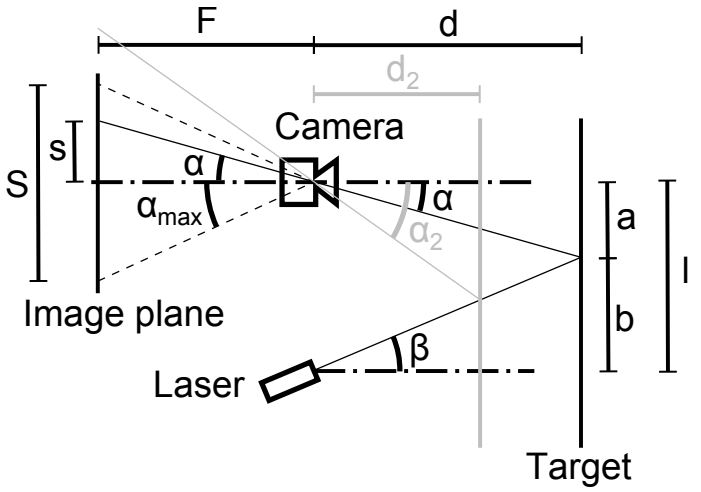

Figure 3.5: Laser triangulation distance sensor principle.

distance of the dot with respect to the laser angle β and the image angle α. We can write:

$$\tan\alpha = \frac{a}{d} \tag{3.2}$$

$$\tan\beta = \frac{b}{d} \tag{3.3}$$

$$a + b = l \tag{3.4}$$

where a is the distance between the dot and the camera optical axis, b the distance between the dot and an axis parallel to the optical axis passing by the laser, and l the distance between the camera and the laser. We replace a and b from the first two equations in the third one, and extract d:

$$d(\alpha) = \frac{l}{\tan\alpha + \tan\beta} \tag{3.5}$$

We now want the distance with respect to the pixel position. The maximum viewing angle of the camera α_{max} is linked to the width of the camera sensor S, and the focal length F:

$$\tan\alpha_{max} = \frac{S/2}{F} \tag{3.6}$$

We can extract F and replace it in the following equation:

$$\tan\alpha = \frac{s}{F} = s\frac{\tan\alpha_{max}}{S/2} = p\frac{\tan\alpha_{max}}{P/2} \tag{3.7}$$

where s is the position of the laser dot on the camera sensor. The pixel position p and pixel number P can replace the image position s and sensor width S, as they are linked by the relation: $\frac{s}{S} = \frac{p}{P}$. We can now insert $\tan\alpha$ in Equation 3.5 to get the distance with respect to the pixel position p:

$$d(p) = \frac{l}{p\frac{\tan\alpha_{max}}{P/2} + \tan\beta} \tag{3.8}$$

Finally, the derivative of d is:

$$\frac{\mathrm{d}d}{\mathrm{d}p} = \frac{-l\frac{\tan\alpha_{max}}{P/2}}{\left(p\frac{\tan\alpha_{max}}{P/2} + \tan\beta\right)^2} \tag{3.9}$$

It gives indications about the error of the system. The derivative $\mathrm{d}p/\mathrm{d}d$ is needed to analyze the sensitivity of the sensor. First we extract p from Equation 3.8:

$$p(d) = \frac{P/2}{\tan\alpha_{max}}\left(\frac{l}{d} - \tan\beta\right) \tag{3.10}$$

We can then compute the derivative:

$$\frac{\mathrm{d}p}{\mathrm{d}d} = \frac{-P/2}{\tan\alpha_{max}}\frac{l}{d^2} \tag{3.11}$$

Now we can analyze these equations which will help us to design the sensor. As the camera is defined (fixed P and α_{max}), the only parameters we can act on are the laser position β and l.

From Equation 3.11, we see that the sensitivity does not depend from β, but from d and l. As it depends from d, the sensitivity is not constant over the full range of the sensor, and decreases with distance. This is confirmed by the derivative curves shown in Figure 3.6. Increasing l is the only mean we have to increase the sensitivity of the sensor. However, increasing l also increases the minimal measurable distance (see Figure 3.7(b) on the right), as the laser dot will not be on the image at small distances (see Figure 3.5, α_2 in gray). Choosing l is thus a trade-off between sensitivity and minimal measurable distance.

To use the full range of the camera, β must be greater or equal to α_{max}, otherwise pixels on one side of the image will never be used (Figure 3.7(a), on the left). To measure up to infinity, β must be smaller or equal to α_{max}, otherwise the laser dot will leave the image after a certain distance. We must thus choose between sensitivity and range. To avoid the asymptotic part of the curve, where the sensitivity is very low, we choose to limit the range of the sensor, with a β angle slightly bigger than α_{max}.

Based on this and on mechanical considerations, we choose l=8.3 cm and β=23.4°, for an expected measurement range between 10 and 250 cm, with corresponding absolute sensitivities between 50 to 0.1 pixels/cm.

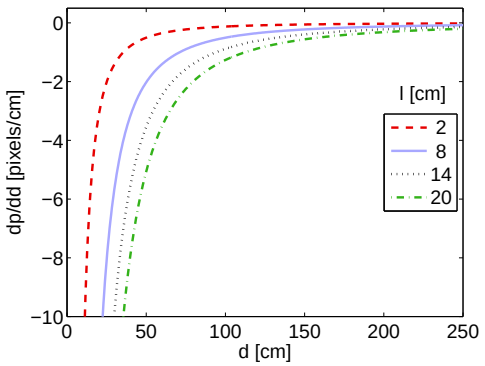

Figure 3.6: Sensitivity $\mathrm{d}p/\mathrm{d}d$ of the distance sensor for different l, with α_{max}=22° and P=512 pixels.

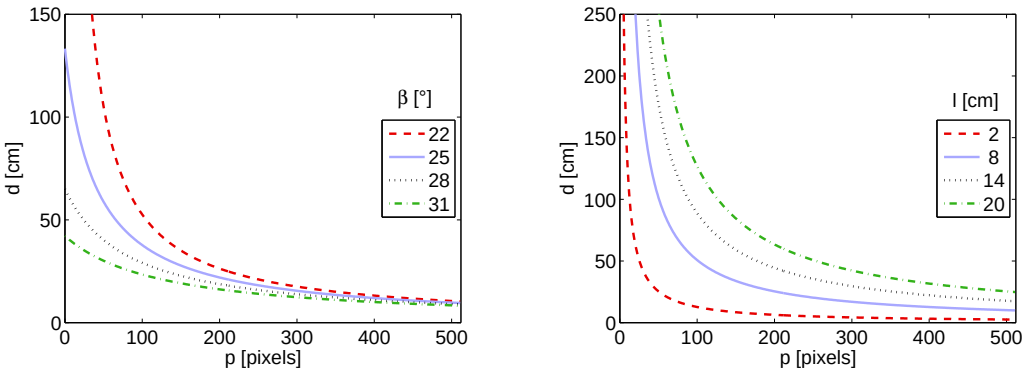

(a) (b)

Figure 3.7: Distance d with respect to the laser dot image position p, for (a) varying β (l=8.3 cm) , and (b) varying l (β=22°), with α_{max}=22° and P=512 pixels.

3.2.2.2 Hardware

A red laser (wavelength of 650 nm) of class II is used, with a power lower than 1 mW. Eyes are normally protected by blinking reflexes for this security class which is thus not dangerous. The laser emitter is very compact, with a length of 16 mm and a diameter of 6 mm, including the drive electronics.

The laser is fixed on the robot, at a distance l of 8.3 cm from the camera axis. For mechanical reasons it could not be placed on the robot main axis. It is placed at 1.8 cm of the axis, pointing downwards. The laser is thus not in a plane parallel to the camera horizon, and the laser image is thus not moving on an horizontal line, but moves on an inclined line. However, it does not change the measuring principle and theory.

The laser can be turned on and off using the user interface.

3.2.2.3 Software

The detection of the laser position in a dark image is easy and can be done with many different methods, looking at the high intensity pixels for example. However, other high intensity pixels are present in many cases, coming from light sources, LEDs reflections (Figure 3.8(a)), laser reflection in corners (Figure 3.9), etc.

As the laser is not in a plane parallel to the camera horizon, the line where the laser moves on the camera image is not horizontal but has an inclination. We can thus restrict the laser image search area on this line (Figure 3.8(b)). This allows to get rid of most of the lighting LEDs reflections, and of the laser reflection in corners for example, as they are not on this line except if the corner is almost perpendicular to the detection line (Figure 3.9).

We can also use the fact that we know the size of the laser dot, which changes with distance: it has a width of around 24 pixels for the closest distances, and reduce to 6 pixels at the bigger distances. We can thus focus the search to high intensities peaks of width corresponding to the distance. This can be done using a convolution of the signal with a difference of Gaussians (DOG, [Rus11]), which is used in blob detection algorithms

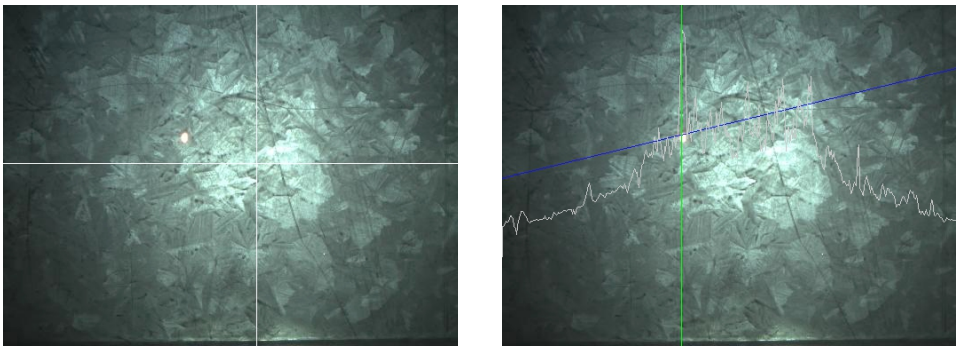

(a) Maximum intensity on the full image: LED light reflections have more intensity than the laser dot.

(b) Maximum intensity on the laser dot possible position line (blue). This method is more robust to other light sources.

Figure 3.8: Laser dot detection methods.

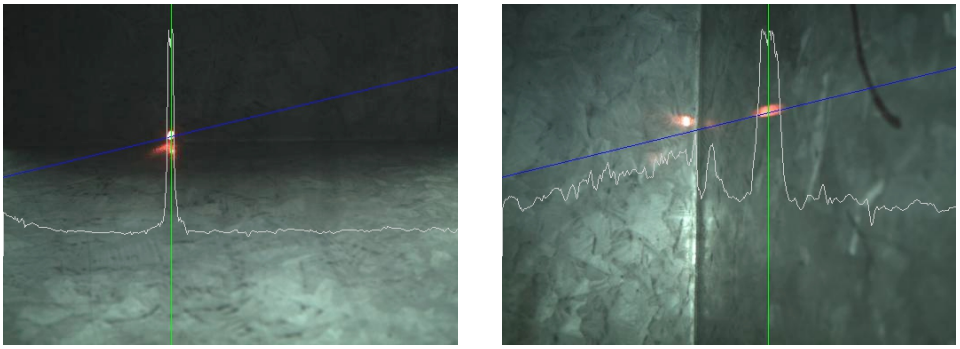

(a) Horizontal corners do not cause problems as the reflection is not on the detection line.

(b) Vertical corners may cause problems if they are almost perpendicular to the detection line.

Figure 3.9: Laser dot detection in corners.

for example. The DOG equation is defined as (Figure 3.10):

$$c_p = \sum_{j=-3w_i}^{3w_i} \frac{v_{p-j} - \bar{v}}{v_{max}} \left(\frac{1}{\sigma_{1p}} e^{\frac{-(x_j-\mu)^2}{2\sigma_{1p}^2}} - \frac{1}{\sigma_{2p}} e^{\frac{-(x_j-\mu)^2}{2\sigma_{2p}^2}} \right) \tag{3.12}$$

With $\sigma_{1p} = w_i/4$, $\sigma_{2p} = w_p$, μ=0, v_{max}=255. w_p is varying from 6 to 24 pixels linearly with the distance, following this relation:

$$w_p = 24 - (d(p) - 10)\frac{24-6}{220-10} \tag{3.13}$$

10 being the minimal and 220 the maximum measurable distance of the system. The signal value v is centered (by removing its mean $\bar{v}$) and scaled before the convolution, so that constants are independent to the signal.

A weighted average over the high intensity values of the convolution returns the middle of the peak $\bar{p}$:

$$\bar{p} = \frac{\sum_{p=1}^{n} c_p p}{\sum_{p=1}^{n} c_p} \tag{3.14}$$

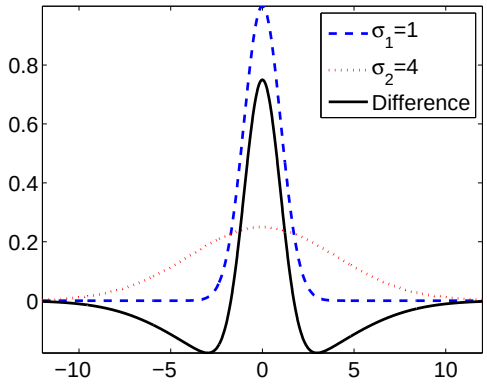

Figure 3.10: Difference of Gaussians (DOG) with $\mu = 0$, σ_1=1 and σ_2=4.

with c_p the convolution intensities, p the pixels position and n the number of pixels. We limit the computation to high intensity convolution values. Taking only the values with intensities above 60% of the maximum intensity c_{max} gives good results. The distance is then computed using Equation 3.8.

Figure 3.11 shows the result of this algorithm on a dark image with a horizontal corner. On the lower right graph, the result of the convolution, as well as both ends DOG curves are shown. The dot is well detected and its center is found precisely. The reflection of the laser in the corner does not pose problems, as it is not on the detection line.

Figure 3.12 shows the result on a difficult images, having a strong LEDs light reflection in the middle. The peak with the correct width is detected, despite the strong signal from the LEDs, thanks to the correct width detection. However, it would fail if the laser would be in the middle of the LEDs light reflection.

A final improvement is possible by selecting only the red colors corresponding the laser light. For this, one solution is to pass from RGB (Red, Green, Blue) coding to HSV (Hue, Saturation, Value) (see Appendix A.3.2 for details). The decomposition of each HSV signal from picture 3.12(left) is shown in Figure 3.13. There is a clear difference between the laser and LEDs in the saturation part. The hue allows filtering from other colors, and the value allows removing the low lights. To select the laser light, we thus keep the value of the pixels following these conditions:

$$H < 0.2 \text{ or } H > 0.8 \tag{3.15}$$
$$S > 10^{-4} \tag{3.16}$$
$$V > 0.1 \tag{3.17}$$

The result of this filtering, followed by the convolution algorithm, is shown in Figure 3.14. The strong intensity LEDs reflection is almost completely removed from the image. The processing is thus easier after this filtering.

These algorithms are quite robust to external lights and reflections, but they are best used in indoor environments with low light intensities. Even that they were tested on many different images and conditions, they depend on manually tuned constants and thresholds, and may not work in some conditions. As the operator sees if the detection of the laser is correct or not, he can select the best working algorithms for the encountered conditions. Reducing the LEDs intensity, or the camera exposure is also improving the laser detection.

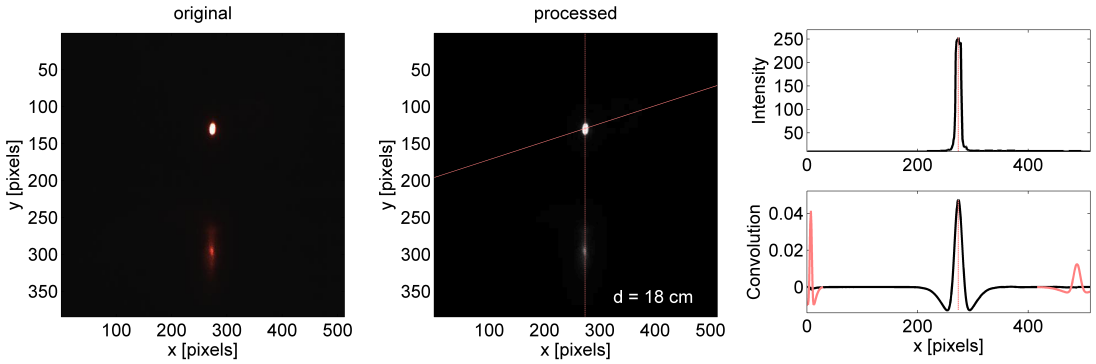

Figure 3.11: Laser detection using a convolution with a DOG of varying width. Both ends DOGs are shown on the lower right graph (red). A corner creates a second reflection which does not disturb.

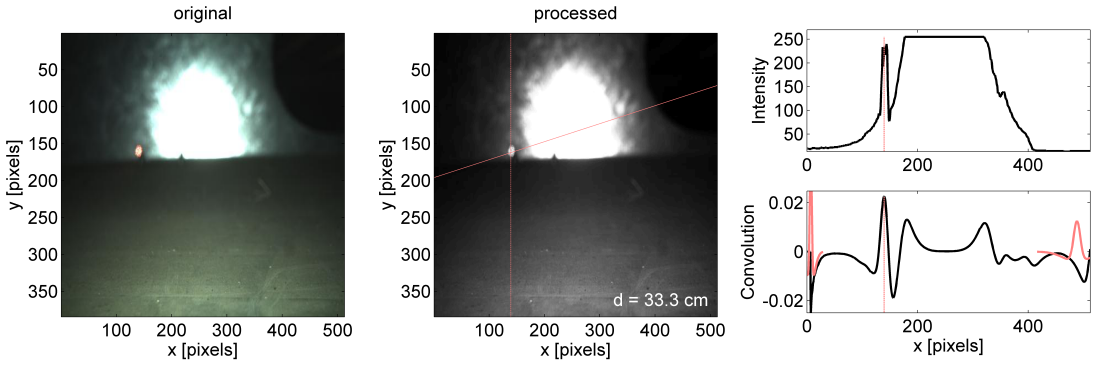

Figure 3.12: Laser detection using a convolution with a DOG of varying width.

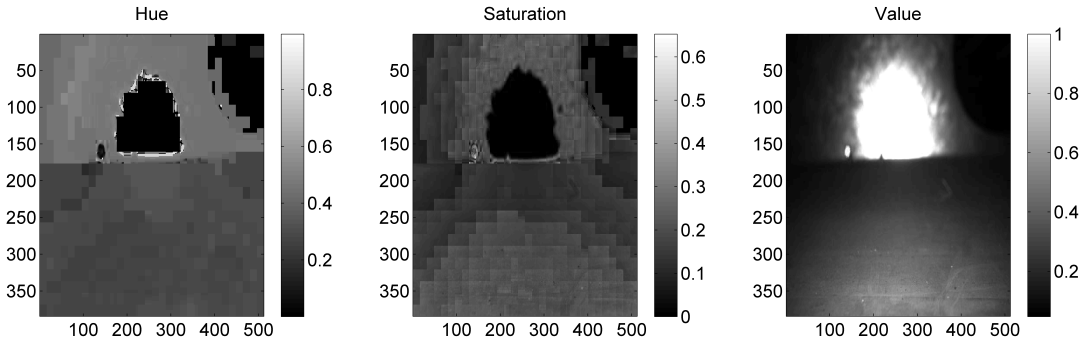

Figure 3.13: HSV decomposition of the image.

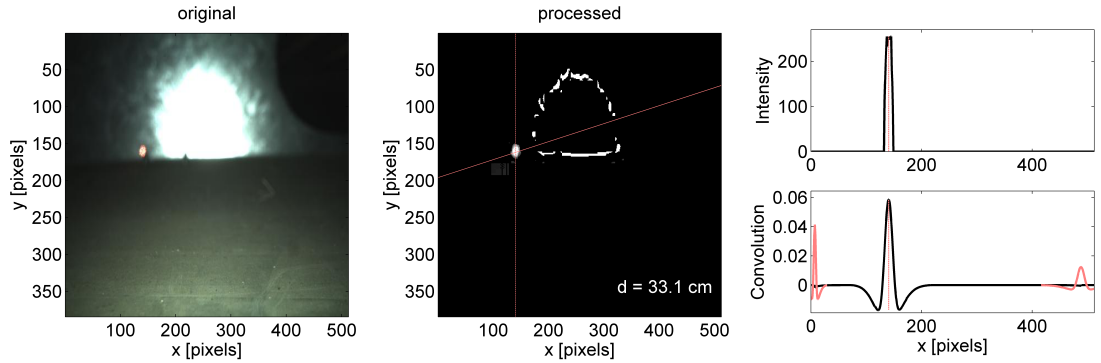

Figure 3.14: Laser detection using a convolution with a DOG of varying width, after selecting red lights in HSV space.

3.2.2.4 Calibration and results

Three sets of calibrations measures were done over the range 10 to 220 cm. We first adapted the detection line height and angle to pass through the laser image on the whole measuring range. We then tuned the parameters from the distance Equation 3.8 to find a good fit over the data. The obtained parameters are: $\alpha_{max} = 22°$, $\beta = 23.4°$ and $l = 8.3$ cm. After calibration, the achieved absolute distance errors between 10 and 100 cm are lower than 1 cm (Figure 3.15). The error then rises up to a maximum error of 15 cm at 220 cm. The derivative $\mathrm{d}d/\mathrm{d}p$ (Equation 3.9) is also shown on the figure. It gives the theoretical error in cm/pixels: for example an error of 1 pixel at a distance of 150 cm gives a bit less than 4 cm error. The theoretical error follows roughly the real error.

Figure 3.16 shows the differential measure of a cube with a side length of 60 mm. The distance is measured on the back surface (a, 37.14 cm) and on the front surface (b, 30.80 cm). The difference gives a size of the cube of 6.34 cm, which gives an error of 5.6%.

For comparison, the optoNCDT 1710-1000 laser triangulation sensor from Micro-Epsilon[3] has a resolution of 0.1 mm, with a range from 1 to 2 m. It has a smaller range, but a much better resolution. However, we do not need such resolution. Furthermore it has a size of 200x83x48 mm, which is too big to integrate on the robot.

This measuring system helps a lot for driving the robot with the camera view, as it helps to know the distances and put a scale on objects in unknown environments. With good tuning of the lighting LEDs intensity and camera exposure, it is possible to measure continuously the distance. For better laser detection it is better to switch the LEDs off and reduce the camera exposure before making the measurement.

One advantage of this sensor is that we see visually exactly where the measure is done. This is very helpful to make precise measurement, and allows to control if the measured distance is valid or not.

[3]Micro-Epsilon: `http://www.micro-epsilon.com`.

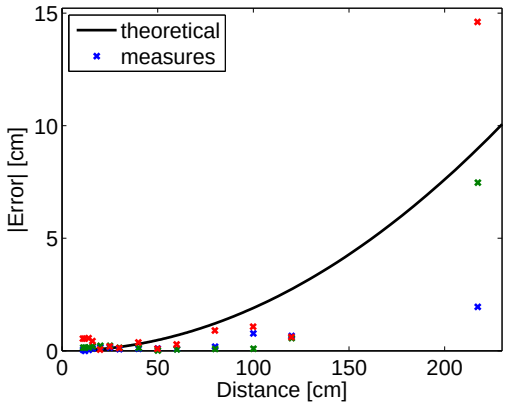

Figure 3.15: Absolute distance errors of the three calibrations measures (crosses), and dd/dp which gives the theoretical error in [cm/pixel].

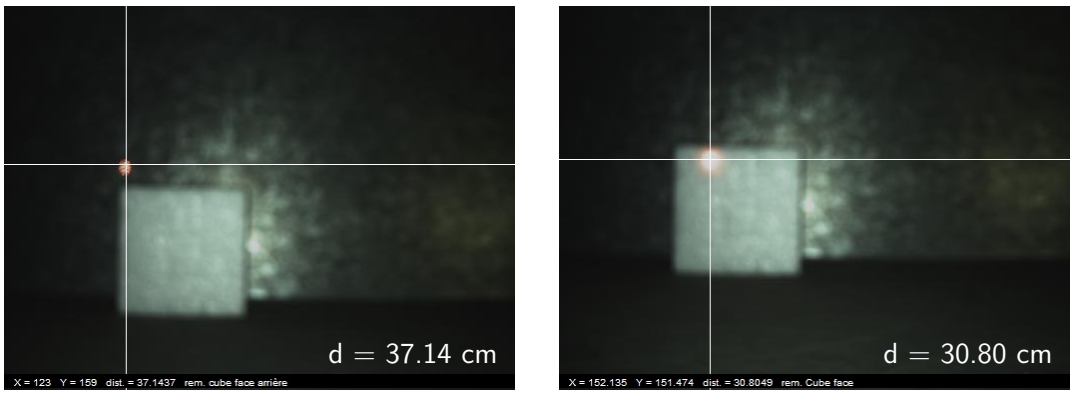

(a) (b)

Figure 3.16: Measuring the size of a 6 cm cube, by making the difference between the distance of the back surface and front surface: $37.14 - 30.80 = 6.34$ cm.

3.2.3 Inspection results

The live video feedback from the Cy-mag^{3D} II allows to inspect visually a structure where the robot can move, but it also allows to control the robot without viewing it. The Wifi transmission keeps the robot free of tethering cables, which keeps its mobility intact.

We tested the inspection capabilities of the Cy-mag^{3D} II in an air duct. Using the camera, the distance sensor, the accelerometers and the Hall sensors as feedback, we could drive the robot in the duct without viewing it. We achieved a trajectory of more than 16 m (Figure 3.17), passing two outer corners and inspecting some parts. Passing the external corners is difficult, as we do not see what is behind the corner. It also requires the use of the tail, which makes the control more difficult.

The achieved image transmission rate is of only 3 images per second, with a resolution of 512x384 pixels. This low data rate is due to the fact that the camera sends raw bayer color data (see Appendix A.3.4 for details). The processor has to convert this coding in YUV (luma and chrominance, see Appendix A.3.3 for details), and then compress it in JPEG before transmission, which requires computing power and time. Also due to drivers

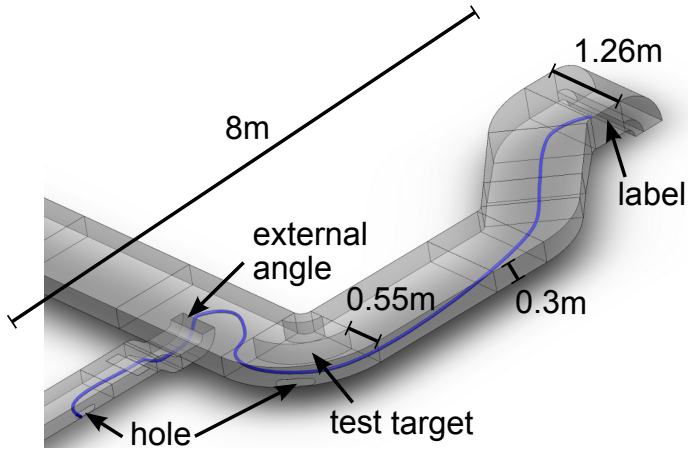

Figure 3.17: Trajectory of the robot in the ventilation. It reached a point 8 m away from the entrance and came back.

problems on the i.MX31, the video compression cannot currently be used.

A test target is used to measure the visual performances of the camera (Figure 3.18(a)). Figure 3.18(b) shows an image of the target taken in the test environment, at a distance of 125 mm. Details as small as 0.2 mm are visible, which gives an angular resolution of 0.1° (arctan(0.2/125)). This resolution could be theoretically increased by 4 by using the full resolution of the camera, as we subsample the image which has an original resolution of 2048 pixels on the width.

With our system, a good focused image is obtained only at a defined distance, as there is no auto-focus. This is a problem, as we must set the focus to the correct distance before the inspection. For example, if we set the focus at around 1 m, we will get sharp images of the general view, but we will not be able to view small details on close objects.

The LEDs are reflected on the glossy paper of the test target in the center of the image and decrease a lot the visibility in this zone. However, they are necessary in such dark environments (Figure 3.19). They allow to light objects up to 5 m away. The LEDs intensity and camera settings must be adjusted manually to obtain a good exposed image, depending on the conditions and on what part of the image is important.

Figure 3.20 shows a label present at the end of the trajectory executed in the ventilation duct. The label measure 12.7x70 mm, and the letters have an height of 2.5 mm. All the text is clearly visible and readable.

Controlling the robot using only the camera view is difficult. First it is difficult to evaluate the size of the objects in unknown environments. Secondly the low frame rate makes the feel of the dynamics of the robot difficult. Finally, the long exposure time required to get a well exposed image in a dark environment makes the images blurry when the robot moves and oscillates. One of the only solution to control the robot looking at sharp images is thus to move by small steps (10 cm for example), and look at the images during stops.

The distance sensor helps a lot in controlling the robot, as it allows to measure objects and get the scale of the environment. For example, on long flat surfaces, moving by 10 cm steps as described before takes a long time. Using the laser sensor, we can measure the distance to the next visible obstacle, and then move over this full distance, as we know there is nothing between the robot and the obstacle. We can thus move faster and inspect

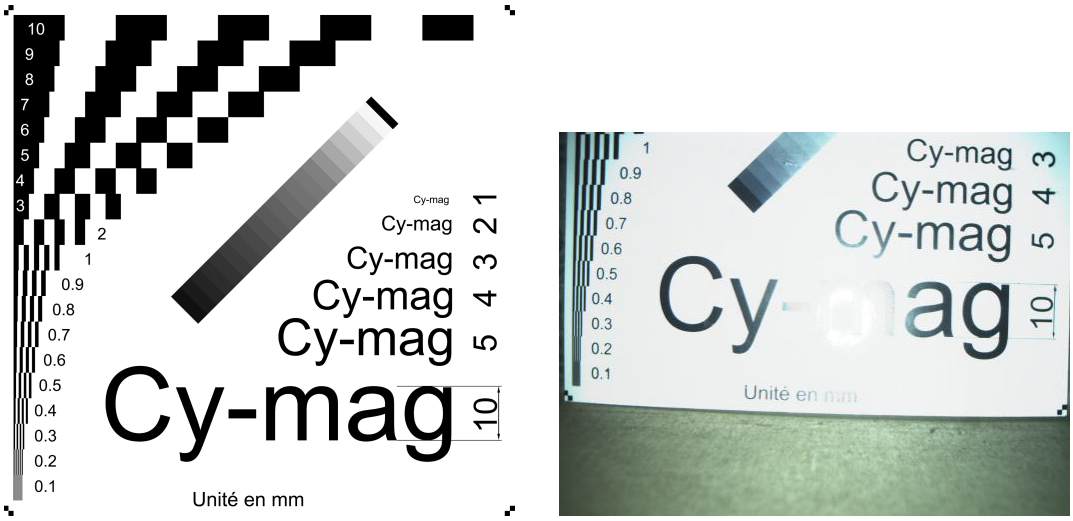

(a) (b)

Figure 3.18: (a) Original test target image (not to scale), and (b) image taken by the Cy-mag^{3D} II. 0.2 mm details are visible at a distance of 12.4 cm.

Figure 3.19: Cy-mag^{3D} II lighting the air duct.

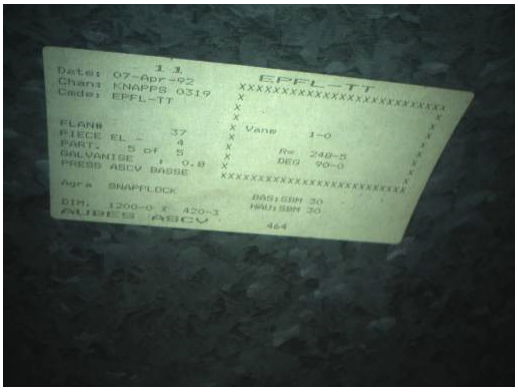

Figure 3.20: Label at the end of the ventilation duct. It measures 12.7x70 mm, and the letters have a height of 2.5 mm.

a bigger area in the same time.

A fisheye lens was also tested. It gives a much wider angle of view of 180° (Figure 3.21), compared to the previous 42°. This decreases the inspection capabilities, as one must be much closer of an object to see its details. As the viewing angle is bigger, the motion blur of the image due to the robot movement and oscillations is also smaller. It is thus easier to control the robot, as the operator has a view of almost everything in front of the robot, and the image is of better quality when the robot moves.

A solution to have both wide and narrow angle could be to use a fisheye lens and a numerical zoom. As the camera has 2048 pixels on the width, we can either subsample the image to get 512 pixels as we do now, or just use the 512 central pixels to zoom in. Using such cropping, the resulting viewing angle α_2 is obtained from the original viewing angle α_1, the number of pixels on the width P_w and the new number of pixels p_w by the following formula:

$$\alpha_2 = 2 \arctan\left(\frac{p_w}{P_w} \tan(\alpha_1/2)\right) \tag{3.18}$$

For example, with P_w=2048, p_w=512, and α_1=150°, we get α_2=87°.

The Wifi connection is working in the tested environment with no limitations up to 8 m. We did not test bigger distances to be sure we could recover the robot in case of problems.

3.2.4 Conclusions

A camera and a laser distance sensor were added to the Cy-mag^{3D} II to remote control it and to inspect the environment. Wireless transmission of the images and control commands is important to retain the robot's mobility, as a cable would limit its mobility, especially over long distances.

Inspection of details as small as 0.2 mm is possible with the used miniature camera. This resolution can be increased by 4 using the full resolution of the camera. An auto-focus would increase the usable range of the camera.

A laser triangulation distance sensor was developed and is especially useful to get a scale of the objects in unknown environments. This distance sensor is very compact, as we only need to add a laser to the system, the camera being used to sense the location of the laser dot. It achieves a precision below 1 cm for distances between 10 to 100 cm. The precision then rises up to 15 cm at 220 cm. To increase the measuring capabilities, a laser line can

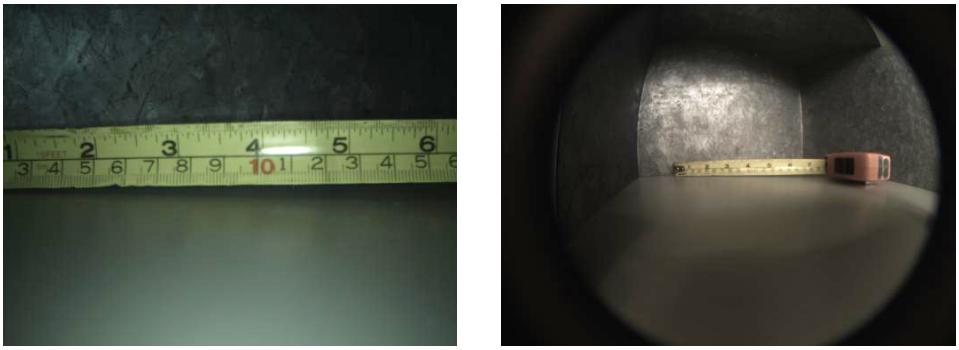

(a) 42° horizontal angle. (b) 180° horizontal angle.

Figure 3.21: View of the same scene using the standard (a) and the fisheye (b) objectives.

be used instead of the single beam. We would thus measure distances on the full vertical range of the camera [GCMD11]. However, the laser emitter could be bigger and may be more difficult to integrate on the robot.

Other sensors also increase the feedback from the robot and increase the control capabilities. As the environments may be very similar in all directions, it is sometimes difficult to know the orientation of the robot only by looking at the camera images. For example, in the air duct, we sometimes did not know whether we were on the bottom surface, on a wall or on the ceiling. The accelerometer is thus very useful to understand the orientation of the robot, and helps in the navigation and control. The Hall sensors allowed us to know the magnet's positions and adhesion status, which is very useful to drive the robot safely. Using all of these sensors, we were able to drive the robot over 8 m into an air duct and come back, passing external and internal angles, only using the user interface, without viewing the robot.

The size of the Cy-mag^{3D} II was designed to use the available mx31moboard electronics driving the camera and WiFi dongle. Using a smaller electronics for the camera and WiFi (as mentioned in Appendix A.1.2) would allow us to scale down the robot with no major problems: the magnetic system, mechanics and motors could easily be designed smaller, as shown in the first version of the Cy-mag^{3D}; the electronic boards of the wheels may be more difficult to scale down, as the chips and sensors components are of fixed size, but changing some design part would allow us to reduce the size enough.

3.3 Vision with the Tubulos

In Section 2.5 we described two different tube crawlers, using two different locomotion principles: the Tubulo I uses magnetic wheels, and the Tubulo II uses inch-worm movements with MSDs. Their aim is to inspect boiler tubes, they thus embed a camera, and transmit the images to the user using a SerDes. Details about the electronics and inspection results are showed in the next sections.

3.3.1 Electronics

There is not enough space on the Tubulo I or II to put a big camera, as the tubes have a diameter of 25 mm, and the modules have cross section of less than 18 mm. We thus use the small Pixelplus camera (Section 3.1.1), which fits well in both robots.

We also do not have enough space to embed a powerful processor to manage the camera. Furthermore wireless transmission of data in tubes is difficult and requires specifically designed electronics and antennas (Section 3.1.4.1). We thus decided to transmit the camera images to a computer using cables, without processing them on board. A SerDes system is used to transmit the digital images over a twisted pair of cables (Section 3.1.3). It has the advantage of needing only two cables, which are thus light and flexible. The transmission length is around 10 m, and can be increased up to 20 m using an additional signal conditioning chip.

Lighting LEDs are needed in the dark environments like tubes. Two LEDs are placed on the side of the camera (Figure 3.22). We use LEDs of 3 mm diameter, with a beam angle of 37° and a luminosity of 10'000 mcd. They consume 20 mA at 3.2 V (64 mW).

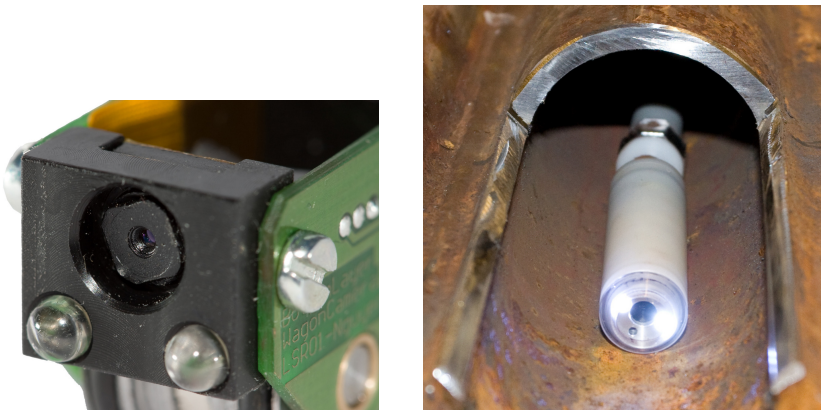

(a) (b)

Figure 3.22: Tubulo 1 (a) and 2 (b) camera and lighting LEDs.

3.3.2 Results

The SerDes can transmit 640x480 pixels images from the camera at a frame rate of 15 images/s over 10 m. It gives a good fluid view of the tube.

The LEDs are sufficient to get a good lighting in ⌀25 mm tubes. They allow viewing up to 20 cm in front of the robot, which is sufficient for inspection.

A test pattern with stripes of different width (Figure 3.23(a)) is rolled in the tube and used to test the camera performances. Details as small as 0.1 mm are visible at a distance of 30 mm, which is an angular resolution of 0.2° (Figure 3.23(b)).

An image taken by the Tubulo in a new 25 mm steel tube is shown in Figure 3.24(a). As the tube is new, no features can be seen except the dark longitudinal soldering at the bottom.

Tests in old ⌀50 mm water wall tubes were done with the Tubulo II. The robot is not centered in the tube but sticks on one side of it. In this case the tube is too big to get a good lighting (Figure 3.24(b)), and we see only one side of the tube. Some corrosion and dust is visible on the image.

3.3.3 Conclusions

A miniature camera is installed on both Tubulos to inspect the tubes they move in. Due to size limitations on the robot, we decided to transmit the images using cables. A SerDes electronics allows for reducing the number of cables between the camera and the computer from 10 to two. This allows digital transmission of the images with a light and flexible twisted pair of cables, which does not disturb the mobility of the robot significantly. However, the range with the current system is limited to 10 m, which is too short for real waterwall tubes that measure up to 50 m. Using better quality cables and an additional driver should allow us to transmit up to 100 m. However, a shielded cable will be heavier and stiffer than the current one, which will reduce the mobility of the robot.

Two LEDs are used to light the tubes, and allow a clear vision over 20 cm. The camera can detect details as small as 0.1 mm.

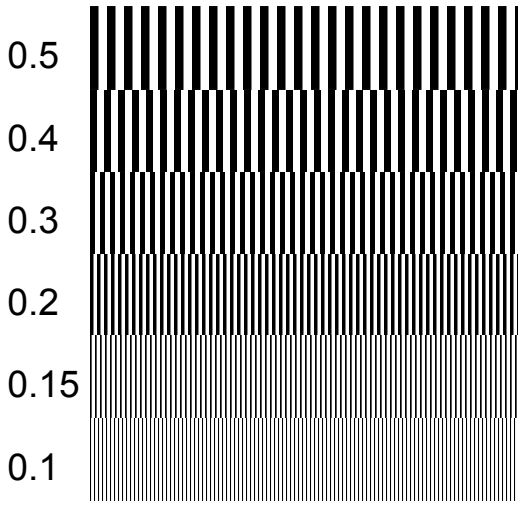

(a) Part of the test target (not to scale) rolled in the ⌀ 25 mm tube, with the stripes spacing in mm.

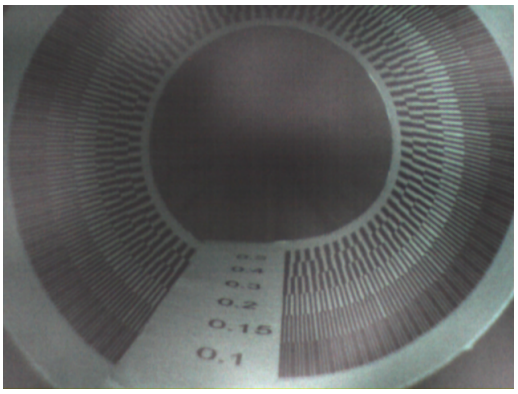

(b) View of a test target in a tube. 0.1 mm details are visible at a distance of 30 mm.

Figure 3.23: Tubulo camera test target.

(a) New ⌀ 25 mm steel tube.

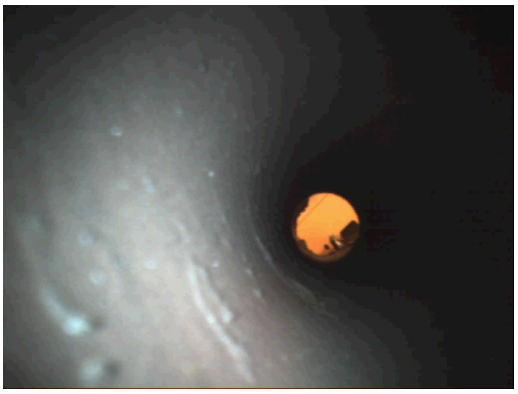

(b) Used ⌀ 50 mm water wall tube.

Figure 3.24: Images taken by the tubulo robot.

3.4 General conclusions on vision

Vision is required for inspection robots. First, it allows for visually inspecting the structures the robot moves on. The general state of the structure can be checked, and visible defects as small as 0.1 mm can be detected using miniature digital cameras. Secondly, vision is required if the robot gets out of sight from the operator. This allows the operator to control the robot by having access to the point of view of the robot.

A camera is the most useful sensor for remote controlling a robot; however, other sensors can increase the controllability substantially by giving more information about the environment and the state of the robot. Using only camera images, it is very difficult to know the scale of the objects in unknown environments. A distance sensor has been shown to be very useful to measure objects and the environment. As the environment may be very structured, the camera images do not give information about the orientation of the

robot. We cannot distinguish the bottom from the ceiling in an air duct, for example. An accelerometer is thus very useful in this case. Finally, the camera does not detect non-ferromagnetic surfaces. Hall sensors that allow for measuring the adhesion force are thus very useful to drive the robot safely, giving the possibility to stop the robot before it falls. They also allows us to know the position of the magnetic systems of the Cy-mag^{3D} II, which helps to control the robot in difficult phases such as obstacle passing. The integration of all of these sensors in addition to the camera is therefore a key aspect of the safe and efficient deployment of this new type of robot.

4 Advanced Inspection Methods

4.1 Introduction

Visual inspection is often not sufficient to control the state of parts or structures. Cracks, holes and other defects can be located inside the material, on the hidden side of the inspected part or too small, and can thus not be detected visually. To detect such defects, other Non-Destructive Testing (NDT) methods than vision are required (see Section 1.5.2, page 13, for details).

Most non-visual NDT methods are difficult to miniaturize and integrate on mobile robots. Some of them require high energy that is not suitable for use on mobile systems. Methods such as ultrasonic testing also require a liquid couplant between the probe and the part, which is difficult to embed. Most magnetic methods use electromagnets for magnetization, which also require a lot of energy. These electromagnets can be replaced by permanent magnets when the flux does not need to oscillate. This gives a strong energy consumption advantage. Eddy current testing requires a relatively small amount of power. It is quite easy to use, as the probe just needs to be moved on the part in order to inspect it. However, the probe position must stay stable during the scanning; otherwise it creates changes in the output signal that make the detection of defects very difficult. Magnetic Particle Inspection (MPI) has the advantage of inspecting a whole surface, contrary to most other NDT techniques where a probe, inspecting a single point, must scan the whole surface. Another advantage is that the required magnetization can be done with permanent magnets. However, this requires an inspection liquid, which is more difficult to integrate on a robot.

In this chapter, an Eddy current sensor is mounted on the Tripillar II. We run tests to detect cracks on a test block, and we illustrate the limitations of this system. A MPI system is then designed to extend the inspection capabilities to larger surfaces. Its aim is to inspect turbine blades without disassembling the rotor from the stator. The magnetic force is created by an MSD, which does not consume energy for magnetization. Tests done on a test block and on a turbine blade validate the system.

4.2 Eddy current inspection with the Tripillar II

Eddy current sensors allow to detect defects near the surface. Cracks, corrosion and thinning are the most usual defects detected by Eddy current sensors. These sensors are usually held by inspectors, or pushed through tubes using endoscopes. A climbing robot embedding such a sensor can inspect places that cannot be inspected using standard

methods.

We mounted an Eddy current sensor on the Tripillar II. The next sections show the sensor description and the tests done with this system.

4.2.1 Design

An Eddy current sensor developed at the Laboratory of Microsystems at EPFL (now sold by the Sensima spin-off[1]) is mounted on the Tripillar II (Figure 4.1(a)). It is fixed on the robot with a flexible blade, which acts as a spring pushing the sensor on the surface. This sensor generates Eddy currents in the material using a coil of 4 mm diameter driven by an alternating current. A resonant circuit creates the alternating current (Figure 4.2), with a frequency w_0 depending on the resistance R, the impedance L and the capacitance C:

$$w_0 = \sqrt{\frac{1}{LC}} \tag{4.1}$$

Changes in the material will change the induced Eddy currents and thus change the impedance L of the coil. As L depends on the material, the frequency will vary accordingly. Monitoring the frequency allows thus to detect changes in the material, as cracks for example.

4.2.2 Results

We performed an example of inspection on a test block, having three cracks of around 150 μm width, and 1, 2 and 3 mm depth (Figure 4.1(b)). The frequency output of the sensor moved over the block by the robot is shown in Figure 4.3. The changes in frequency allow to detect the 3 cracks clearly. This sensor does not measure the depth of the cracks, however the depth can be estimated by comparing the signal with known cracks.

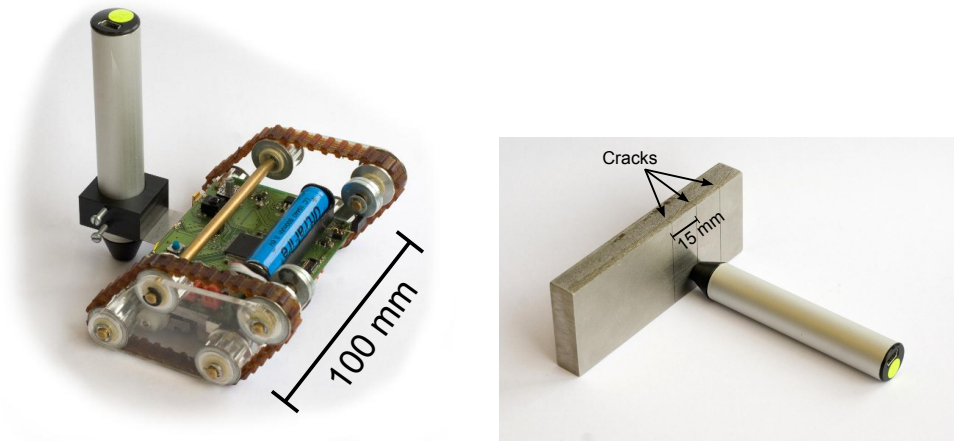

(a) (b)

Figure 4.1: (a) Tripillar II carrying an Eddy current sensor and (b) Eddy current sensor on the test block.

[1]Sensima inspection Eddy current Compact Tester:
`http://www.sensimainsp.com/DataSheetECTesters.html`.

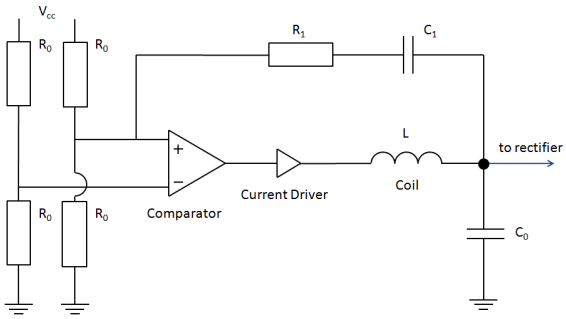

Figure 4.2: Resonant circuit used to drive the coil. The frequency depends on R, L and C. As L varies depending on the material at proximity, the frequency changes accordingly (source: Sensima).

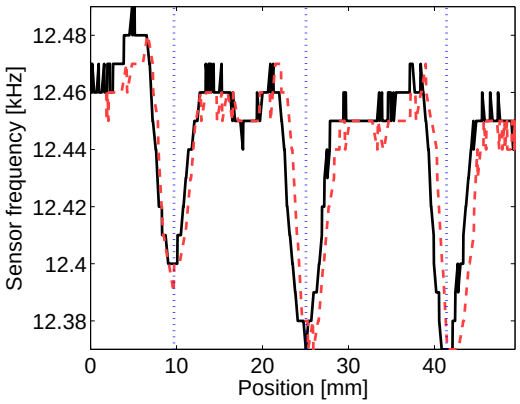

Figure 4.3: Sensor output depending on the position of the robot. The 3 cracks are clearly visible.

The robot moved over the cracks (plain curve) and came back (dashed curve). The position is computed from the motor encoders, which allows a good precision on straight movements, as there is almost no slippage in this case. The real distance of 15 mm between the cracks is confirmed on the graph, with a distance of 15.3 and 16.3 mm between the first two and the last two cracks.

4.2.3 Conclusion

The Eddy current sensor mounted on the Tripillar II shows good performances on a small test block. The sensor is mechanically stable enough to generate a stable signal and the cracks are well detected.

To inspect the full surface of a part and build an inspection map, a precise positioning system is needed. Odometry using only the motor encoders information is not precise enough, as the caterpillars need to slip when turning, and the error of this positioning method will rise very quickly. Exteroceptive sensors are thus needed to allow absolute measures of the environment. Precise distance sensors placed on the robot, or a camera filming it from above could be used for example.

The present sensor position is not optimal to perform inspections. The sensor moves a lot laterally when the robot turns, and the robot mobility is disturbed, as it cannot pass inner angles with the attached sensor. This could be improved by placing the sensor at a more central position on the robot, which requires a better integration of the sensor to the system. The casing and electronics shape, currently designed to be held by hand, can be changed to fit the available space on the robot. The electronic circuit can be simplified to drive the sensor directly from the microcontroller embedded on the robot.

Sensima is developing methods to measure the depth of the cracks with the Eddy current sensor. An array of Hall sensors placed in the coil should give the required information about the magnetic flux around the crack to compute its depth.

With the future developments of the sensor, and a good integration on the robot, this inspection system has the potential to access and inspect remote places that are not reachable currently.

4.3 Magnetic particle inspection system

While Eddy current sensors require a long scanning of the surface to perform a full inspection, MPI can inspect a surface in one go and is faster. Based on tests done at Alstom and based on inspectors' experience, MPI is even one of the only inspection methods giving good results on eroded parts of some turbine blades. These blades are disassembled from the rotor and inspected on a regular time basis (about every three years of operation). However, disassembling a big turbine is a complex operation and takes time. Indeed, it takes around one month (700 man-hour) to disassemble, inspect and reassemble a full turbine. A system able to perform an inspection on the assembled turbine would reduce the total inspection time and thus the costs.

The turbine blades we focus on are of the type ND41A (Figure 4.4). A steam turgine's last stage consists of 51 blades of this type (Figure 4.5). The blades are 1050 mm long, have a width of 300 mm at the base and 200 mm at the end. The turbine diameter at the blade platforms is 1656 mm and the diameter including the blades is 3755 mm. The angle between the blades is 7.06°, and the minimum distance between two blades is around 50 mm. Measured on a 3D model of the blades, the smallest concave (inner) curvature is around 70 mm radius, and the smallest convex (outer) curvature is around 50 mm. The blades are manufactured of ferromagnetic steel. Most of the cracks occur perpendicular to the leading edge (a 30 mm-wide band), and at the base of the blade. Cracks as small

Figure 4.4: ND41A turbine blade. It is 1050 mm long, has a width of 300 mm at the base and 200 mm at the end. It has surface curvatures with radius as small as of 50 mm near the edges. The typical eroded area on the leading edge is shown in green.

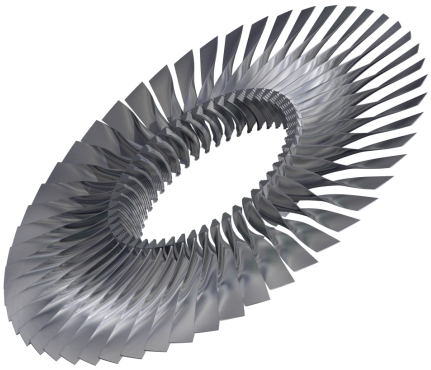

Figure 4.5: Turbine full stage CAD view. It has an internal diameter of 1656 mm, and an external diameter of 3755 mm.

as 1 mm in length must be detected.

The next section will explain MPI in more detail. The design of the system will then be described and the results of inspection tests will be shown.

4.3.1 Magnetic particle inspection

Magnetic Particle Inspection (MPI) is based on the Magnetic Flux Leakage (MFL) inspection method (see Section 1.5.2.4, page 18, for details). The part to be inspected is magnetized, and magnetic particles are dispersed on it. They will gather on places where the magnetic field is stronger, which corresponds to cracks and other defects locations. Fluorescent particles and UV lighting are used to increase the viewing contrast.

An MPI inspection is done by completing the following stages:

1. Clean
2. Demagnetize
3. Spray magnetic particles
4. Magnetize
5. Look for cracks under UV light
6. Demagnetize

The magnetic particles have a typical size ranging from 0.1 to 10 μm. The magnetization can be done with an electromagnetic yoke (Figure 4.6(a)). It creates a magnetic field between its two legs at the electrical network frequency (50/60 Hz). It requires an electrical connection (220 V, 50 Hz), and it is too big to make the in-situ inspection of the blades. Permanent magnet yokes are also available (Figure 4.6(b)), but they are difficult to handle due to the strong adhesion force, and too big for the turbine inspection. Automatic systems using bigger magnetization coils also exist.

One advantage of the alternative fields when using electromagnets is that they improve the sensitivity, by making the particles more mobile. The sensitivity is also improved by magnetizing during a longer period, even with static fields.

Semi-automatic MPI inspection is done at Alstom using a system capable of demagnetizing, magnetizing and spraying magnetic particles (Figure 4.7). The visual inspection is then done by an inspector.

Details and norms of MPI are described in the document ASTM E1444-05 [Int05].

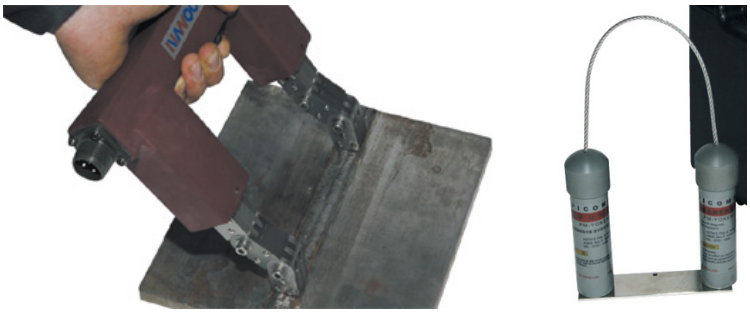

(a) Coil yoke.

(b) Permanent magnets yoke.

Figure 4.6: Two portable yokes from nawoo (`http://www.nawoo.com`).

Figure 4.7: Automatic MPI machine at Alstom. Only the final visual inspection is done by the operator.

The norms specify a minimum field or forces for the inspection systems. For standard electromagnetic yokes, the norm requires a minimum tangential field of 30e-4 T:

> "Tangential-field strengths shall have a minimum value of 30 Gauss (30 x 10-4 Tesla [T]) when measured at the part surface using a Hall effect probe gaussmeter as described in Appendix X4. Ensure that adequate field strengths are present in the areas of the part to be examined."

For permanent magnet yokes, a minimum lifting force is required, depending on the legs distance. In our case, we need at least 4.5 kg with spacing between 50 to 150 mm between the legs:

> "Alternating current and permanent magnet yokes shall have a lifting force of at least 10 lb [4.5 kg], with a 2- to 6-in. [50- to 150-mm] spacing between legs. Direct current yokes shall have a lifting force of at least 30 lb [13.5 kg], with a 2- to 4-in. [50- to 100-mm] spacing between legs, or 50 lb [22.5 kg], with a 4- to 6-in. [100- to 150-mm] spacing."

Test parts are used to test MPI systems. We use a test block measuring 142x50x33 mm,

containing 5 different cracks of known length (Figure 4.8). Detecting the cracks on this block allows to control the inspection capabilities of a system.

4.3.2 System design

With the goal to inspect turbine blades in situ, an MPI system is designed. As it is not known in advance if each required function will be functional, the design of the system is done progressively in a modular way, so that each module can be added or removed easily. The different modules can thus be tested and modified if needed.

Before describing all the subparts, the final system is shown in Figure 4.9. It shows a complete view of the system with its different components, which are: the MSD, the MSD actuation, the locomotion module, the liquid dispersion, the UV lighting, the camera, the electronics and the control. Those will be detailed in the next sections.

Figure 4.8: Test block (142x50x33 mm) containing 5 main cracks (P1-P5) from 2 to 14 mm long.

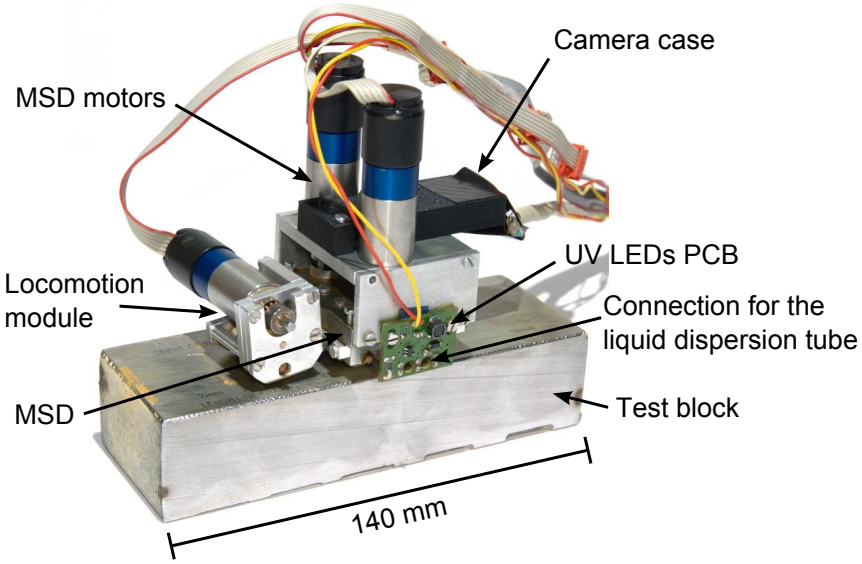

Figure 4.9: Full MPI system placed on the test block.

4.3.2.1 MSD design

Magnetizing the part is the core operation to perform MPI. Magnetization will create attraction forces around cracks and defects, which will attract the particles and make the defects visible.

To reduce the energy consumption of the system, the choice is made to magnetize the part using permanent magnets. Magnetic Switchable Device (MSD) are used for two main reasons: an MSD allows to remove the system with a small force which makes the operation easier; an MSD allows to change the magnetization direction, which will be used to demagnetize the inspected part.

A specific MSD was thus designed for this application, which we will call MSDI1, as Magnetic Switchable Device for Inspection 1[2]. It has a central hole used for visualization of the inspected surface, and two magnets.

Its working principle and geometry is different from the classic MSD (described in Section 2.1.2, page 23). In the off state, the magnetic flux follows a circular circuit inside the structure (Figure 4.10). To change to the on state, one magnet is rotated by 180°, the magnetic flux then goes off-plane and creates an adhesion force of up to 12 kg to any ferromagnetic part near the contact feet.

MPI tests were done on a test block and on a cracked turbine blade. The MSDI1 is used to magnetize the part, liquid containing the ferromagnetic particles is then applied. The cracks are observed under UV light. Based on the feedback of expert inspectors, the cracks are detectable with the same visibility as with standard yokes (Figure 4.11). The difference is that the inspected area is much smaller using this system: only 80 mm^2 compared to the 7100 mm^2 of the whole part using a hand yoke (as shown in Figure 4.6(a)). The MSDI1 still works with an air gap up to 2 mm.

Based on these good results, I designed a bigger MSD to increase the inspection surface, the MSDI2 (Figure 4.12(a)). The viewing window measures 20x20 mm, which makes a surface 3.6 times bigger than MSDI1. This allows to inspect bigger surfaces and thus to inspect faster.

The working principle is the same as MSDI1, but two magnets are placed on each side to increase the magnetic potential. Only one magnet of each side needs to be actuated, as the other one follows its rotation thanks to the magnetic flux. The adhesion force is of 11 kg, which is enough with regards to the norms (4.5 kg).

The MSDI2 is mounted on a wheeled structure, which can roll on surfaces (Figure 4.12(b)). The air gap can be adjusted between 0 to 4 mm using screws. An air gap is needed when moving on convex surfaces, to prevent the feet from touching the surface.

The feet are distinct parts, separated from the top part, and are fixed using screws. This allows to change them easily, to adapt to the different possible curvatures (Figure 4.13).

Magnetic simulations

Magnetic simulations are done to ensure the required performances and to optimize the design of the system. They allow to estimate the adhesion force and the magnetic fields, and to improve them by modifying iteratively the design. They were performed using the program Comsol.

The magnetic field on the surface of an inspected part is shown in Figure 4.14(a). A field of 200 A/m is achieved in the middle of the inspected surface, which corresponds to the specifications for electromagnetic magnetization in MPI norms. The norms also

[2]The MSDI1 was developed by Frédéric Rochat in his PhD [Roc11].

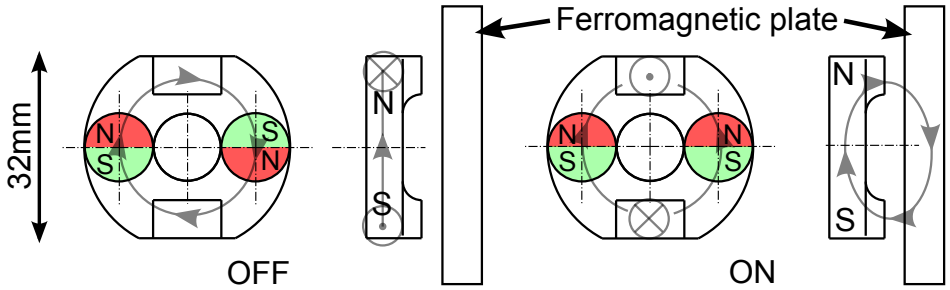

Figure 4.10: MSDI1 drawings and concept.

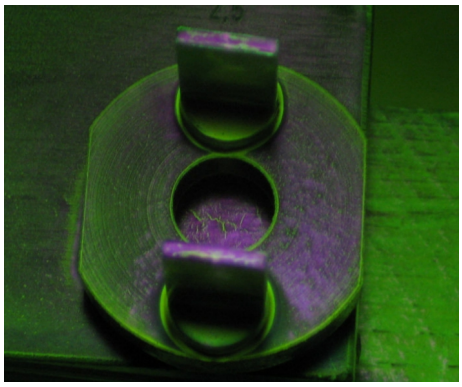

Figure 4.11: MSDI1 and a crack on the test block.

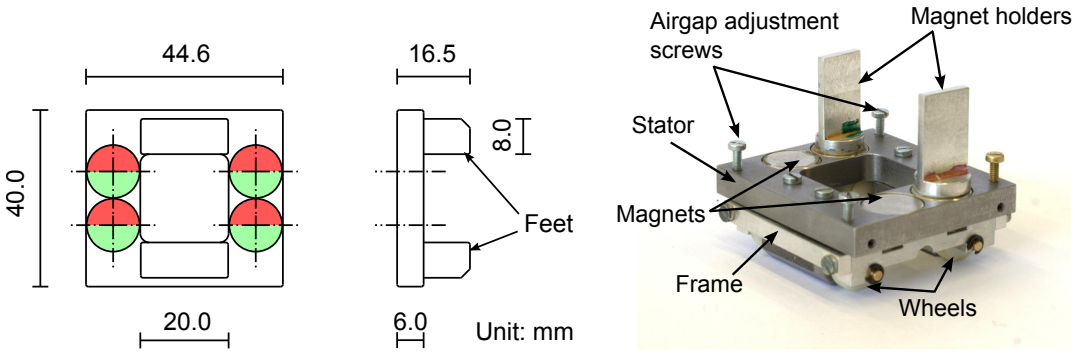

(a) (b)

Figure 4.12: (a) MSDI2 drawings, showing the exchangeable feet, and (b) picture with the supporting wheels and the screws to adjust the air gap.

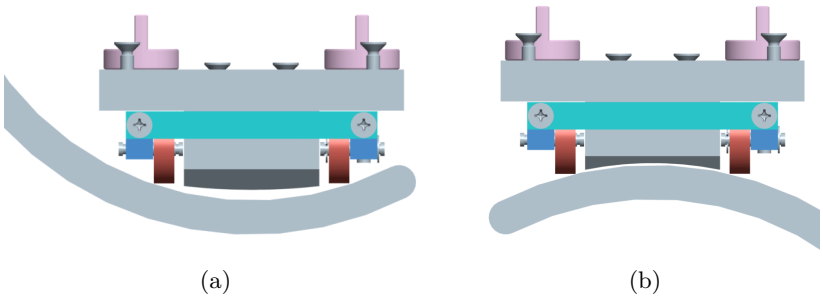

(a) (b)

Figure 4.13: MSDI concave (a) and convex (b) surface adaptation.

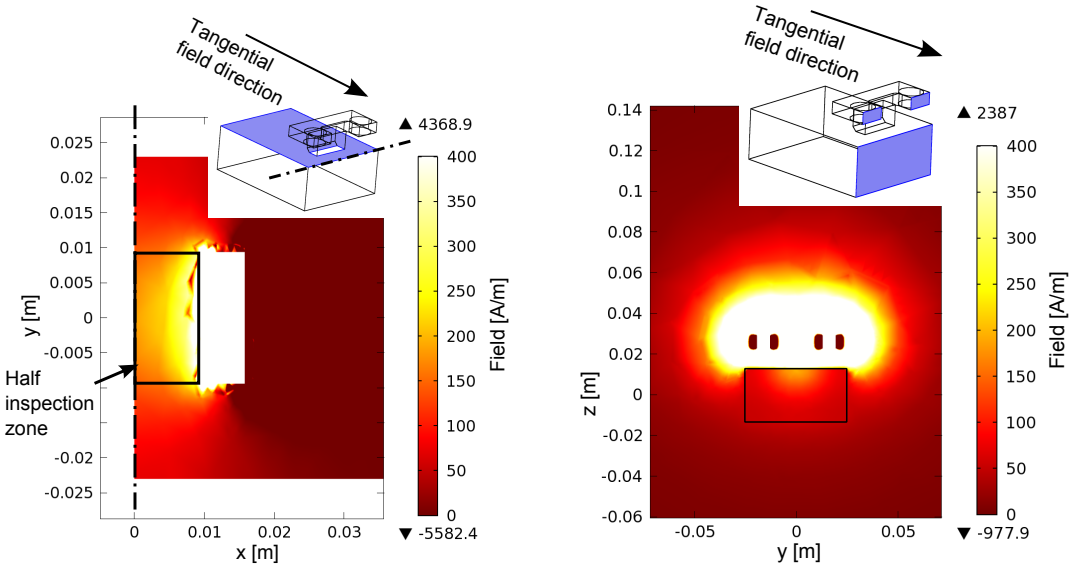

(a) (b)

Figure 4.14: MSDI2 magnetic simulations. Field [A/m] on (a) the top surface and (b) a cross section between the feet of the MSDI2.

specify a minimal adhesion force for magnetization using magnets of 4.5 kg, for a spacing of 50 to 150 mm between the feet.

Figure 4.14(b) shows magnetic field in a cut view of the system and inspected part. The field at a depth of 10 mm within the inspected part is still around 150 A/m.

The angular positions of the magnets define the magnetization intensity. Figure 4.15 shows the simulated tangential field on the test part, depending on the magnets angular positions. We see that the intensity of the field can be chosen between the positive and the negative maximums.

This is useful for demagnetization, as a decaying alternating field is needed. It can be achieved by a rotation sequence of the magnets, alternating the flux direction, and decaying the maximum rotation angle (Figure 4.16).

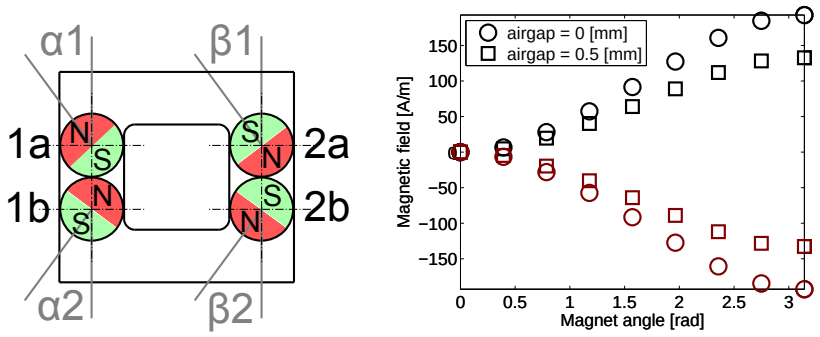

(a) (b)

Figure 4.15: Simulated tangential magnetic field (b) on the test block depending on the angle of the magnets (a). Black dots correspond to $\beta 1$=0 with $\alpha 1$ varying ($\alpha 1 = \alpha 2$), and red dots correspond to $\alpha 1$=0 with $\beta 1$ varying ($\beta 1 = \beta 2$).

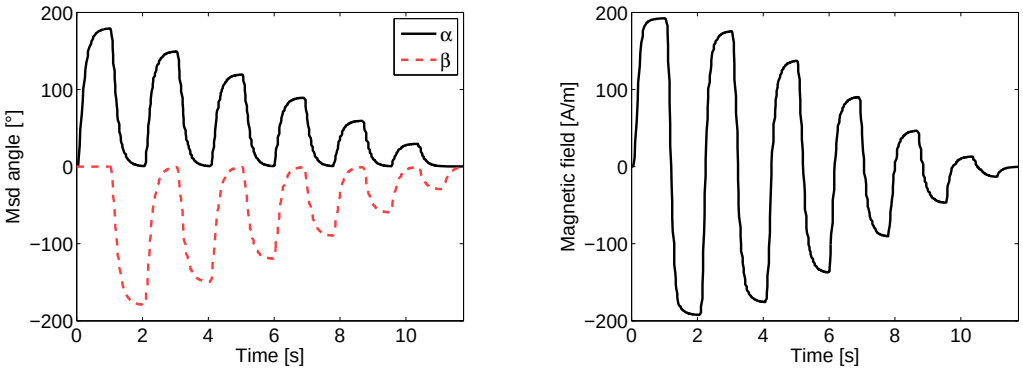

(a) Magnets angular position (defined in Figure 4.15(a)).

(b) Resulting simulated field on the inspected part.

Figure 4.16: Demagnetization sequence.

Simulations validation

The simulations are validated by comparing the simulated forces with the measured ones (Figure 4.17). In both cases, there is an air gap of 0.5 mm, and one magnet is rotated between 0 and 180°. The real force is lower of around 17% than the expected simulated one. This variation can be caused by different factors, such as small air gap variations, magnet properties or steel quality.

With this air gap, the maximum force is only 2.7 kg, which is not enough according to the norms. The MSDI2 must thus be used with very thin air gaps, between 0.0 to 0.2 mm.

The MSDI2 is tested on the test block and shows good inspection results. According to inspection experts, the cracks are detected with a good visibility, and the inspection surface is bigger than with MSDI1.

4.3.2.2 MSD actuation module

Figure 4.18 shows the magnets actuation module. Two motors rotate one magnet on each side of the MSD. The other magnets rotate freely thanks to the magnetic flux, and self

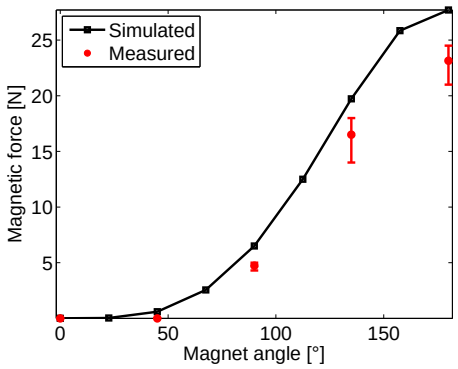

Figure 4.17: Simulated and measured magnetic force depending on the magnets angles ($0 < \alpha < 180°$, $\beta = 0$), for an air gap of 0.5 mm. 8 measures were done for each magnet angle: the mean, minimum and maximum are indicated.

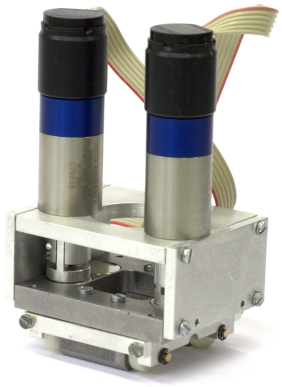

Figure 4.18: Magnets actuation module mounted on the MSDI2.

align with the motorized ones, so there is no need to control them. The module can be fixed on top of the MSDI2 using screws.

The measured torque to rotate the magnets is 67 mNm. A Faulhaber 1717 motor with a 159 reduction stage is used. It gives a usable output torque of 190 mNm, which makes a sufficient security factor of 2.8. Encoders allow to measure the rotation of the motors precisely. The reference zero position must be set manually.

The achieved maximum rotation speed of the magnets is of 1.5 Hz. This could be increased by using more powerful motors.

4.3.2.3 Locomotion

Moving over the part is important for the system, as in its static configuration it allows only to inspect a small surface. The system has been equipped with an active locomotion, making an automated inspection possible. The propulsion of the system is done using a magnetic wheel driven by a motor (Figure 4.19). The module is fixed to the MSD with flexible blades, acting as a suspension to adapt to the surface.

The magnetic wheel has a central cylindrical magnet with a flux guide on each side.

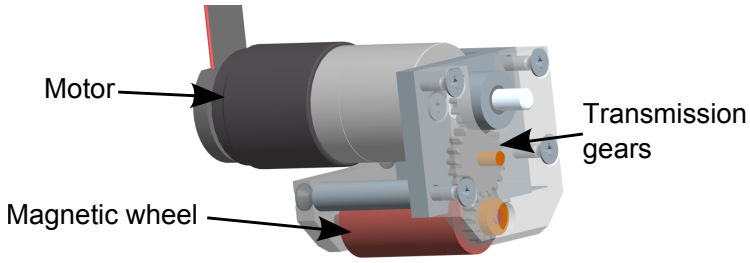

Figure 4.19: CAD view of the propulsion module.

This wheel has the same design that was used for the magnetic flux monitoring tests (Section 2.2.3, page 28). It has a diameter of 10 mm and a width of 20 mm. Its adhesion force is of 3.5 kg.

The full MPI system weighs around 300 g. The minimum required force to push the system on a vertical surface is thus of 3 N. A Faulhaber 1717 motor with a 246 reduction stage is used. It gives a usable output torque of 295 mNm. With the given geometry, this is largely sufficient for this application.

A motor control electronics module controls the motor precisely (see Appendix A.1.3 for details). The maximum torque of the motor makes the wheel slip on the surface during acceleration. The torque is thus limited to prevent slippage, which allows to measure the traveled distance with the encoder. A maximum speed of 20 mm/s is achieved.

4.3.2.4 Liquid dispersion

A liquid dispersion system is required to make the magnetic particles contained in the liquid flow over the inspected part. After doing some experiments, we concluded that the best way to disperse the fluid was to let it flow smoothly out of a tube on the inspected part, between the feet of the MSDI2. If the liquid is dispersed in front of the MSDI2, it creates a drag when we roll over it. If we disperse it too fast, the liquid and the particles do not stay in the inspection area and are “washed away”.

To adapt this distribution system on the MPI system, we place the distribution tube between the LEDs, as close to the surface as possible. The liquid is driven by a pump placed near the liquid tank.

The pump is a Kavan electric pump, it has a maximum input voltage of 12 V and a maximum flow of 30 ml/s (Figure 4.20). The central control can regulate the pump voltage and thus the liquid flow.

The inspection liquid is stored in a 10 l container. The part to inspect is placed in a bigger container, collecting the inspection liquid during the inspection.

On the existing prototype, the control of the flow of the liquid is made in open loop. No flow measurement is available on this system. A closed-loop speed controller would help to get a finer control of the flow, as the voltage needed to start the pump varies. We thus drive the pump with a high voltage to start the pump, and then decrease the voltage to get a slow flow.

4.3.2.5 UV Lighting

UV lighting is needed to see the fluorescent particles. Small UV leds can be used for this, as the room to put the lighting is small.

The cylindrical LEDs from VioLed (5C90) have a wide viewing angle of 90°, and thus produce a quite uniform illumination (Figure 4.21(a)). Their peak wavelength is centered at 365 nm, and have an optical power of up to 4 mW. Three LEDs can be placed on each side of the viewing window, at the bottom.

Stronger and smaller LEDs were found (X-365-30) that produce up to 6 mW of optical power. However, their field is more directional and it creates a heterogeneous intensity over the inspected surface, which makes the cracks visualization more difficult.

An LED driver (LM3410) is used to generate the sufficient voltage and to control the current passing through the LEDs (20-25 mA).

The optimal position of the LEDs is a compromise between the achieved contrast and the unwanted reflections: if the LEDs are directed too much toward the surface, reflections directed to the camera occur and reduce the visibility around these spots (Figure 4.21(b)); if the LEDs are parallel to the surface, the contrast is not sufficient. The chosen compromise was to place them on the sides, slightly inclined toward the surface (around 10°), avoiding reflections in the middle area.

Figure 4.20: Kavan electric pump used to disperse the liquid containing the magnetic particles. It has a maximum flow of 1.8 l/min, and a size of 73x46x60 mm.

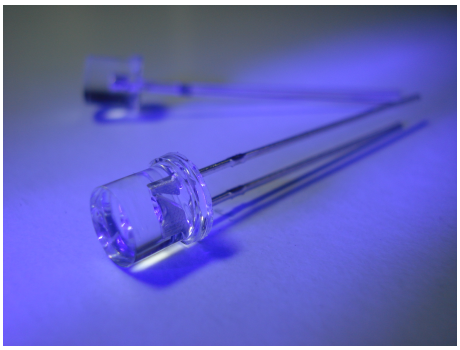

(a) UV cylindrical LEDs (⌀5 mm) from VioLed.

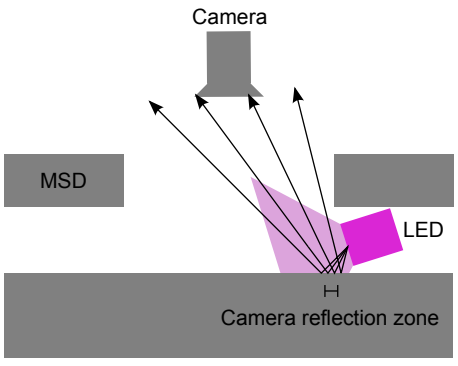

(b) LEDs positions and light reflection.

Figure 4.21: UV Lighting.

4.3.2.6 Camera

When introducing the inspection system in a turbine, a camera is needed to take an image of the inspection zone between the feet of the MSDI2.

Three different cameras are compared and tested (Table 4.1 for details). The PixelPlus camera has the advantage of being compact, but has a small sensor, which reduces the sensitivity, and has an average resolution (640x480 pixels, Figure 4.22(a)). A SerDes electronics is available for this camera, which allows a cable range of at least 10 m (see Section 3.1.3, page 74, for details). The Digimicro camera is a miniature microscope, with an adjustable magnification between 10 and 200 times. It has a good resolution (1600x1200 pixels), but is big (Figure 4.22(b)). The quickcam from Logitech has a good resolution (1600x1200 pixels) and has an autofocus, but is also quite big (Figure 4.22(c)). The camera used on the Cy-mag^{3D} II was excluded because of the size of the electronics.

The camera tests were done with the magnetic system with no air gap. We inspected the cracks on the test block (Figure 4.8).

The results with the PixelPlus camera are a bit disappointing (Figure 4.23(a)). The sensitivity seems too small to get a good image quality with low level lights.

The Digimicro camera is showing very good results (Figure 4.23(b)). The cracks are visible and very detailed. The problem with this camera is that it is quite big, and has a magnification of 10x. It must thus be placed quite far to get a full view of the window area (3-4 cm).

The Logitech webcam gives good results. It is a bit less sharp than the Digimicro (Figure 4.23(c)). It has an autofocus, which works well when we approach it slowly close

Table 4.1: Camera comparisons

	PixelPlus	**Digimicro**	**Logitech**
Size [mm]	33x12x4 (with serializer electronics)	⌀33x110	90x45x30
Resolution [pixels]	640x480	1600x1200	1600x1200
Sensitivity [V/Lux-sec]	1.46	-	-
Autofocus	no	no	yes
Magnification	1x	10-200x	1x
Transmission protocol	SerDes	USB	USB
Cable maximum range [m]	10	5	5

(a) PixelPlus (b) Digimicro (c) Quickcam

Figure 4.22: The 3 tested cameras.

(a) PixelPlus (b) Digimicro (c) Quickcam

Figure 4.23: Images of P3 for the 3 different cameras. The MSDI2 is placed with no air gap.

to the surface. It is thus easier to use than the two other cameras, which have a manual focus that can be difficult to set correctly. However, this camera is also too big to fit in the system.

Mainly because of its small size, the PixelPlus camera is chosen for the system.

To measure the length of the cracks found on the images, we use the fact that we know the distance between the two feet, which is of 20 mm. We can thus calibrate the image by getting a pixels/mm ratio. We then measure the size of the cracks by measuring the pixels number and convert it in mm.

4.3.2.7 Electronics and control

The control of the system is done using two SmartRob cards (Appendix A.1.6), both running Aseba (Appendix A.2.2). These cards embed a microcontroller, electronics to control motors and sensors.

They control the motors rotating the MSD magnets, the motor driving the propulsion wheel, the pump and the LEDs (Figure 4.24). Motor controllers are used to drive precisely the motors (Appendix A.2.2.1). The pump is controlled using Pulse Width Modulation (PWM) over the voltage.

Communication over Bluetooth is done with a computer running a user interface able to control the several parameters (Figure 4.25). The camera images are sent to the computer by LVDS using a SerDes interface (Section 3.1.1).

4.3.3 Results

With the full system working, we made inspection tests on the test block and on a real blade with cracks on it. Before each test, the part was demagnetized using a dedicated coil driven by an alternating current.

This chapter summarizes the results concerning the inspection capabilities, the demagnetization and the mobility.

4.3.3.1 Inspection images

Inspection tests are done on the test block and on a blade. The test block has a flat surface, which allows the system to move on it and take images automatically. The blade

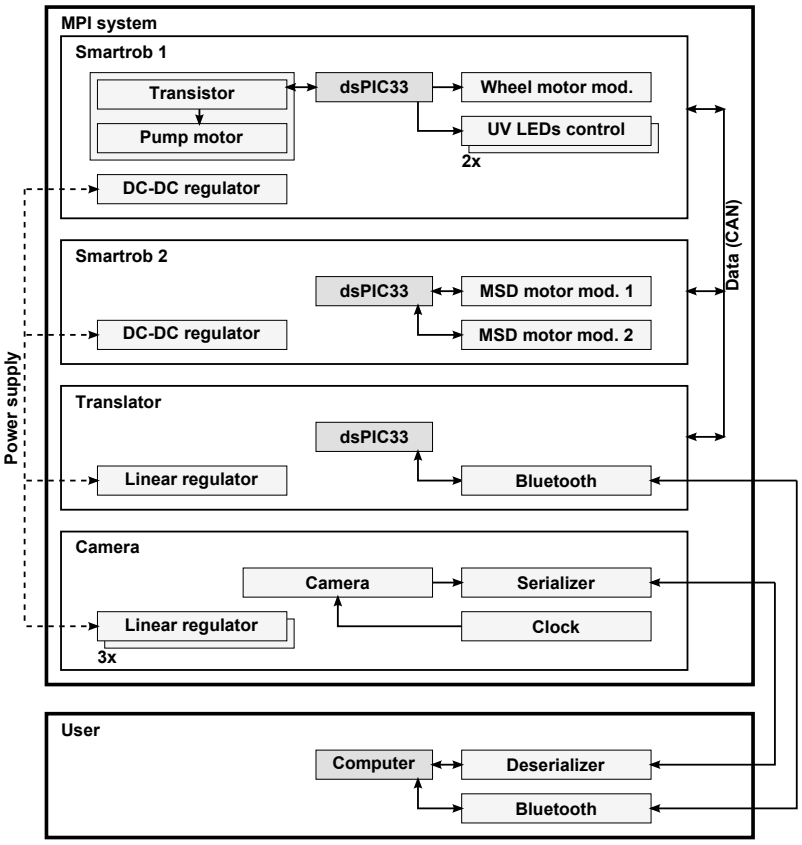

Figure 4.24: MSDI system electronics.

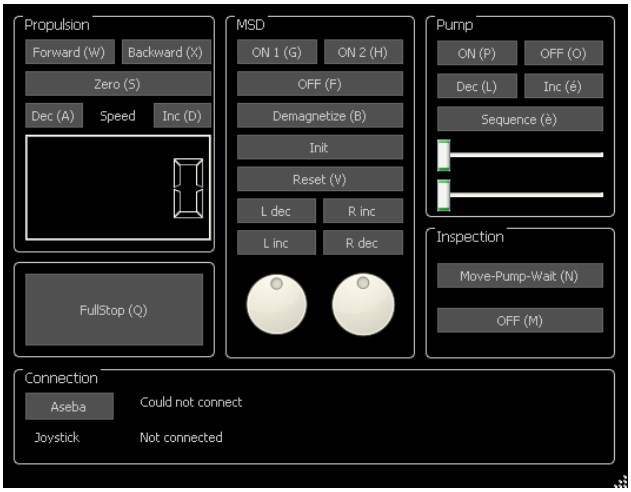

Figure 4.25: User interface of the MSDI system.

has a strong curvature, which prevent the system to move with its current design. The inspection images are thus taken by placing the MSDI2 on the desired location on the blade.

Test block

Figure 4.26 shows the sequence of operations of the system for an inspection. First the magnetization is activated by rotating the magnets of the MSD. Then the pump makes 15 ml of inspection liquid flow between the MSD feet. The decreasing flow is needed to get a sufficient torque to start the pump. The flow is then reduced to slowly spread the particles on the inspection zone. After the pump is stopped, there is a delay of two seconds to let the unnecessary liquid flow away so that the surface is ready to take an image. Finally, the system moves forward to a new position and the cycle starts again.

Using this inspection sequence, it takes 83 seconds to inspect a length of 80 mm on the test block, in 10 steps of 8 mm. It corresponds to around 1 mm/s, or 20 mm^2/s. Steps of 8 mm only are done to ensure each crack is taken at the center of an image, where the visibility is the best due to the lighting.

Figure 4.27 shows images of the cracks P1 to P4. They are taken from a movie recorded with the PixelPlus camera during an inspection sequence. The air gap between the MSD and the surface is set to 0.2 mm. The obtained image quality with respect to crack visibility and resolution is sufficient to detect all the cracks. The quality of the images has been validated with an inspection expert.

The system is thus able to perform autonomously an MPI on a straight line on a flat surface. The system performs automatically the whole process including the image acquisition, but does not perform the image analysis to achieve the final crack detection. This task is performed by an inspector.

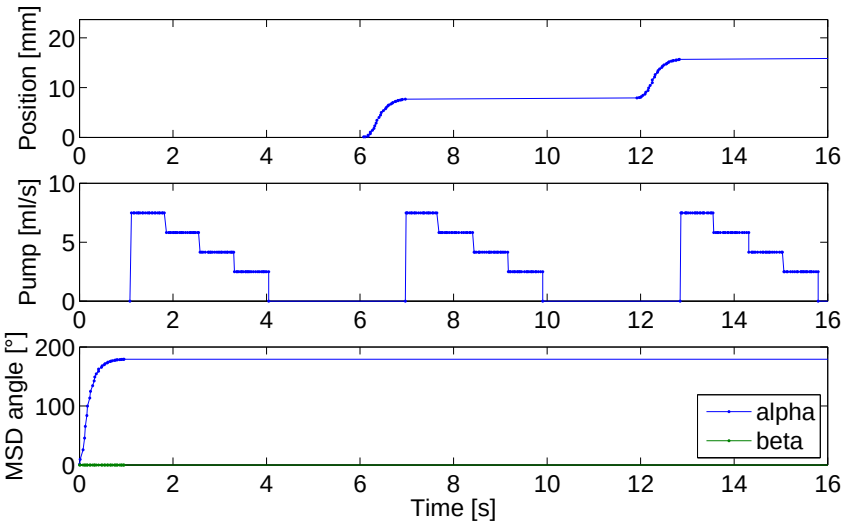

Figure 4.26: System state during the inspection sequence.

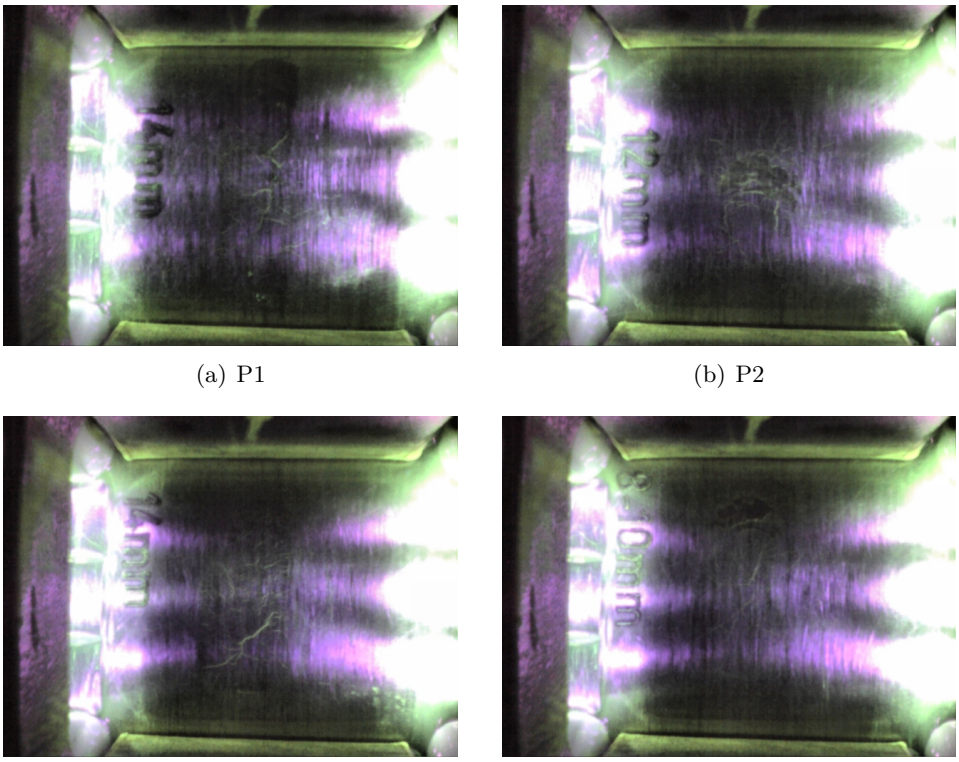

(a) P1 (b) P2

(c) P3 (d) P4

Figure 4.27: Images taken from an inspection sequence over the test block with the PixelPlus camera. The air gap between the MSD and the surface is of 0.2 mm, the magnetization is longitudinal.

Cracked blade

Tests were also done on a turbine blade, where 15 cracks having length between 0.9 to 4.1 mm were created artificially. In this case, the curvature is too strong for the system, making impossible to move on the edges. However, we can place the system manually on the cracks locations. The system holds when the MSDI2 is activated. We used the flat feet of the MSDI2, which are thus in contact only at one point.

After magnetizing the part and dispersing the liquid, the cracks are visible using this configuration. The Figure 4.28 shows three images of the cracks number 1361, 1362 and 1364, which have a length of 4.2, 2.2 and 1.6 mm respectively. We measure on the images lengths of 3.79, 2.18 and 1.51 mm respectively. These results are close to the real values, and confirm the inspection capabilities of the tool.

Curved feet would increase the visibility, as it would reduce the mean air gap and increase the magnetization.

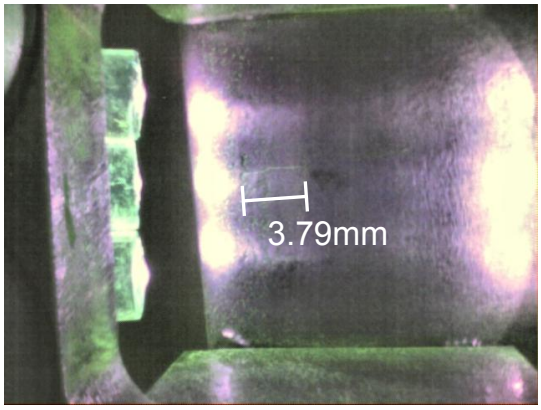

(a) nb 1361, l=4.2 mm.

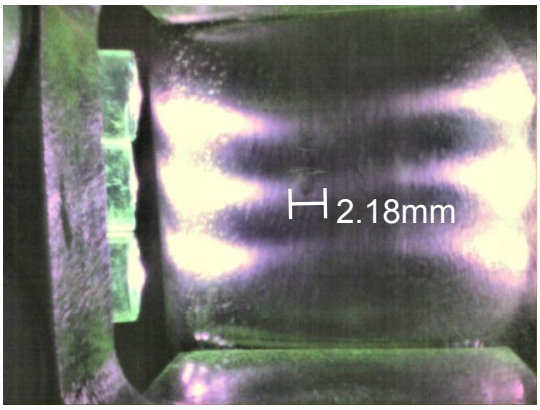

(b) nb 1362, l=2.2 mm.

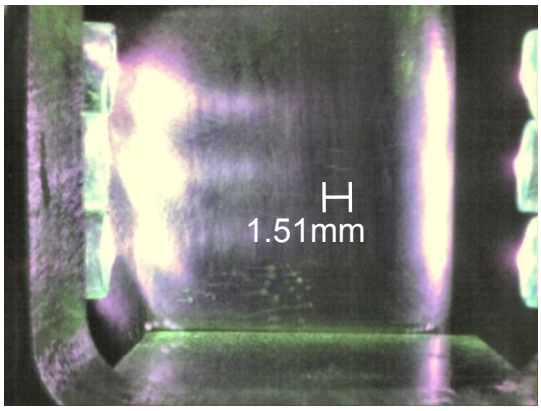

(c) nb 1364, l=1.6 mm.

Figure 4.28: Images from 3 different cracks of the blade.

Image processing

Processing can be applied to the images to enhance the visibility of the cracks. Using the program ImageJ[3], one method is to apply the following algorithms:

- Despeckle (remove noise)
- Subtract background (rolling ball radius of 50 pixels, depending on the image size)
- Color threshold (keeping the Hue values between 40 and 120 (green))
- Open (remove single dark spots)

Figure 4.29 shows the original and processed image of the P1 crack of the test block with perpendicular magnetization and no air gap. In the central zone, the cracks are well selected and visible. The length of the crack is of 14 mm, which is confirmed on the measurements.

The same processing was applied on the blade cracks, but the results are not so clear (Figure 4.30). The cracks do not have a sufficient contrast. It is thus difficult to differentiate between cracks and noise.

The cracks visibility and image quality is not sufficient to make a simple automatic crack detection. A human inspector still needs to observe the images and look for defects.

[3]ImageJ - Image processing and analysis in Java, `http://rsbweb.nih.gov/ij/`.

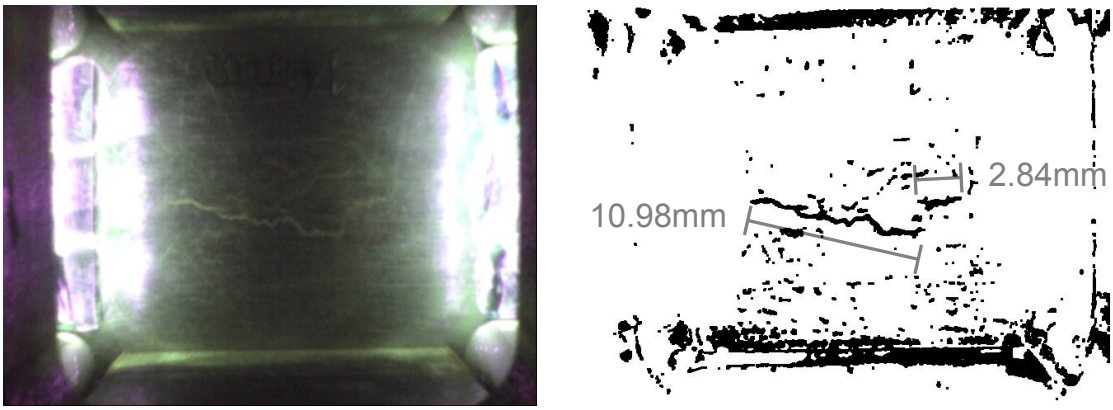

(a) (b)

Figure 4.29: Raw (a) and processed (b) images of the P1 crack. The full crack measures 14 mm, which is confirmed on the picture.

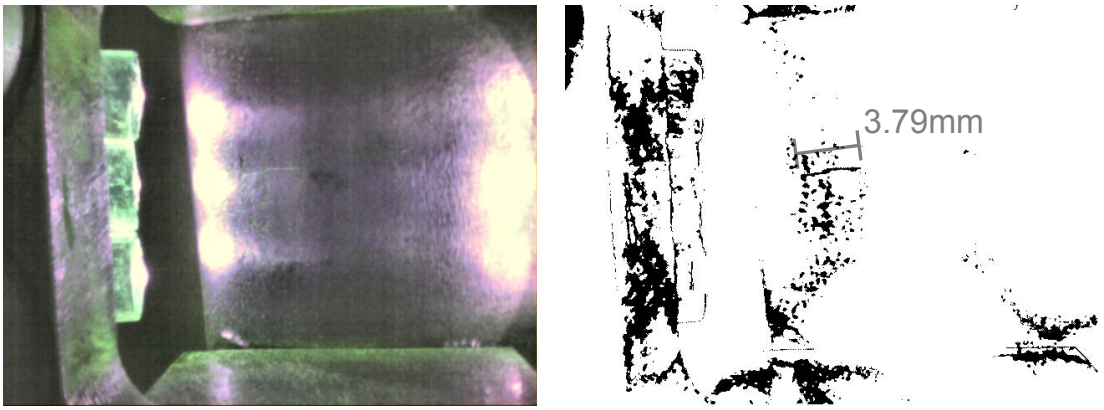

(a) (b)

Figure 4.30: Raw (a) and processed (b) images of the crack nb. 1361. It is difficult to differentiate the crack from the noise around it.

4.3.3.2 Demagnetization

A demagnetization of the part is usually necessary after an inspection, as a remanent magnetic field can attract abrasive particles which will increase the wear of the part. On parts which are inspected during their production process, a remanent magnetic field can pose problems during machining or welding.

Using an MSD allows to do it in two different ways. We can either apply an alternating decaying sequence on the magnets angular positions staying on the inspection place, or alternate the magnets while moving forward.

Measures of the orthogonal remanent flux density in the test block were done after different magnetization and demagnetizations using a gaussmeter. Figure 4.31 shows the results.

The first 2 columns show the remanent flux with no demagnetization. In the first case the MSDI is removed from the block with the attraction force still active, in the second

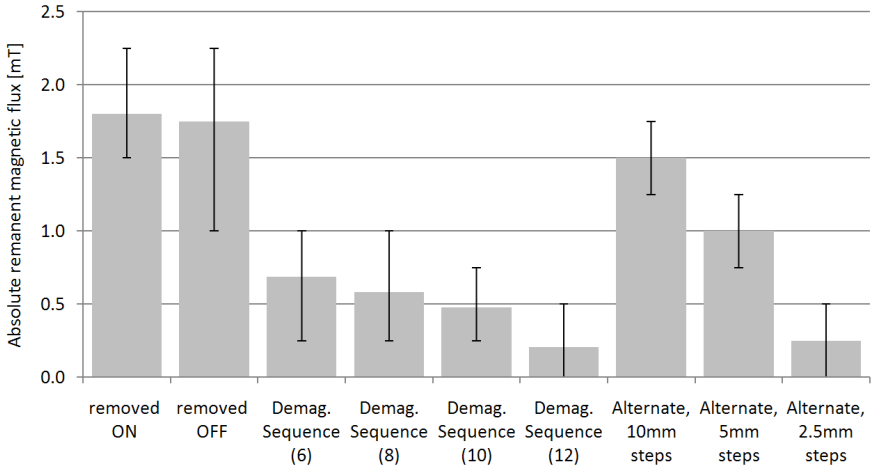

Figure 4.31: Demagnetization measures. Using a demagnetization sequence or alternating the magnetization over small steps give similar results.

one the MSD is switched off before removing. The results are very similar with a remanent flux of around 1.75 mT.

The third to sixth columns show the remanent flux after a demagnetization sequence, consisting in alternating the flux direction and reducing its intensity progressively (up to 12 flux direction changes, as already shown in Figure 4.16, page 105). Increasing the number of flux direction changes reduces the remanent flux. With 12 direction changes, the resulting flux is almost zero and validates the method.

For these first 6 columns, the values correspond to the mean of the absolute magnetic flux under the contact surfaces of the MSDI (6 measures), with the minimum and maximum indicated by the whiskers.

Another method has also been tested: instead of reducing the alternating flux, the reduction is obtained by rolling away the MSD, alternating the flux while moving. The sequence is: switch on in positive direction, switch off, move, switch on in negative direction, switch off, move, etc... The flux is then measured on the traveled path. Columns 7 to 9 show the results for different step sizes. We can see that the smaller the steps, the smaller the remanent flux. With 2.5mm steps, the measured flux is the same as with the demagnetization sequence with 12 flux direction changes.

The minimal resolution of the used Gaussmeter is of 0.5 mT, so the measures were done on the very beginning of the sensitivity of the sensor. The probe dimensions are 2.5 mm width, 5.5 mm long and 0.5 mm thick. The flux measure is the integral over the whole surface of the probe.

While the MSD enables to demagnetize the part, the magnetization from the magnetic wheel used for locomotion is still present and cannot be removed behind the system. This remaining magnetization is similar to the one made by the MSD, as their adhesion forces are close.

Another attaching system is thus needed if no magnetization can be left. It could be mechanical, pushing on both sides of the blade for example. An inch-worm movement similar to the Tubulo II using two MSDs is another option (Figure 2.67, page 65): before moving, the MSD would make a demagnetization sequence. The MSD would hold thanks to the adhesion force of the other one.

4.3.3.3 Mobility on the blade

As the blade has a strong curvature in some zones, the system cannot move everywhere in the same configuration. On the flat parts, the flat feet are well adapted (Figure 4.32(a)).

On the concave side, feet of the MSD are too far from the surface to get a sufficient force, thus the field is too weak for inspecting (Figure 4.13(a), page 104). Furthermore the current illumination system is taking too much place on the sides and prevents the wheels to touch in concave zones.

On the convex side, the feet may touch the blade if they are not placed at an appropriate distance (Figure 4.13(b)). With a 1.8 mm air gap, the system can move everywhere on the convex side without touching, except in the strong curvature zone of the leading edge (Figure 4.33), where a 2.6 mm air gap is needed (Figure 4.32(b)).

These air gaps are too big to get enough magnetization and crack visibility. Thus, specific feet as described in Figure 4.13 (page 104) are needed to obtain good inspection results.

As the wheels are placed on the side of the magnetic system, the MSD cannot move directly along the edge of the blade, but only 5 mm away. As the edge is the area with the most interest for inspection, a new support module is needed, with the wheels at the front and the back for example. However, the inspection area at the end of the blade will be reduced with such a design.

The current motor configuration of the MSD switching module is too high and would not pass between the blades in the turbine. Some mechanical adaptations are needed, by putting the motors horizontally with a 90° transmission for example.

4.3.4 Conclusions

The built system is able to perform a full MPI inspection on flat surfaces. It can magnetize, disperse the inspection liquid, light using UV LEDs, take an image, demagnetize and move straight. It shows good MPI inspection results on flat surfaces, as cracks are detected with almost the same visibility as with bigger inspection systems. The achieved average inspection speed is 1 mm per second on a width of 20 mm (without demagnetizing).

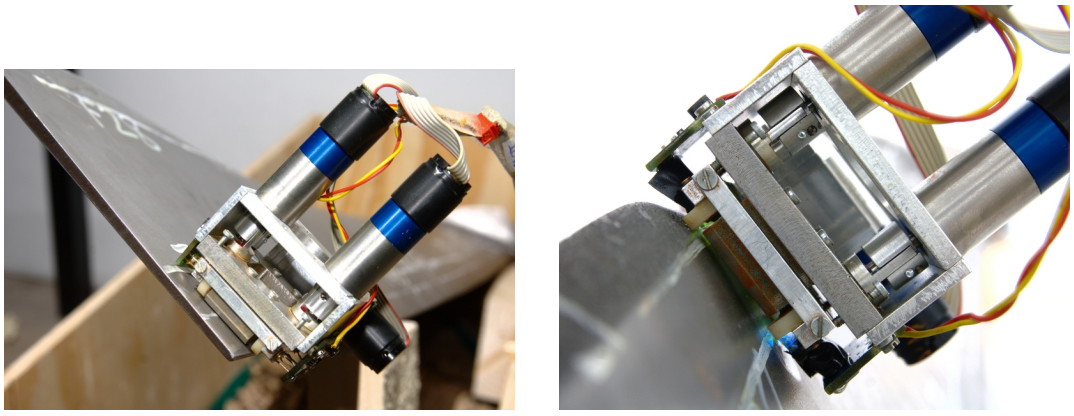

(a) (b)

Figure 4.32: MPI system on the blade. (a) very small curvature on the trailing edge, (b) strong curvature on the leading edge.

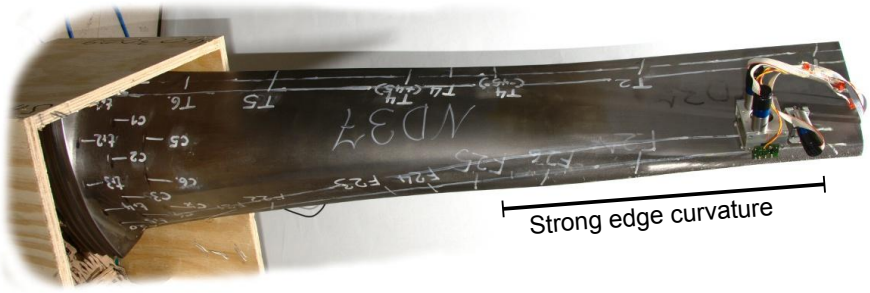

Figure 4.33: MPI system on the blade, showing the strong curvature of the leading edge zone.

The system can hold and move on the blade where the curvature is low. The edge zones, where the curvature is the highest, poses movement problems with the current system. Special feet adapted to the curvature are needed, as this zone is the most important for inspection.

Cracks on the blade are detectable using the system without locomotion, when the MSDI2 is placed directly on the blade.

Even though image processing can help detecting cracks, it does not work well in some cases. A human inspector is thus still needed to look for cracks on the recorded images. This could be improved with stronger magnetization, giving a better contrast on the images, and a better image resolution.

4.3.4.1 Future work

The MPI system was developed to show the feasibility of the method. It requires future developments and industrialization to become fully functional.

The current electronic boards are separated from the system and connected to it using cables, which make the system bulky and not practical to use. A dedicated electronics should thus be developed and embedded in the system, to enhance the portability and ease of use.

The contrast of the cracks could be increased by increasing the magnetization and lighting. Adapting the magnetization feet to the surface curvature would reduce the air gap and thus increase the magnetization. Reducing the distance between the feet would also increase the magnetization.

To improve the image quality, a better camera with a higher sensitivity, higher resolution and an autofocus should be used. The SerDes electronics and software could be adapted to use other cameras, such as the one used on the Cy-mag^{3D} II.

The mechanics should be adapted so that the system can follow the edge with no shift, by putting the wheels at the front and back instead of on the sides. It should also adapt to stronger curvatures.

For full demagnetization, the magnetic wheel ensuring climbing should be replaced by another system. For example, the system could wrap around the edge of the blade, with wheels pushing on both sides of the blade.

Another possibility would be to use only magnetic wheels for the magnetization. Putting many wheels on a flexible shaft (patented by W. Fischer [WF10]) would allow the system

to adapt to curvatures (Figure 4.34). Demagnetization would not be possible in this case.

4.4 General conclusions on advanced inspection methods

Visual inspection is often not enough to detect small or sub-surface defects in industrial environments. Embedding other NDT sensors on inspection robots is thus required to detect such defects. However, most of these sensors are difficult to miniaturize and integrate on small robots.

A small Eddy current sensor was fixed and used on the Tripillar II to detect cracks on a test block. This sensor can be modified to be better integrated on the robot, without disturbing its mobility. One problem with this type of sensor is that it measures only one point at a time. Inspecting a full surface is thus time-consuming and requires a precise positioning system.

A miniature Magnetic Particle Inspection system was then designed and validated. The developed system shows the feasibility of inspecting turbine blades without disassembling the turbine, using a frequently used inspection method. This system opens new perspectives for turbine inspections, as it could allow drastically reducing the time required to perform an inspection. Indeed, removing the turbine from the stator is tricky and needs time. Disassembling each blade of the turbine also takes time, as reassembling the turbine requires that it is balanced precisely. The developed system is smaller than any current MPI sensing method, and can still be further miniaturized if needed. The system could be built around an MSD slightly smaller than the MSDI1, for example.

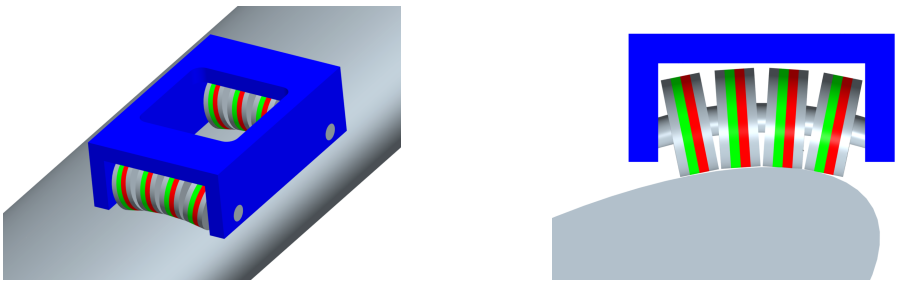

(a) (b)

Figure 4.34: Magnetic wheels on a flexible shaft could adapt to strong curvatures and magnetize the part.

5 Conclusion

5.1 Methodology summary

Based on the experience gained through the development of various robots and systems during this thesis, a short methodology summary to design miniature climbing inspection systems is proposed, focusing on ferromagnetic mobility and NDT.

Table 5.1 shows advantages, disadvantages and applications of the adhesion principles and mobility solutions that can be used to move on ferromagnetic structures, and that were tested in this thesis. An important point is that the choice of the adhesion principle and mobility concept will highly depend on the application and its requirements, and that no solution can work for all the possible applications. The advantages and disadvantages of each principle are now explained quickly.

Magnetic caterpillars can help when a high friction force is required. It can thus be helpful for an ultrasonic inspection system when a liquid couplant is used, as this liquid makes the surface very slippery. Outer corners passing would require a complicated structure for a robot using caterpillars.

Magnetic wheels have high adhesion force, but get blocked in inner corners, and require a system to unblock them. In addition to creating the adhesion force for the system, magnetic wheels can be used to magnetize a part for MFL inspection or MPI.

Advanced magnetic wheels (Cy-mag^{3D} concept) can produce a high adhesion force and can be used for very high mobility robots. Different wheels configurations can be used depending on the application and the obstacles to pass (Cy-mag^{3D}, bicycle, other...).

Table 5.1: Methodology summary for ferromagnetic mobility of mobile inspection systems

Mobility principle	**Comments**	**Applications**
Magnetic caterpillar	+ High friction force - Outer corners	Slippery surfaces (Ultrasonic inspection)
Magnetic wheel	+ High adhesion force - Inner corner blocking	MPI, MFL
Advanced magnetic wheel (Cy-mag^{3D})	+ High adhesion force, high mobility	High mobility, MPI (MFL)
MSD	+ Switchable adhesion force, demagnetization	High mobility, switch off for recovery, MPI (MFL)
Magnetic adhesion in tubes	+ Diameter adaptation - Low mobility in curves	Boiler tubes (and others)

MSDs allow to switch the adhesion force easily. They can offer high mobility if used on bipedal robots or similar structures. MSDs can be switched off for rescuing the robot, allowing to pull it using a tether cable for example. They can be used to magnetize a part for MPI or MFL inspection, and to demagnetize it.

Magnetic adhesion for tube climbing was used on the Tubulos to increase the range of diameter adaptation. However performances were lower than expected, as the mobility in curves is low. I would thus not recommend this principle for tube climbing, or with a redesign taking into account this problem.

After this summary about magnetic mobility, Table 5.2 shows a similar summary for inspection methods applicable on miniature mobile systems. The advantages and disadvantages of each inspection principle are now explained quickly.

Vision can be used for remote control by the user by giving a remote view from the robot. A camera also allows visual inspection, and is required for MPI. A disadvantage of vision is that it requires high speed data transmission (wired or wireless), and may require high embedded processing power.

Eddy Current sensors can be compact and need relatively low energy, but a full scanning of the part is required as such sensors inspect only one point at a time.

MPI can perform inspection of areas, which increases the inspection speed. However the inspection liquid dispersion can pose problems of integration, as well as the liquid storage.

Ultrasonic testing often requires a liquid couplant to transmit the sound wave. This liquid is very slippery and can pose problems of adhesion to a climbing system.

Even though some inspection methods are easier than others to embed on mobile inspection systems, the NDT method must be chosen by inspection experts, depending on the parts to inspect and on the defects to detect, as each method achieves different performances. The inspection system must then be designed to embed the correct sensor.

Importantly, possible interactions between mobility and NDT can allow strong integration. The magnetization required for MPI (and MFL) can be obtained using a magnetic system creating the adhesion force for the robot. Using the same magnetic system for these two functions allows to reduce the size of the final system. The magnetization from the adhesion system can also be helpful for Eddy current testing, as it can increase the defects detectability.

Table 5.2: Methodology summary for Non-destructive testing on mobile inspection systems

Sensing principle	**Comments**	**Applications**
Vision	+ Remote view - Signal transmission (wire, wireless), high processing power	Visual inspection, remote control, MPI
Eddy Current	+ Compact, medium energy consumption - Point inspection - scanning required	Choice depending on the parts to inspect and defects to detect
MPI	+ Area of inspection - Inspection liquid dispersion	
Ultrasonic	- Couplant liquid: slippery, dispersion	

5.2 Conclusion

The goal of this thesis was to study, design and test new miniature inspection systems able to move in and inspect complex ferromagnetic environments. In my work I focused on system integration and optimization of complete inspection systems. This effort is complementary to the work of Frédéric Rochat [Roc11], who focused on adhesion systems for miniature climbing robots. The results of this thesis illustrates the key role of integration in innovation. While most of the techniques integrated in the presented systems are within the state of the art, their detailed study and optimized integration allows for the achievement of totally new performances and redefines inspection methods.

The most evident example is the last system, based on MPI: MPI is well known, the cameras used are standard and the magnetic switches have been used in industry for decades. Nevertheless the careful study and integration of these techniques results in a radically new system, capable of redefining the inspection process and procedures.

Integration also allows us to tackle key aspects such as the safety of climbing robots and partial automatization of inspection tasks. The correct integration of sensors and the fusion of their data allows for leveraging the security level of the global system, enabling the use of such system in critical infrastructures. For example, very compact adhesion sensors were developed thanks to the high integration of mechanics, magnetism and electronics. These sensors largely help to control climbing robots, giving the assurance of a sufficient adhesion force.

5.3 Contributions

The main contributions of this work to the state of the art are the following:

- I contributed to the development and integration of different innovative magnetic miniature climbing robots. In all of these robots I studied the integration of electronics, sensors and batteries to allow wireless remote control, and the on-board integration of a camera or an other NDT sensor to inspect the environments they climb on. With the achieved small sizes and high mobility, these robots set new standards in the field of inspection robotics and allow for increasing the range of places that can be inspected.
- I showed that good integration allows for increasing the autonomy of miniature robots, for instance, for autonomously climbing on ferromagnetic structures, following a line, passing inner angles and stopping when finding non-ferromagnetic surfaces. Parts of an inspection procedure can thus be automatized, which simplifies the work of the human operator.
- I showed that the use of innovative sensors in addition to the required camera allows to clearly improve the perception of the environment by the remote operator. This allows for controlling the robot with more precision, in a safer and faster way.
- I developed a radically new miniature Magnetic Particle Inspection (MPI) system based on an MSD used for magnetization. The system can inspect a flat surface autonomously, performing all of the required steps of MPI on-board within a very reduced volume. This system can potentially inspect curved surfaces found on turbine blades. The small size of this inspection system opens totally new possibilities to inspect complex parts such as steam turbines without disassembling them.

5.4 Outlook

All of the developed robots and systems are prototypes and do not reach industrial quality. They show the mobility and sensing capabilities achievable with high system integration in miniature robots. However, they do not reach a sufficient robustness to perform real case inspections, as we are not sure whether we can get the robots back from the environment. This is a key issue, as a lost robot will cost time and money to access the robot and remove it. An industrialization of the prototypes is thus necessary to reach the required quality to perform inspections. It is not an easy process, as the improvements in mechanical robustness must not weaken the mobility performances due to the possible increases in weight or air gaps. An idea to help resolve the problem of blocked robots is to use MSDs or equivalent systems: in case of a problem, the adhesion force can be deactivated, and the robot can be pulled out using a tether cable, for example.

Parts of the work from this thesis are highly dependent on the current technologies. New electronics components and smaller or more powerful microcontrollers are continuously being developed and launched on the market. They allow for constructing smaller or more powerful electronics boards to control the robots, which can thus be designed smaller or with increased performance. Cameras also evolve quickly, increasing the number of pixels, increasing the sensitivity and reducing the noise of the signal. Better visual performances will thus be achieved in the future with cameras of the same size, and smaller cameras can be developed. From the energy point of view, it seems that the capacity of Lithium batteries will not increase substantially beyond current levels. However, they certainly will become safer and faster to charge. After a fast development, Neodymium magnets are slowly finding their maximum energy density. The highest grade of N56 achieved in laboratory in 2002 [RWKU02] is not far from the current N52 commercial magnets, and just a small increase can thus be expected in the future.

The required system integration will, however, remain, as it will be possible to build smaller robots if the components get smaller. The mobility concepts are also independent of the technologies' evolution.

A Appendices

A.1 Electronics

Some electronics components and modules used in the different robots are described in the next sections.

A.1.1 Microcontrollers

We use dsPIC33 microcontrollers on all robots to control the motors, sensors and communications. They have a 16 bit architecture running at a speed of up to 40 MIPS at 40 MHz. They embed a DSP (Digital Signal Processing) core and a DMA (Direct Memory Access) bus.

One dsPIC33 can control up to 3 motors using PWMs and sense their encoders outputs. It can drive and get the values from different sensors, such as IR distance sensors, accelerometers or current sensors. It can communicate with other microcontrollers using a CAN bus, and with a user computer using a serial port over a Bluetooth connection (Appendix A.1.5).

A.1.2 i.MX31 processor

A processor card for mobile robots was developed by the LSRO and LIS laboratories: the *mx31moboard* (Figure A.1). It is based on the freescale i.MX31 processor (ARM11, 533MHz, 128MB RAM), running a lightweight Linux distribution. This processor was designed for mobile products such as cell phones. It can process video images in real time and has a low power consumption (1.2 W, 2.4 W with the Wifi card). A Bluetooth module, an SD card, USB peripherals and a Wifi card can be plugged. A 3 megapixels camera can be mounted onto the board. The board has a compact size of 40x67x15 mm and embeds the computing power required for onboard image processing.

Other possibilities exists and could be considered for smaller systems, as the smaller Gumstix for example. With a size of only 17x58x4.2 mm, it embeds an ARM running at 600 MHZ. However, the drivers for the Wifi and camera were not fully functional at the time.

A.1.3 Motor control

A motor control electronic module is used to get a precise control of motors. It is composed of an H-bridge, a motor current measure and a motor encoder acquisition (Figure A.2).

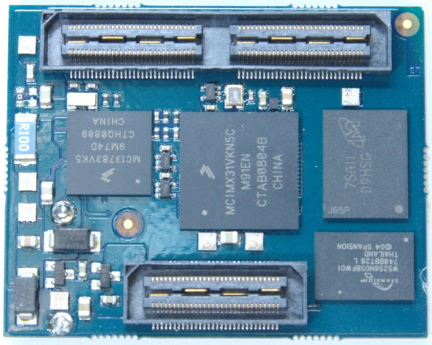

Figure A.1: mx31moboard card, measuring 40x67x15 mm.

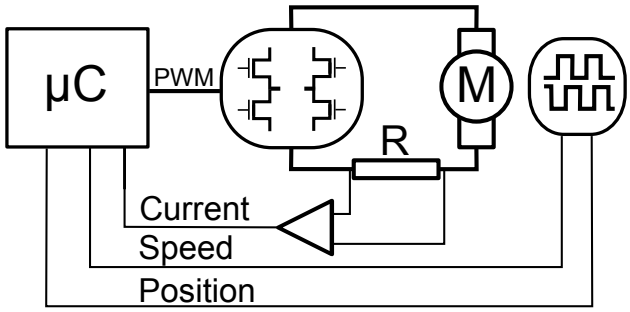

Figure A.2: Motor control electronics module (source: [Bon10]).

The microcontroller drives an H-bridge with PWM. The H-bridge is driving the motor using the battery voltage. The current measure is done by amplifying and measuring the voltage on a resistor placed in serial with the motor. The position and speed measures are done using the encoder pulses.

Using these sensing information about the motor, the motor can be controlled in torque, speed and position using 3 cascaded PID controllers (Appendix A.2.2.1).

A.1.4 Batteries

We use Li-ion (Lithium-ion) batteries on the robots. They have a high energy density compared to other established technologies (Figure A.3). The nominal cell voltage of 3.6/3.7 V is higher than the other battery technologies. It is an advantage, as it is higher than the usual 3.3 V tension used to drive the microcontrollers and other electronics. Using a single Li-ion cell and a LDO (Low dropout regulator, a linear DC converter) allows thus to have a stable power supply for the electronics. For higher voltages, which can be required by motors, 2 cells are used in serial and provide 7.2 V.

To use more than one battery and increase the autonomy, a battery module is used to plug them in parallel. It includes a protection chip that allows a safe use of the Li-ion battery, avoiding overcharge, over-current or complete discharge. Ideal diodes chips prevent a battery to be charged from other batteries when their voltages are different.

A.1.5 Bluetooth module

A Bluetooth module can be plugged on most robots to create a wireless serial link (Figure A.4). The LMX9838 chip from National Semiconductor is used, and measures 17x10x6 mm with the required PCB to drive it. It allows a 921600 baud communication between the robot and a computer over UART (universal asynchronous receiver/transmitter).

This wireless communication allows to program the robot, transmit user commands and receive sensors data remotely.

A.1.6 SmartRob card

The SmartRob card is a versatile control card for mobile robots (Figure A.5). It embeds a dsPIC33 (dsPic33FJ256MC710) and electronics allowing to drive 2 motors (sensing encoder and current), 4 servos motors, 1 camera, 5 proximity IR sensors and 3 Sharp distance sensors. It can be powered with a voltage between 6 to 13.2 V, and has a size of 75x75x10 mm.

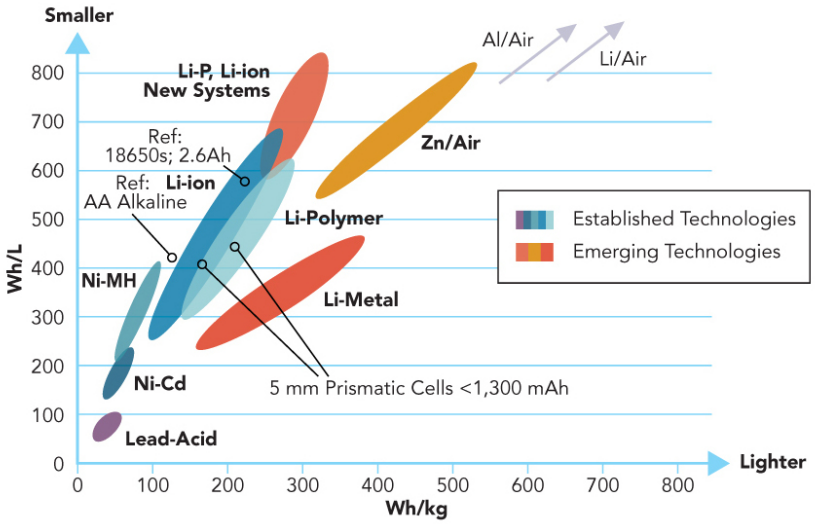

Figure A.3: Comparison of energy densities for various chemistries (source: Nexergy).

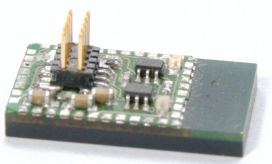

Figure A.4: Bluetooth module, measuring 17x10x6 mm.

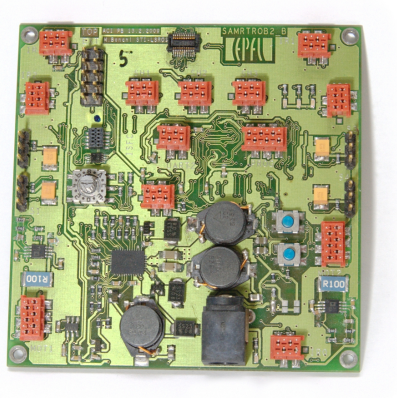

Figure A.5: Smartrob card, measuring 75x75x15 mm.

A.2 Programming

We use different libraries and tools to program the robots microcontrollers. The library Molole is used for the low level programming of the microcontrollers, and the Aseba framework allows to program the behaviors of the robots easily. The motor control module is described at the end of the section.

A.2.1 Low level

Molole is a library of low-level functions for the dsPic processor family. It is aimed to program robotics applications in an efficient way using interrupts. Using communication ports, interfacing sensors and peripherals or controlling motors can be done easily using this library.

Molole is mainly developed by the Mobots group at the Laboratory of Robotics Systems at EPFL. Molole is an open source project and can be downloaded at the following address: `http://gna.org/projects/molole`.

A.2.2 High level

Aseba is an event-based software architecture [MLM07]. It was developed to program and control robots using one or more microcontrollers, which can communicate over a CAN bus.

The event-based architecture is opposed to polling, where the peripherals are checked at a regular interval by the microcontrollers. It has the advantage to reduce to bus load, as less data is sent on it, and to reduce the reaction time, as the data is processed directly when it is received (Figure A.6).

The software structure of Aseba is shown in Figure A.7. A virtual machine is embedded in each dsPic, and executes a user code. The virtual machine controls the communication, and has access to native functions and low level controls. The user can program the behavior of the robot using a script language and an IDE (Integrated Development Environment). It gives access to low level functions of the microcontoller controlling the sensors and actuators.

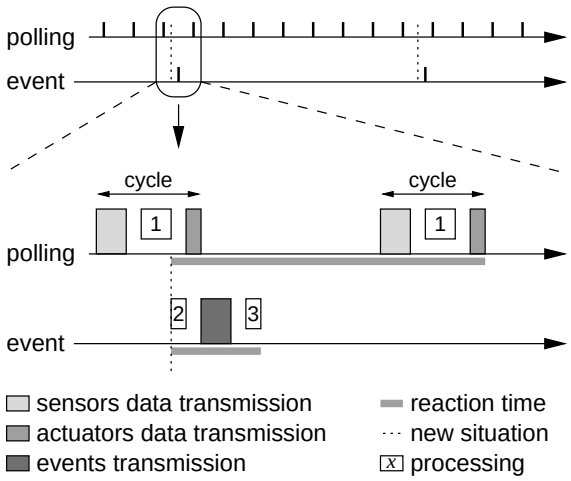

Figure A.6: A time oriented comparison of polling versus events-based systems. 1) main processor processing all sensors, 2) microcontroller processing its local sensors, 3) microcontroller processing incoming event and setting actuator. Because processing is done locally and only useful data is transmitted and the transfer occurs asynchronously, bus load and reaction time are both reduced when using events (source: [MLM07]).

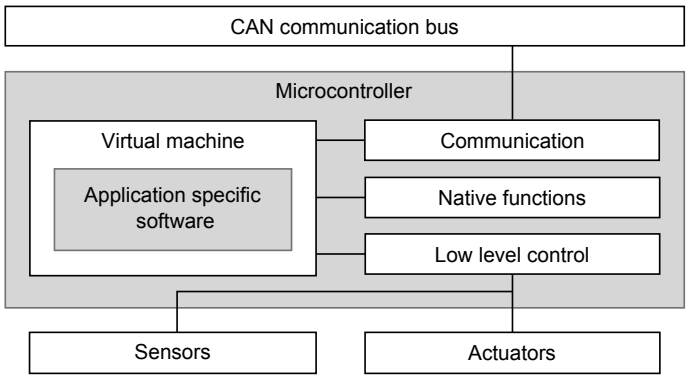

Figure A.7: Software structure of a microcontroller in an Aseba network (source: [MLM07]).

Aseba is mainly developed by the Mobots group at the Laboratory of Robotics Systems at EPFL. Aseba is an open source project and can be downloaded at the following address: `https://aseba.wikidot.com/`.

A.2.2.1 Motor control

The motor controller module is a nested PID controller over current, speed and position. There is one PI controller to control the current, one PID controller for the speed and one PD controller for the position, as shown in Figure A.8.

This flexible architecture allows to set maximum current or speed. The position controller can be disabled to control directly the speed of the motor. The same can be done to control directly the motor current. A generic code of a PID controller is shown in the

following equation:

$$i(t) = i(t-1) + e(t) \tag{A.1}$$

$$\text{output} = \frac{e(t) \cdot \text{Kp} + i(t) \cdot \text{Ki} + \text{Kd} \cdot (e(t) - e(t-1))}{s} \tag{A.2}$$

where t is the time index, i the integrator, e the error between the command and the current value, s a scaler, and Kp, Ki and Kd the PID constants.

The current time constant is much smaller than the speed and position one. The current controller runs thus at a higher frequency.

This controller is programmed using Molole. The different constants can be accessed and modified by Aseba.

A.3 Color coding

This section shows the basics of some color codes.

A.3.1 Red, Green, Blue

Red, Green and Blue (RGB) are the three primary colors for additive color synthesis. Using a combination of each RGB color intensity allows to display all the different colors, including black (no color) and white (all colors). Figure A.9 shows the RGB colors mapped on a cube, each axis representing a color.

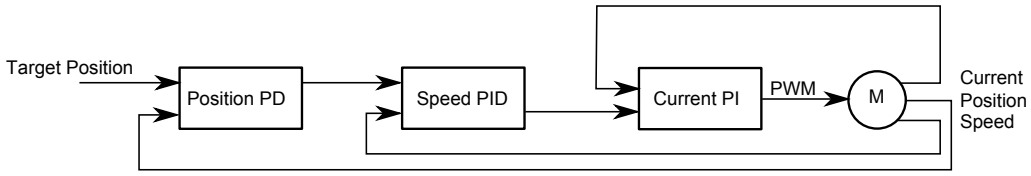

Figure A.8: Nested PID motor control (source: [Bon10]).

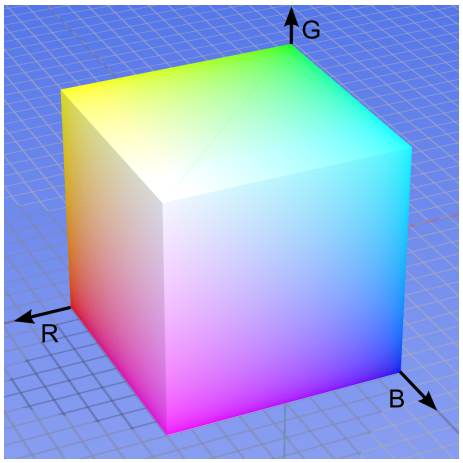

Figure A.9: RGB colors mapped to a cube. Each axis represent one color. The black is hidden at the origin (source: Wikipedia).

A.3.2 Hue, Saturation, Value

Hue, Saturation and Value (HSV) is a cylindrical geometry color space (Figure A.10). It was designed to be more intuitive than the RGB space.

The hue (angular dimension) chooses the color from the color circle: red is placed at 0°, green at 120°, blue at 240°and red again at 360°. The saturation is the color intensity: low saturation colors will look pale. The value is the shininess of the color: low value will result in dark colors.

The HSV values are obtained from the RGB values by the following formulas, with $H \in [0, 360[$, $S, V, R, G, B \in [0, 1[$, $max = \max(R, G, B)$, $min = \min(R, G, B)$:

$$\begin{aligned} H &= \begin{cases} 0, & \text{if } max = min \\ (60° \frac{G-B}{max-min} + 360°) \mathrm{mod} 360°, & \text{if } max = R \\ (60° \frac{B-R}{max-min} + 120°), & \text{if } max = G \\ (60° \frac{R-G}{max-min} + 240°), & \text{if } max = B \end{cases} \\ S &= \begin{cases} 0, & \text{if } max = 0 \\ 1 - \frac{min}{max}, & \text{otherwise} \end{cases} \\ V &= max \end{aligned} \tag{A.3}$$

A.3.3 YUV

The YUV model is a 3 components color space. It was designed to add color to the black and white television standard, by adding two color components to the already present grayscale image. It is now used a lot in image compression methods. The Luma (Y) represent the black and white, and the chrominance (U anv V) adds color to the image. An image decomposed in its Y, U and V components is shown in Figure A.11.

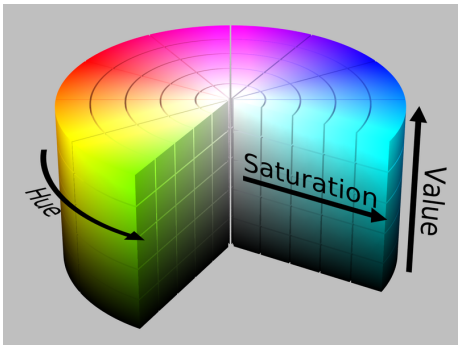

Figure A.10: HSV color cylinder (source: Wikipedia).

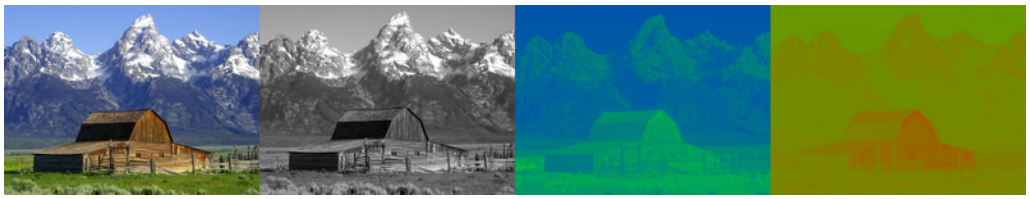

Figure A.11: YUV decomposition of an image (source: Wikipedia).

A.3.4 Bayer filter

A Bayer filter is a color filter array that allows detecting RGB colors on imaging sensors [Bay76]. The arrangement of the color filters is shown in Figure A.12. It is made of 50% of green, 25% of red and 25% of blue filters. This configuration using more green filters is chosen, as the human eye is more sensitive to green. Each pixels measure thus the intensity of one color only. The value of the two other colors can be interpolated from the neighbor pixels to get a full RGB value for each pixel [SNH98].

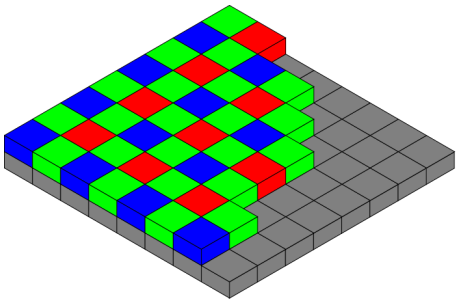

Figure A.12: The Bayer arrangement of color filters on the pixel array of an image sensor (source: Wikipedia).

Bibliography

[AAF+08] M. Armada, T. Akinfiev, R. Fernandez, P. Gonzalez de Santos, E. Garcia, and S. Nabulsi. Evolution and perspectives of climbing robots at the industrial automation institute. In *Climbing And Walking Robots: Proceedings of the 11th International Conference on Climbing and Walking Robots and the Support Technologies for Mobile Machines (CLAWAR 2008)*, pages 337–344, Coimbra, Portugal, 2008.

[BABE08] W. Brockmann, S. Albrecht, D. Borrmann, and J. Elseberg. Dexterous energy-autarkic climbing robot. In *Climbing And Walking Robots: Proceedings of the 11th International Conference on Climbing and Walking Robots and the Support Technologies for Mobile Machines (CLAWAR 2008)*, pages 525–532, Coimbra, Portugal, 2008.

[Bay76] Bryce E. Bayer. Color imaging array. US Patent nb 3971065, 1976.

[BBLM08] F. Bonaccorso, C. Bruno, D. Longo, and G. Muscato. Structure and model identification of a vortex-based suction cup. In *Climbing And Walking Robots: Proceedings of the 11th International Conference on Climbing and Walking Robots and the Support Technologies for Mobile Machines (CLAWAR 2008)*, pages 303–310, Coimbra, Portugal, 2008.

[BCC+05] D. Bozzetti, F. Chignoli, T. Cola, E. D'Alessio, and M. Gori. Robotized system for visual inspection inside boiler chambers and no-contact thickness evaluation of waterwall tubes in the steam generators of thermoelectric plants. In *International conference on climbing and walking robots (CLAWAR 2005)*, pages 753–761, London, UK, 2005.

[Ber03] Mark J. Bergander. EMAT thickness measurement for tubes in coal-fired boilers. *Applied Energy*, 74(3-4):439–444, 2003.

[BGJ05] C. Balaguer, A. Gimenez, and A. Jardon. Climbing robots mobility for inspection and maintenance of 3D complex environments. *Autonomous Robots*, 18(2):157–169, 2005.

[BGP+09] Gary L. Burkhardt, Todd H. Goyen, Albert J. Parvin, Ronald H. Peterson, and Richard F. Tennis. Remote-field Eddy current inspection tool for small-diameter unpiggable pipelines. In *ASME International Pipeline Conference (IPC 2009)*, volume 2, pages 41–44, Calgary, Canada, 2009. American Society of Mechanical Engineers.

[Bir01] A. S. Birring. Selection of NDT techniques for inspection of heat exchanger tubing. *NDT Internet Publishing, Journal of Nondestructive Testing and Ultrasonics (Germany)*, 6(8):1–12, 2001.

[BLM+10] Michael Bonani, Valentin Longchamp, Stéphane Magnenat, Philippe Rétornaz, Daniel Burnier, Gilles Roulet, Florian Vaussard, Hannes Bleuler, and Francesco Mondada. The MarXbot, a miniature mobile robot opening new perspectives for the collective-robotic research. In *IEEE/RSJ International Conference on Intelligent Robots and Systems (IROS 2010)*, pages 4187–4193, Taipei, Taiwan, 2010.

[BNES97] TA. Bubenik, JB. Nestlroth, RJ. Eiber, and BF. Saffell. Magnetic flux leakage (MFL) technology for natural gas pipeline inspection. *NDT and E International*, 30(1):36–36, 1997.

[Bon10] Michael Bonani. *Robotique collective et auto-assemblage*. PhD thesis, EPFL, 2010.

[BRS+08] Alain Bock, Frédéric Rochat, Patrick Schoeneich, Francesco Mondada, and Hannes Bleuler. Slim magnetic crawling robot, EPFL, 2008.

[BTIG07] Pinhas Ben-Tzvi, Shingo Ito, and Andrew A. Goldenberg. Autonomous stair climbing with reconfigurable tracked mobile robot. In *ROSE - International Workshop on Robotic and Sensor Environments*, pages 104–109, Ottawa, Canada, 2007.

[BVS+02] R. Bickerstaff, M. Vaughn, G. Stoker, M. Hassard, and M. Garrett. Review of sensor technologies for in-line inspection of natural gas pipelines. *Sandia National Laboratories, Albuquerque, December*, 2002.

[BXQ+10] Wang Binhai, Chen Xiguang, Wang Qian, Liu Liang, Zhang Hailong, and Li Bingqiang. Power line inspection with a flying robot. In *1st International Conference on Applied Robotics for the Power Industry (CARPI 2010)*, pages 1–6, Montreal, Canada, 2010. IEEE.

[Cho02] H. R. Choi. Robotic system with active steering capability for internal inspection of urban gas pipelines. *Mechatronics*, 12(5):713–736, 2002.

[CJHH10] B Chu, K Jung, CS Han, and D Hong. A survey of climbing robots: Locomotion and adhesion. *International Journal of Precision Engineering and Manufacturing*, 11(4):633–647, 2010.

[Coe02] J. M. D. Coey. Permanent magnet applications. *Journal of Magnetism and Magnetic Materials*, 248(3):441–456, 2002.

[CQJ05] L. Chen, P. W. Que, and T. Jin. A giant-magnetoresistance sensor for magnetic-flux-leakage nondestructive testing of a pipeline. *Russian Journal of Nondestructive Testing*, 41(7):462–465, 2005.

[DAS03] O. Duran, K. Althoefer, and L. D. Seneviratne. Pipe inspection using a laser-based transducer and automated analysis techniques. *IEEE-ASME Transactions on Mechatronics*, 8(3):401–409, 2003.

[DRSM10] Ludovic Daler, Frédéric Rochat, Patrick Schoeneich, and Francesco Mondada. Tripillar II: redesign and electronic integration, EPFL, 2010.

[Eom04] H. J. Eom. *Electromagnetic wave theory for boundary-value problems: an advanced course on analytical methods.* 2004.

[EYB09] Wu Enqi, Ke Yinglin, and Du Baojiang. Noncontact laser inspection based on a PSD for the inner surface of minidiameter pipes. *IEEE Transactions on Instrumentation and Measurement*, 58(7):2169–2173, 2009.

[FCSM09] W. Fischer, G. Caprari, R. Siegwart, and R. Moser. Compact magnetic wheeled robot for inspecting complex shaped structures in generator housings and similar environments. In *IEEE/RSJ International Conference on Intelligent Robots and Systems (IROS 2009)*, pages 4116–4121, 2009.

[FGHG06] M. Friedrich, L. Gatzoulis, G. Hayward, and W. Galbraith. Small inspection vehicles for non-destructive testing applications. *International Conference on Climbing and Walking Robots (CLAWAR 2006)*, pages 927–934, 2006.

[FTS07] W. Fischer, F. Tâche, and R. Siegwart. Inspection system for very thin and fragile surfaces, based on a pair of wall climbing robots with magnetic wheels. *IEEE/RSJ International Conference on Intelligent Robots and Systems (IROS 2007)*, pages 1216–1221, 2007.

[GCMD11] Fu Guoqiang, P. Corradi, A. Menciassi, and P. Dario. An integrated triangulation laser scanner for obstacle detection of miniature mobile robots in indoor environment. *IEEE/ASME Transactions on Mechatronics*, 16(4):778–783, 2011.

[GSC+06] M. Greuter, G. Shah, G. Caprari, F. Tâche, R. Siegwart, and M. Sitti. Toward micro wall-climbing robots using biomimetic fibrillar adhesives. In *Proceeding of the 3rd International Symposium on Autonomous Minirobots for Research and Edutainment*, pages 39–46. Springer, 2006.

[Guy72] W.K. Guy. Magnetic wheel. US Patent nb 3690393, 1972.

[HL10] Jiseong Hwang and Jinyi Lee. Magnetic images and NDT of the express train wheel using a high speed scan-type magnetic camera. *Key Engineering Materials*, 417-418:169–172, 2010.

[HMN+08] C. Hürzeler, J.C. Metzger, A. Nussberger, F. Hanni, A. Murbach, C. Bermes, S. Bouabdallah, D. Schafroth, and R. Siegwart. Teleoperation assistance for an indoor quadrotor helicopter. In *International Conference on Simulation, Modeling and Programming for Autonomous Robots*, Venice, Italy, 2008.

[HMT09] Masahiko Hoshina, Tomoaki Mashimo, and Shigeki Toyama. Development of pipe inspection robot; driving system and control of outer-rotor-typed spherical ultrasonic motor. In *International Conference on Advanced Robotics (ICAR 2009)*, pages 1–6, Munich, Germany, 2009. IEEE Computer Society.

[Int05] ASTM International. E 1444, standard practice for magnetic particle testing, 2005.

[Jam05] Anouar Jamoussi. Robotic NDE: A new solution for in-line pipe inspection. In *Middle East Nondestructive Testing Conference & Exhibition*, 2005.

[JJJY11] Jun Jongwoo, Kim Jungmin, Lee Jinyi, and Park Youngmin. A hand held magnetic camera system for real time crack inspection. In *IEEE Sensors Applications Symposium (SAS 2011)*, pages 298–301, 2011.

[JL89] Z. Ji and MC Leu. Design of optical triangulation devices. *Optics & Laser Technology*, 21(5):339–341, 1989.

[JL08] Jongwoo Jun and Jinyi Lee. Nondestructive evaluation of a crack on austenitic stainless steel using a sheet type induced current and a Hall sensor array. *Journal of Mechanical Science and Technology*, 22(9):1684–1691, 2008.

[JS11] Lee Jinyi and Kwon Seokjin. Non-destructive testing of a train wheel using a linearly integrated Hall sensor array. In *IEEE Sensors Applications Symposium (SAS 2011)*, pages 268–72, 2011.

[KL10] Jungmin Kim and Jinyi Lee. Inspection of the internal cracks on a pipe using a cylinder-type magnetic camera. *Key Engineering Materials*, 417-418:165–168, 2010.

[KOA+06] B. Kennedy, A. Okon, H. Aghazarian, M. Badescu, X. Bao, Y. Bar-Cohen, Z. Chang, B.E. Dabiri, M. Garrett, and L. Magnone. Lemur IIb: a robotic system for steep terrain access. *Industrial Robot: An International Journal*, 33(4):265–269, 2006.

[KYK+95] Y. Kawaguchi, I. Yoshida, H. Kurumatani, T. Kikuta, Y. Yamada, and OGC. Ltd. Internal pipe inspection robot. *Proceedings of the IEEE International Conference on Robotics and Automation*, 1:857–862, 1995.

[LBP08] Rodriguez H. L., Bridge B., and Sattar T. P. Climbing ring robot for inspection of offshore wind turbines. *International Conference on Climbing and Walking Robots (CLAWAR 2008)*, pages 555–562, 2008.

[Lew04] Dave Lewis. SerDes architectures and applications. In *DesignCon 2004*, 2004.

[LHJH07] Zhao Liefeng, Feng Huajun, Bai Jian, and Jin Hao. Panoramic optical annular staring inspection system for evaluating the inner surface of a pipe. In *Proceedings of SPIE - The International Society for Optical Engineering*, volume 6838, 2007.

[LM08] D. Longo and G. Muscato. Adhesion techniques for climbing robots state of the art and experimental consideration. In *Climbing And Walking Robots: Proceedings of the 11th International Conference on Climbing and Walking Robots and the Support Technologies for Mobile Machines (CLAWAR 2008)*, pages 6–28, Coimbra, Portugal, 2008.

[Lon04] D. Longo. A modular approach for the design of the Alicia climbing robot for industrial inspection. *The Industrial Robot*, 31(2):148–158, 2004.

[LRSM09] Barthélémy Lüthi, Frédéric Rochat, Patrick Schoeneich, and Francesco Mondada. Magnetic wheel, robot d'inspection miniature, EPFL, 2009.

[Lue08] Thomas Luethi. Non-destructive evaluation methods, 2008.

[MA09] A. Mazumdar and H. H. Asada. Mag-Foot: A steel bridge inspection robot. In *IEEE/RSJ International Conference on Intelligent Robots and Systems (IROS 2009)*, pages 1691–1696, 2009.

[MBR+09] F. Mondada, M. Bonani, X. Raemy, J. Pugh, C. Cianci, A. Klaptocz, S. Magnenat, J.C. Zufferey, D. Floreano, and A. Martinoli. The e-puck, a robot designed for education in engineering. In *Proceedings of the 9th Conference on Autonomous Robot Systems and Competitions*, volume 1, pages 59–65, 2009.

[MBS+08] S. Mondal, A. Brenner, J. Schang, B. Bridge, and T. Sattar. Remote automated non-destructive testing (NDT) weld inspection on vertical surfaces. In *Climbing And Walking Robots: Proceedings of the 11th International Conference on Climbing and Walking Robots and the Support Technologies for Mobile Machines (CLAWAR 2008)*, Coimbra, Portugal, 2008.

[MC00] C. Moosbrugger and F. Cverna. *Electrical and Magnetic Properties of Metals*. ASM International, 2000.

[MGSW09] J. Mampel, K. Gerlach, C. Schilling, and H. Witte. A modular robot climbing on pipe-like structures. In *4th International Conference on Autonomous Robots and Agents (ICARA 2009)*, pages 87–91, 2009.

[MLM07] Stephane Magnenat, Valentin Longchamp, and Francesco Mondada. ASEBA, an event-based middleware for distributed robot control. 2007.

[MM07] R. Moser and B. Mark. Automated robotic inspection of large generator stators. In *IEEE/ASME international conference on Advanced intelligent mechatronics*, pages 1–5, 2007.

[MMS04] C. Menon, M. Murphy, and M. Sitti. Gecko inspired surface climbing robots. In *IEEE International Conference on Robotics and Biomimetics (ROBIO 2004)*, pages 431–436, 2004.

[MRS+11] Olivier Marti, Frédéric Rochat, Patrick Schoeneich, Francesco Mondada, and Hannes Bleuler. Cy-mag3D : conception, réalisation et évaluation d'un robot mobile d'inspection magnétique muni d'une caméra et pouvant évoluer dans un environnement industriel ferromagnétique complexe. Master's thesis, EPFL, 2011.

[MS07] M. P. Murphy and M. Sitti. Waalbot: An agile small-scale wall-climbing robot utilizing dry elastomer adhesives. *IEEE/ASME Transactions on Mechatronics*, 12(3):330–338, 2007.

[MSF+08] L. L. Menegaldo, M. Santos, G. A. N. Ferreira, R. G. Siquelral, and L. Moscato. SIRUS: A mobile robot for floating production storage and offloading (FPSO) ship hull inspection. In *Amc '08: 10th International Workshop on Advanced Motion Control*, pages 27–32, New York, United States, 2008. IEEE.

[NKY+08] K. Nagaya, K. Kubo, T. Yoshino, T. Hoshi, and I. Murakami. Inspection robot climbing vertical cross piping using magnetic adhesive mechanism. *Journal of Optoelectronics and Advanced Materials*, 10(5):1069–1074, 2008.

[NM99] A. Nishi and H. Miyagi. Development of a flying-type wall-moving robot. In *International conference on climbing and walking robots (CLAWAR 1999)*, pages 699–705, Portsmouth, UK, 1999.

[NRS+08] Olivier Truong-Dat Nguyen, Frédéric Rochat, Patrick Schoeneich, Francesco Mondada, and Hannes Bleuler. Climbing robot with magnetic caterpillar, EPFL, 2008.

[NRS+09] Olivier Truong-Dat Nguyen, Frédéric Rochat, Patrick Schoeneich, Francesco Mondada, and Hannes Bleuler. Versatile train-like tube crawler. Master's thesis, EPFL, 2009.

[NSRM09] Olivier Truong-Dat Nguyen, Patrick Schoeneich, Frédéric Rochat, and Francesco Mondada. Tubulo II. Technical report, EPFL, 2009.

[NTTF95] T. Nishimine, O. Tsuyama, T. Tanaka, and H. Fujiwara. Automatic magnetic particle testing system for square billets. In *Industry Applications Conference. Thirtieth IAS Annual Meeting (IAS 1995)*, volume 2, pages 1585–1590, 1995.

[OSB10] A. L. C. Oliveira, M. F. Silva, and R. S. Barbosa. Architecture of an wheeled climbing robot with dynamic adjustment of the adhesion system. In *8th IEEE International Symposium on Intelligent Systems and Informatics, SIISY*, pages 127–132, Subotica, Serbia, 2010.

[PDvdP+08] C. Pulles, E. Dertien, H.J. van de Pol, R. Nispeling, and S. Stramigioli. Pirate, the development of an autonomous gas distribution system inspection robot. In *International Gas Union Research Conference (IGRC 2008)*, Paris, France, 2008.

[PJHN08] J. Pyrhonen, T. Jokinen, V. Hrabovcova, and H. Niemela. *Design of rotating electrical machines*. Wiley Online Library, 2008.

[PJL02] S. Park, H. D. Jeong, and Z. S. Lim. Development of mobile robot systems for automatic diagnosis of boiler tubes in fossil power plants and large size pipelines. In *IEEE/RSJ International Conference on Intelligent Robots and System*, volume 2, pages 1880–1885, 2002.

[PLH08] J.L. Paillat, P. Lucidarme, and L. Hardouin. Variable geometry tracked vehicle (VGTV) prototype: conception, capability and problems. In *Humans Operating Unmanned Systems (HUMOUS) conference*, pages 115–126, 2008.

[PPS+08] H. Prahlad, R. Pelrine, S. Stanford, J. Marlow, and R. Kornbluh. Electroadhesive robots - wall climbing robots enabled by a novel, robust, and electrically controllable adhesion technology. *IEEE International Conference on Robotics and Automation*, pages 3028–3033, 2008.

[Rey09] François Rey. Camera LVDS documentation. EPFL, 2009.

[RMDA02] M. Rachkov, L. Marques, and A. De Almeida. Climbing robots for porous and rough surfaces. In *International conference on climbing and walking robots (CLAWAR 2002)*, pages 1013–1020, Paris, France, 2002.

[Roc11] Frédéric Rochat. *Miniature Magnetic Climbing Inspection Robots*. PhD thesis, EPFL, 2011.

[RSB+10] Frédéric Rochat, Patrick Schoeneich, Michael Bonani, Stephane Magnenat, Francesco Mondada, Hannes Bleuler, and Huerzeler Christoph. Design of magnetic switchable device (MSD) and applications in climbing robot. In *13th International Conference on Climbing and Walking Robots and the Support Technologies for Mobile Machines*, pages 375–382, Nagoya, Japan, 2010.

[RSM+10] Frédéric Rochat, Patrick Schoeneich, Francesco Mondada, Hannes Bleuler, and Fabien Tâche. Magnetic wheels optimization and application to the MagneBike climbing robot. In *13th International Conference on Climbing and Walking Robots and the Support Technologies for Mobile Machines*, pages 801–808, Nagoya, Japan, 2010.

[Rus11] J.C. Russ. *The Image Processing Handbook*. Taylor & Francis, 2011.

[RWKU02] W. Rodewald, B. Wall, M. Katter, and K. Uestuener. Top Nd-Fe-B magnets with greater than 56 MGOe energy density and 9.8 kOe coercivity. *IEEE Transactions on Magnetics*, 38(5):2955–2957, 2002.

[Sad06] H. M. Sadek. NDE technologies for the examination of heat exchangers and boiler tubes principles, advantages and limitations. *Insight-Non-Destructive Testing and Condition Monitoring*, 48(3):181–184, 2006.

[SBS+08] F. Z. Shang, B. Bridge, T. Sattar, S. Mondal, and A. Brenner. Development of a climbing robot for inspection of long weld lines. *Industrial Robot - an International Journal*, 35(3):217–223, 2008.

[Sch95] H. Schempf. Neptune: Above-ground storage tank inspection robot system. *IEEE robotics and automation magazine*, 2(2):9–15, 1995.

[SGS06] W. Shen, J. Gu, and Y. Shen. Permanent magnetic system design for the wall-climbing robot. *Applied Bionics and Biomechanics*, 3(3):151–159, 2006.

[SMB+08] J. Shang, S. Mondal, A. Brenner, B. Bridge, and T. Stattar. A cooperative climbing robot for melt weld inspection on large structures. In *Climbing And Walking Robots: Proceedings of the 11th International Conference on Climbing and Walking Robots and the Support Technologies for Mobile Machines (CLAWAR 2008)*, Coimbra, Portugal, 2008.

[SMG+10] Hagen Schempf, Edward Mutschler, Alan Gavaert, George Skoptsov, and William Crowley. Visual and nondestructive evaluation inspection of live gas mains using the explorer family of pipe robots. *Journal of Field Robotics*, 27:217–249, 2010.

[SNH98] T. Sakamoto, C. Nakanishi, and T. Hase. Software pixel interpolation for digital still cameras suitable for a 32-bit MCU. *IEEE Transactions on Consumer Electronics*, 44(4):1342–1352, 1998.

[Sta07] R. K. Stanley. Recent advances in robotic coiled tubular assessment. *Insight-Non-Destructive Testing and Condition Monitoring*, 49(9):524–30, 2007.

[Str90] K. J. Strnat. Modern permanent magnets for applications in electrotechnology. *Proceedings of the IEEE*, 78(6):923–946, 1990.

[Suz99] K. Suzumori. Micro inspection robot for 1-in pipes. *IEEE/ASME transactions on mechatronics*, 4(3):286–292, 1999.

[TFC+09] F. Tâche, W. Fischer, G. Caprari, R. Siegwart, R. Moser, and F. Mondada. Magnebike: A magnetic wheeled robot with high mobility for inspecting complex-shaped structures. *Journal of Field Robotics*, 26(5):453–476, 2009.

[TSK01] K. Tsuruta, T. Sasaya, and N. Kawahara. In-pipe wireless micro robot. *Journal of Micromechatronics*, 1(3):263–272, 2001.

[UUAS06] O. Unver, A. Uneri, A. Aydemir, and M. Sitti. Geckobot: a gecko inspired climbing robot using elastomer adhesives. In *Proceedings of the IEEE International Conference on Robotics and Automation (ICRA 2006)*, pages 2329–2335, 2006.

[VV06] K.S. Vivekanand and K.S. Venkataraman. NDE techniques for reliable inspection of carbon steel tubes. *National Seminar on Non-Destructive Evaluation*, 2006.

[WCLZ10] Zhongwei Wang, Qixin Cao, Nan Luan, and Lei Zhan. Development of an autonomous in-pipe robot for offshore pipeline maintenance. *Industrial Robot*, 37:177–184, 2010.

[WF10] M. Wiesendanger and W Fischer. Device for inspection of generator air gaps. US Patent 61/296,199, 2010.

[YDAL10] Zhang Yuanming, T. Dodd, K. Atallah, and I. Lyne. Design and optimization of magnetic wheel for wall and ceiling climbing robot. In *IEEE International Conference on Mechatronics and Automation (ICMA 2010)*, pages 1393–1398. IEEE, 2010.

[YH92] D. Young Hugh. *University Physics*. Addison-Wesley, 8th edition, 1992.

[YNH07] A. Yamamoto, T. Nakashima, and T. Higuchi. Wall climbing mechanisms using electrostatic attraction generated by flexible electrodes. *International Symposium on Micro-NanoMechatronics and Human Science (MHS 2007)*, pages 389–394, 2007.

[YSHEJBJ08] Kwon Young Sik, Lim Hoon, Jung Eui-Jung, and Yi Byung-Ju. Design and motion planning of a two-moduled indoor pipeline inspection robot. In *IEEE International Conference on Robotics and Automation (ICRA 2008)*, pages 3998–4004, 2008.

[ZY07] Y. W. Zhang and G. Z. Yan. Detection of gas pipe wall thickness based on electromagnetic flux leakage. *Russian Journal of Nondestructive Testing*, 43(2):123–132, 2007.

[ZZM10] E. Zwicker, W. Zesch, and R. Moser. A modular inspection robot platform for power plant applications. In *1st International Conference on Applied Robotics for the Power Industry (CARPI 2010)*, pages 1–6, 2010.

List of Figures

List of Tables

Nomenclature

Symbols

For notation lightness, some symbols may be used to describe different variables in different sections. For example, μ may describe the magnetic permeability or the friction coefficient depending on the context.

Acronyms

CAD	Computer-Aided Design
CAN	Controller Area Network
CMOS	Complementary Metal-Oxide-Semiconductor
DC	Direct Current
EPFL	École Polytechnique Fédérale de Lausanne
ET	Eddy current Testing
I^2C	Inter-Integrated Circuit
IR	Infrared
LED	Light-Emitting Diode
Li-ion	Lithium-ion
LVDS	Low-Voltage Differential Signaling
MFL	Magnetic Flux Leakage
MSD	Magnetic Switchable Device
MSDI	Magnetic Switchable Device for Inspection
MPI	Magnetic Particle Inspection
NDT	Non Destructive Testing
PCB	Printed Circuit Board
PID	Proportional-Integral-Derivative
PWM	Pulse-Width Modulation
RAM	Random Access Memory
SerDes	Serializer/Deserializer
SD card	Secure Digital card
USB	Universal Serial Bus
UT	Ultrasonic Testing
UV	Ultraviolet

Curriculum vitæ

Patrick Schoeneich
Rte de Brent 47
1817 Brent (CH)
+41(0)788797435

28 years old
single
Swiss
patrick.schoeneich@gmail.com

Education

2007–2012	**PhD** in **mobile inspection robotics**, École Polytechnique Fédérale de Lausanne (EPFL), Switzerland.
2003–2007	**Master** in **Microengineering**, specialization in **Robotics and autonomous systems**. EPFL, Switzerland. **1-year exchange** at Indian Institute of Technology Madras, India
1999–2002	**Maturité fédérale**, Gymnase cantonal de Burier, Switzerland. Prices in Chemistry, Mathematics and Sport & Study

Patent

Title	Self-stabilizing one axis inspection robot with magnetic wheels
Filing	November 27, 2009
Inventors	Frédéric Rochat, Patrick Schoeneich, Dr. Francesco Mondada (EPFL), Dr. R. Moser (ALSTOM)

Prizes

Best paper award	Received for the paper *Cy-mag^{3D}: a simple and miniature climbing robot with advance mobility in ferromagnetic environment* published at CLAWAR 2010 [9].

Publications

[1] Patrick Schoeneich, Frédéric Rochat, Olivier Truong-Dat Nguyen, Roland Moser, and Francesco Mondada. Tripillar: a miniature magnetic caterpillar climbing robot with plane transition ability. *Robotica*, pages 1–7, 2011.

[2] Patrick Schoeneich, Frédéric Rochat, Olivier Truong-Dat Nguyen, Gilles Caprari, Roland Moser, Hannes Bleuler, and Francesco Mondada. Tubulo - a train-like miniature inspection climbing robot for ferromagnetic tubes. In *1st International Conference on Applied Robotics for the Power Industry (CARPI 2010)*, pages 1–5, Montreal, Canada, 2010.

[3] Gilles Caprari, Andreas Breitenmoser, Wolfgang Fischer, Christoph Hürzeler, Fabien Tâche, Roland Siegwart, Olivier Truong-Dat Nguyen, Roland Moser, Patrick Schoeneich, and Francesco Mondada. Highly compact robots for inspection of power plants. *Journal of Field Robotics*, 29(1):47–68, 2012.

[4] Frédéric Rochat, Patrick Schoeneich, Barthelemy Lüthi, Hannes Bleuler, Roland Moser, and Francesco Mondada. Cy-mag3D: a simple and miniature climbing robot with advance mobility in ferromagnetic environment. *Industrial Robot: An International Journal*, 38(3):229–233, 2011.

[5] Frédéric Rochat, Patrick Schoeneich, Olivier Marti, Hannes Bleuler, and Francesco Mondada. Cy-mag3De: magnetic climbing inspetion robot. In *Climbing and Walking Robots (CLAWAR 2011)*, pages 407–414, Paris, France, 2011.

[6] Frédéric Rochat, Patrick Schoeneich, Olivier Truong-Dat Nguyen, Hannes Bleuler, and Francesco Mondada. Tubulo II: magnetic climbing inchworm for inspection of boiler tubes. In *Climbing and Walking Robots (CLAWAR 2011)*, pages 949–955, Paris, France, 2011.

[7] Gilles Caprari, Andreas Breitenmoser, Wolfgang Fischer, Christoph Hürzeler, Fabien Tâche, Roland Siegwart, Patrick Schoeneich, Frédéric Rochat, Francesco Mondada, and Roland Moser. Highly compact robots for inspection of power plants. In *1st International Conference on Applied Robotics for the Power Industry (CARPI 2010)*, pages 1–6, Montreal, Canada, 2010.

[8] Frédéric Rochat, Patrick Schoeneich, Francesco Mondada, Hannes Bleuler, and Fabien Tâche. Magnetic wheels optimization and application to the magnebike climbing robot. In *13th International Conference on Climbing and Walking Robots and the Support Technologies for Mobile Machines (CLAWAR 2010)*, pages 801–808, Nagoya, Japan, 2010.

[9] Frédéric Rochat, Patrick Schoeneich, Barthelemy Lüthi, Francesco Mondada, and Hannes Bleuler. Cy-mag3D: a simple and miniature climbing robot with advance mobility in ferromagnetic environment. In *13th International Conference on Climbing and Walking Robots and the Support Technologies for Mobile Machines (CLAWAR 2010)*, pages 383–391, Nagoya, Japan, 2010.

[10] Frédéric Rochat, Patrick Schoeneich, Michael Bonani, Stéphane Magnenat, Francesco Mondada, Hannes Bleuler, and Hürzeler Christoph. Design of magnetic switchable

device (MSD) and applications in climbing robot. In *13th International Conference on Climbing and Walking Robots and the Support Technologies for Mobile Machines (CLAWAR 2010)*, pages 375–382, Nagoya, Japan, 2010.

[11] Stéphane Magnenat, Patrick Schoeneich, Frédéric Rochat, Philippe Retornaz, Michael Bonani, Valentin Longchamp, Martin Voelkle, Thierry Barras, Daniel Burnier, Pierre Noirat, Tarek Baaboura, Florian Vaussard, and Francesco Mondada. Autonomous construction by a mobile robot in unknown environments with scarce resources. In *4th International Conference on Cognitive Systems*, Zurich, Switzerland, 2010.

[12] Ricardo Beira, Ali Sengul, Masayuki Hara, Patrick Schoeneich, and Hannes Bleuler. Tendon-based transmission for surgical robotics: Systematic experimental friction modeling. In *International Conference on Applied Bionics and Biomechanics (ICABB 2010)*, Venice, Italy, 2010.

[13] Frédéric Rochat, Patrick Schoeneich, Olivier Truong-Dat Nguyen, and Francesco Mondada. Tripillar: Miniature magnetic caterpillar climbing robot with plane transition ability. In *12th International conference on climbing and walking robots and the support technologies for mobile machines (CLAWAR 2009)*, volume 1, pages 343–350, Istanbul, Turkey, 2009.